The Development of the CMS Zero Degree Calorimeters to Derive the Centrality of AA Collisions.

by

Jeff Wood, PhD(c)

Submitted to the graduate degree program in Physics and the Graduate Faculty of the University of Kansas in partial fulfillment of the requirements for the degree of Doctor of Philosophy

Committee:

Dr. Michael Murray, Chairperson

Dr. Stephen Sanders

Dr. Philip Baringer

Dr. Siyuan Han

Dr. Russ Ostermann

Date defended: *7 December 2012*

The Dissertation Committee for Jeff Wood, PhD(c) certifies that this is the approved version of the following dissertation:

The Development of the CMS Zero Degree Calorimeters to Derive the Centrality of AA Collisions.

Committee Chairperson:

Dr. Michael Murray, Chairperson

Date approved: *13 April 2013*

Abstract

The centrality of PbPb collisions is derived using correlations from the zero degree calorimeter (ZDC) signal and pixel multiplicity at the Compact Muon Solenoid (CMS) Experiment using data from the heavy ion run in 2010. The method to derive the centrality takes the two-dimensional correlation between the ZDC and pixels and linearizes it for sorting events. The initial method for deriving the centrality at CMS uses the energy deposit in the HF detector, and it is compared to the centrality derived by the correlations in ZDC and pixel multiplicity. This comparison highlights the similarities between the results of both methods in central collisions, as expected, and deviations in the results in peripheral collisions. The ZDC signals in peripheral collisions are selected by low pixel multiplicity to obtain a ZDC neutron spectrum, which is used to effectively gain match both sides of the ZDC.

Acknowledgements

I first thank Jesus Christ for a giving me purpose and Divine Counsel. Despite so much damage caused by religion, I am grateful that I was inspired to train for one of the few careers where honesty is still actually rewarded and deceit scorned. I hope I can show the church that the universe is more wonderful than they might have thought.

I thank the department of Physics and Astronomy at the University of Kansas for giving me a chance to succeed even though I was quite unlikely to academically survive it, let alone thrive. All the funding, the opportunities abroad at CMS, and the support to attend physics conferences greatly enhanced my physics understanding. I am so happy to have attended a graduate school that truly cares about the success of its students. KU will always get positive P.R. from me.

I thank the NSF for funding my long stays at CERN and for travel to Bariloche to enrich my instrumentation background. I thank the administration of Dan Marlow and Marleigh Sheaff on these matters.

I thank the DoE for funding my research and graduate support through all of this work. Even as a libertarian, I will continue to lobby for federal support for the DoE.

I thank the CMS collaboration for such a hermetic and capable machine. In particular, I thank the HCAL community for fitting the ZDC into the grand scheme of things.

I thank Michael Murray for all his advice thoughout many ups and downs on the ZDC projects. I am quite bewildered that having such knowledge in experimental physics comes with such a gentle and kind approach with his colleagues. Thanks for being the nicest and yet most informative boss I have ever had.

I thank Oleg Grachov for his great work on the ZDC project. I appreciate his primer from his broad background in calorimetry and nuclear physics.

I thank Paul Debbins for "showing me the ropes" of CMS hardware, and his dedication to the engineering of the ZDCs and other ZDC-related projects. I am grateful for a machine that works.

I thank Edward Norbeck and Duane Ingram for their vast wisdom in experimental physics. I feel have a great future ahead of me because of their example.

I thank Vasken Hagopian and Yasar Onel for their help and support of reviewing our centrality paper. I am glad they made the politics less daunting. I am also grateful for Vasken, with Dave and Chris, and their laser help in timing in the ZDCs.

I thank German Martinez for making sure ZDC was incorporated into the HCAL detector control system. His heads up into Argentine culture made my Bariloche visit a lot of fun too.

I thank Pawel De Barbaro and Jeff Spaulding in keeping ZDC as important as the rest of HCAL. I appreciate their recommendations. Their help really made taking data with ZDC smooth.

I thank Alice Mignerey, Jaime Gomez, and others from the University of Maryland Nuclear Chemistry group for their contributions to ZDC signal processing. Spectator neutrons are clear from their help.

I thank Marguerite Tonjes for her loyal support for ZDC in the CMS software environment. Without her, ZDC signal would have made no sense.

I thank Richard Kellogg for his crucial work to ZDC signal networking. There would be no ZDC data without him.

I thank Yetkin Yilmaz for his expertise on centrality at CMS and for letting me borrow his guitar so I could maintain my sanity during my short stays at CERN.

I thank Taylan Yetkin, Burak Bilki, Sercan Sen, and Ferak Ozal for their parallel analysis on ZDC signal during and after beam splash.

I thank Pat Kenny for his counsel on CMS software. I am grateful for his help in producing useful variables for ZDC signals.

I thank Dave Schudel for his help and extensive background on general software. A lot of coding hazards were fixed and later avoided because of his help. It was great to talk with him about these things whenever I needed a break.

I thank Jessica Stockham for her great help in building the ZDCs. With such an intelligence, it is comforting to know that physicists in the coming generations can come with great character and patience. It was wise that the KU physics department wanted to hire her expertise again for graduate school.

I thank Jennifer Sibille in helping to finish building the ZDC and its test beam efforts. I appreciate her great patience, and introducing me to the French language while I was at CERN. I wish her the best of luck in her future endeavors.

I thank my family for letting me relax during academic breaks and reminding me that there is "still a world out there."

I thank my family in Florida: Marcie, Willetta, Rob, Drew, Eric, Val, Mark, Luz Elena, Mirko, Robbie, and Bruce for making my Lithuanian Heritage so sunny.

I thank my family from the West Coast: Merle, Sandy, Susie, Kay, Jenny, Ross, Jamie, and Jiah for giving me a place to cool down for the winter.

I thank my family in New England: Oma, Johnny, and Tommy for making me feel at home again.

I thank my late mother for advising me not to "settle," and my late brother for his belief that I was meant for great things. If they only knew how far their advice went...

I thank last, but certainly not least, my father for believing in me even in my failures and his encouragement even during tragedy. It is a blessing to have an example of a man so comfortable and secure with himself to look up to. I hope he can now consider his son a phoenix who rose from his ashes.

Contents

List of Tables

List of Figures

Chapter 1

Introduction

"QCD is quite a colorful theory..."

1.1 Quantum Chromodynamics

The Standard Model of particle physics is a very successful theory on the small-scale structure of the universe. It explains the nature of both matter and the interaction of matter through forces that includes all the known forces except gravity. The theory includes spin-1/2 particles called fermions that substantiate all the matter in the universe, and spin-1 bosons that exchange momentum between fermions when fermions interact, resulting in forces. There is one more particle, a spin-0 particle, called a Higgs' boson, which explains the intrinsic mass of each particle in the theory. The Higgs' boson's own mass is even explained through a self-interaction, and it explains why the mass of each particle in the theory, if massive at all, is different.

The Standard Model is broken down into a few categories: generation of fermionic matter, quarks versus leptons, and all the bosons. For every particle except the massless particles and the Higgs' boson, there is a respective antiparticle as well. Quantum chromodynamics (QCD), is preoccupied with the nature of the quarks and the gluons. A table of the particles in the Standard Model is given in Figure 1.1.

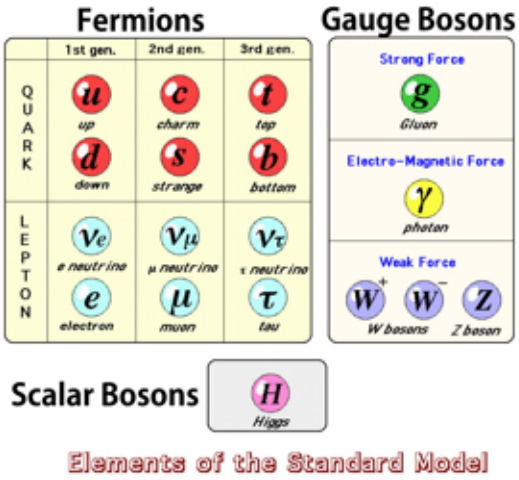

Figure 1.1: The table of particles in the Standard Model is shown here. Quantum chromodynamics is preoccupied with the quarks and gluons. Each quark carries its own flavor.

The theory of quarks is quite bizarre. First of all, quarks carry a kind of charge that no other fundamental fermion in the Standard Model carries. This interesting charge has been called color charge, and this is the important part of the etymology of quantum *chromo*dynamics [1]. Electromagnetic charge, for comparison, requires only two variants to create an electrically neutral object, usually denoted "positive" and "negative." However, color charge requires either three different color charges if such quarks are all matter or antimatter, or two color charges if such quarks are color charge matter-antimatter pairs. Part of these conditions arises from the fact that the total wavefunctions of the hadrons need to be antisymmetric. This means that the interchange of flavor, space, and electromagnetic charge wavefunctions in QCD are not enough to guarantee antisymmetry without a fourth quantum number, the color charge. The total wavefunctions of quarks must be antisymmetric because they are fermions, and must flip sign under interchange with another quark. It should be noted that, to-date, no net color-charged particle has been observed in any particle detection experiment even though the theory of QCD requires that the individual quarks themselves are color charged. This is an important part of the theory, and it is called "color confinement."

So, any composite state of quarks is expected to be color-neutral.

Another property that quarks share seems to be "flavor. Flavor is a quantity in quarks that can change during a weak interaction, where up quarks can become down quarks and release an electron and an anti-electron neutrino, down quarks can become up quarks and release a positron and an electron neutrino. There are various analogs for the other flavors also. Flavor is not conserved during weak interactions, but flavor is conserved in QCD. Up quarks carry up-ness flavor and down quarks carry down-ness flavor. The other, more massive quarks carry their respective flavors as well. So, there are strange-ness, charm-ness, bottom-ness, and top-ness to complete in every respective quark that carries each. It is the combination of flavors of quarks, with their respective quantum spins, that give hadrons their unique properties.

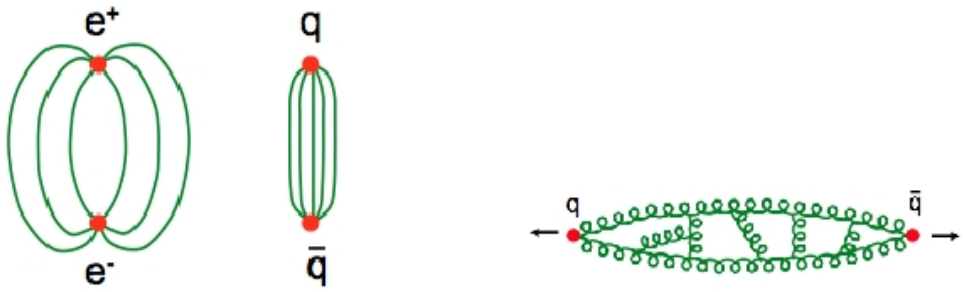

Figure 1.2: A comparison of the interaction of two electromagnetic charges labelled "e" and the interaction of two quarks labelled "q" are shown here. Gluons self-interact in QCD, so this causes the color force to increase with distance because the flux increases. In electromagnetism, the field flux decreases with distance, weakening the force. The gluon fields are shown as coils in the right cartoon.

Hadrons are made by quarks in combinations. With any number of flavors, quarks can be mixed and some can be identical. Quark combinations that come in quark-antiquark pairs are called mesons. Three quarks that are all either matter or all antimatter are called baryons or antibaryons respectively. It should be noted that some research in particle accelerator experiments might have detected four quark and five quark hadrons, which suggests that hadrons are not limited to pairs or triplets, but the results are still in development. No matter what is natural, the theory of QCD certainly

does not restrict states to pairs or triplets either. One thing that is interesting, however, is that quarks never seem to be observed by themselves. Quarks are held together by fields that are mediated by gluons [1]. Gluons are what get transmitted between quarks that carry their respective color charges. So, this also means that gluons carry momentum, and the change of momentum in the exchange between gluons or quarks results in the color force. The definitive property of the color force is that it seems to be one that gets stronger with distance, and no other fundamental interaction in physics seems to behave this way. This is because of a feature of QCD called "asymptotic freedom" [2, 3] It can be shown that asymptotic freedom is a consequence of any non-abelian gauge theory, and QCD is a theory of this type [4]. Figure 1.2 shows how the quantum theory of electromagnetism and QCD differ in this respect. The explanation of this is that gluons not only are able to interact with quarks, but also with themselves through the mediation by even more gluons. This makes QCD not only much more complicated than the quantum theory of electromagnetism, but also more interesting.

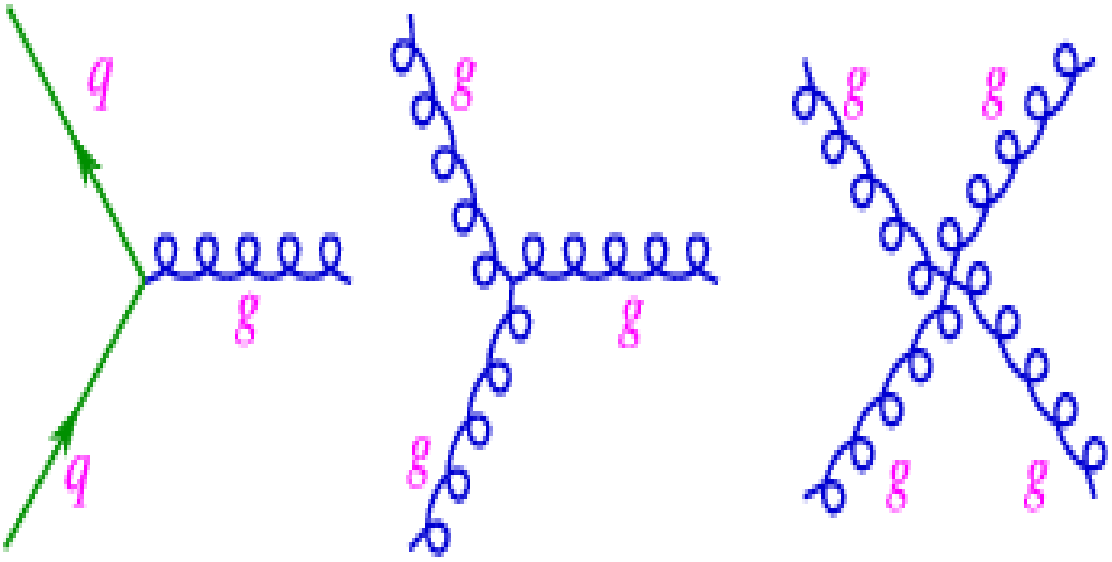

Figure 1.3: The three fundamental vertices exclusive to QCD are shown here. Gluons are able to interact with themselves in QCD, which are indicated by the middle and right vertices. The quark propagators are shown as straight arrows and gluon fields are shown as coils, as is typical notation.

In quantum electrodynamics, the electromagnetic field does not self-interact like the

gluon field does. The self-interaction of gluons in QCD is possible because the gluons themselves are color-charged. They are, by nature, superpositions of color charge states because they are the physical substantiations of the exchanges of exactly one color-anticolor pair. In order to make combinatorics work out correctly, there are eight possible combinations of color-anticolor states that gluons may carry that account for every interaction they mediate. This is because QCD interactions can be mathematically formulated as an SU[3] Lie Algebra, and these interactions, the gluons, can be stated by the adjoint representations of this algebra, which has exactly eight orthonormal bases [1]. This means that both quark-gluon as well as gluon-gluon interactions can produce physics observables in the laboratory. Figure 1.3 shows the fundamental interactions exclusive to QCD in the form of Feynman diagrams. These diagrams, not limited to QCD, are standard representations of the topology of all known quantum field theory processes. They show the propagation of particles as paths and the interactions of their respective fields as vertices.

QCD processes that deal with momentum exchange, Q, of $Q > 2$ GeV are said to be "hard," whereas "soft" QCD processes involve $Q < 2$ GeV. Hard QCD processes typically involve violent momentum exchange, which usually happens in quark-quark interactions mediated by gluons. Soft QCD processes, on the other hand, usually involve mostly gluon-gluon interactions. This typical, although not exclusive, behavior is a consequence of the quarks having an intrinsic mass, and the gluons being massless. It is naturally easier, and therefore takes less energy to bump a massless object than a massive one. This is important because hard QCD processes fall under the category of perturbative QCD (pQCD), which is a numerically solvable realm of QCD that has been experimentally verified with the prediction and subsequent measurement of hadronic jets. Therefore, QCD in the high-energy limit is pQCD [5]. So, pQCD is the discipline in which to study the universe in its infancy, when similar conditions it solves for were very hot and dense. The physics of common objects like the proton and neutron, however, fall under the realm of non-perturbative QCD, which is much harder to solve.

The nonlinearity that results from the self-interactions of the gluon fields are the main complication. Fortunately, non-perturbative QCD can be studied by observing soft QCD processes because it is, essentially, QCD under the low-energy limit. This low-energy limit is more applicable to the universe today because it is cold and diffuse, which is quite the opposite of the conditions that hard processes are produced by. This low-energy limit governs, ironically, most of the QCD-applicable objects in the universe even though less is known about it than the high-energy limit. The consequence of small momentum transfer is that soft QCD processes produce observables that change very little in an accelerator's beam direction, which is called the forward region of high energy physics. So, the forward region is ideal for studying non-perturbative QCD.

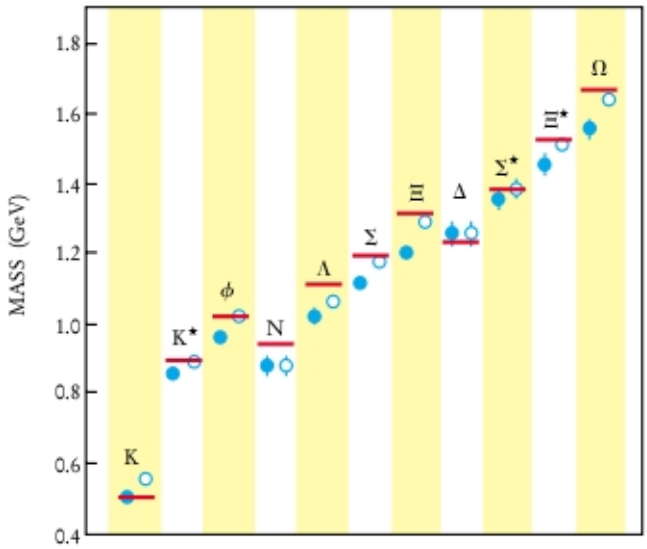

Figure 1.4: The spectrum of mass predicted by QCD for various hadrons is shown here. The closed circles are predictions tied to the K mass, and the open ones to the ϕ mass. All predictions have 10% confidence level. This was taken from [6].

QCD is quite a successful theory. One interesting success of QCD was the prediction of the spin, charge, and mass of the $\Omega-$ baryon before its discovery in the laboratory [7]. It is able to predict the mass of all low-mass quark-containing hadrons within 10% confidence level using various computational techniques. Low-mass quarks are, exclusively, the up, down, and strange varieties. As techniques get better, the confidence

level seems to improve more. An example of the mass spectrum of low-mass quark baryons is given in Figure 1.4. This spectrum shows two calculations, one based on the mass of the ϕ and one on the K, because they are the lowest mass hadrons containing at least one strange quark. The calculation must have input from at least one meson with strangeness because strange quarks are not present in stable nuclear matter, and of course, are not seen by themselves.

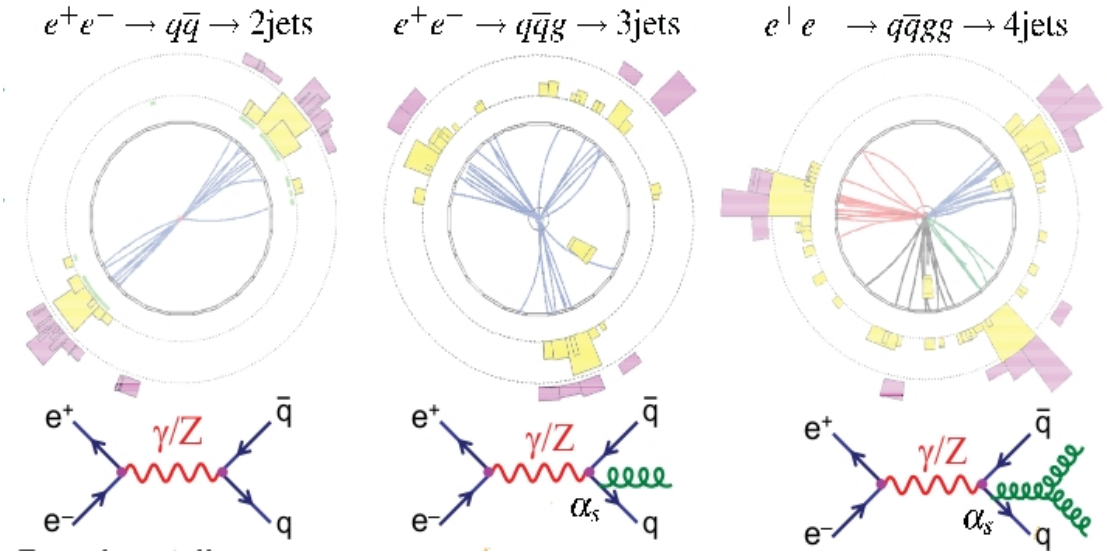

Figure 1.5: From left to right: two, three and four jet predictions of QCD in e^+e^- colliders are shown here. They have been realized in e^+e^- colliders in good agreement with pQCD. The radiation of gluons by outgoing quarks creates hadronic jets of matter.

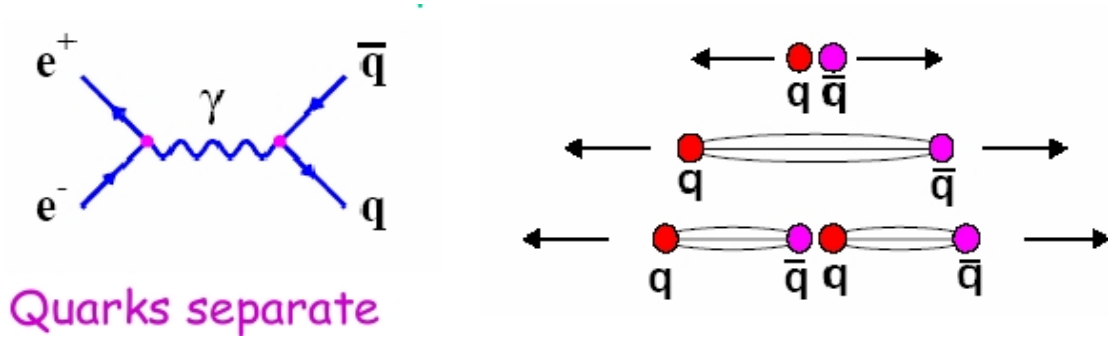

Figure 1.6: Fragmentation in QCD is shown here. When quarks get pulled apart, new quark-antiquark pairs are produced from the increase in the QCD potential. This is how hadronic jets form.

Another prediction of QCD is the production of hadronic jets. These jets are formed by the interaction of diverging quarks by gluons or the radiation of gluons by these quarks. Both of these scenarios can produce new particles. Figure 1.5 shows empirical examples of multiple jet production from e^+e^- collisions both in the laboratory, and the concept of such production in the form of Feynman diagrams. Because the QCD potential energy increases with distance, more energy is available to create new particles as quarks are pulled apart. Figure 1.6 shows a cartoon of how it is easier to relax the gluon fields with the production of new particles rather than to allow the quarks to separate further. This relaxation via new particle production is the main mechanism of hadronic jet creation.

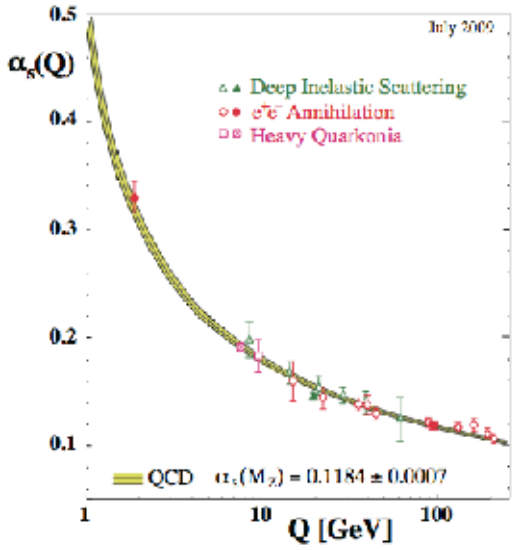

Figure 1.7: The coupling strength of QCD as a function of momentum transfer Q is shown here. Due to antiscreening by self-interacting gluon fields, the coupling strength decreases with more energy [8].

As collision momentum increases, the coupling strength of QCD actually drops. This is because of the anti-screening phenomenon of QCD fields. If collision momentum goes up, the quarks can get closer together, thereby relaxing the QCD field. In soft QCD, the quark wavefunctions are typically more spread out, and are anti-screened. In pQCD,

quarks become more point-like due to Lorentz contraction, and the anti-screening begins to disappear. A plot of the drop in the QCD coupling strength is given in Figure 1.7.

1.2 Heavy Ion Physics

Heavy ion physics is the study of the effects of colliding nuclei to produce matter that has properties similar to the early universe. This matter is called a quark-gluon plasma (QGP). QGP is, conceptually, a state of matter in which conditions are energetic enough to deconfine quarks from each other. This is distinct from color deconfinement because the requirement of quark deconfinement is not to separate quarks from a composite state, but quarks from hadronic states of matter. A lump of QGP is still expected to be color-neutral, although the quarks are no longer confined to hadrons as long as they are in the plasma. Such a state of matter is important to examine QCD theory because composite hadronic effects are separated from quark-gluon, and gluon-gluon interactions within it.

Heavy ions are essentially atomic nuclei stripped free of any bound electrons. When nuclei are spherical, they have a radius (r) proportional to $A^{1/3}$, where A is the mass number of the nucleus. If the geometry of heavy ion collisions becomes important, as it often is, then it is simplest to select spherical nuclei. The nuclear collision cross section is related to the area swept by one nucleus that has the potential of colliding at all. This is related to the total nuclear cross section, which is given by $\sigma_{AA}(b) = \pi b^2$, where σ_{AA} is the total cross section of nucleus, and b is the impact parameter. It can show how much nuclear matter has collided at least once in a nuclear collision, which has the potential of producing the QGP. So, the amount of QGP produced, if any, is dependent on the geometry of each heavy ion collision.

The density profile of the spherical nucleus is related to the nuclear potential energy well [10]. This nuclear potential, called the Woods-Saxon potential, models the amount of bound energy of the nucleons in the nucleus as a function of the nuclear radius.

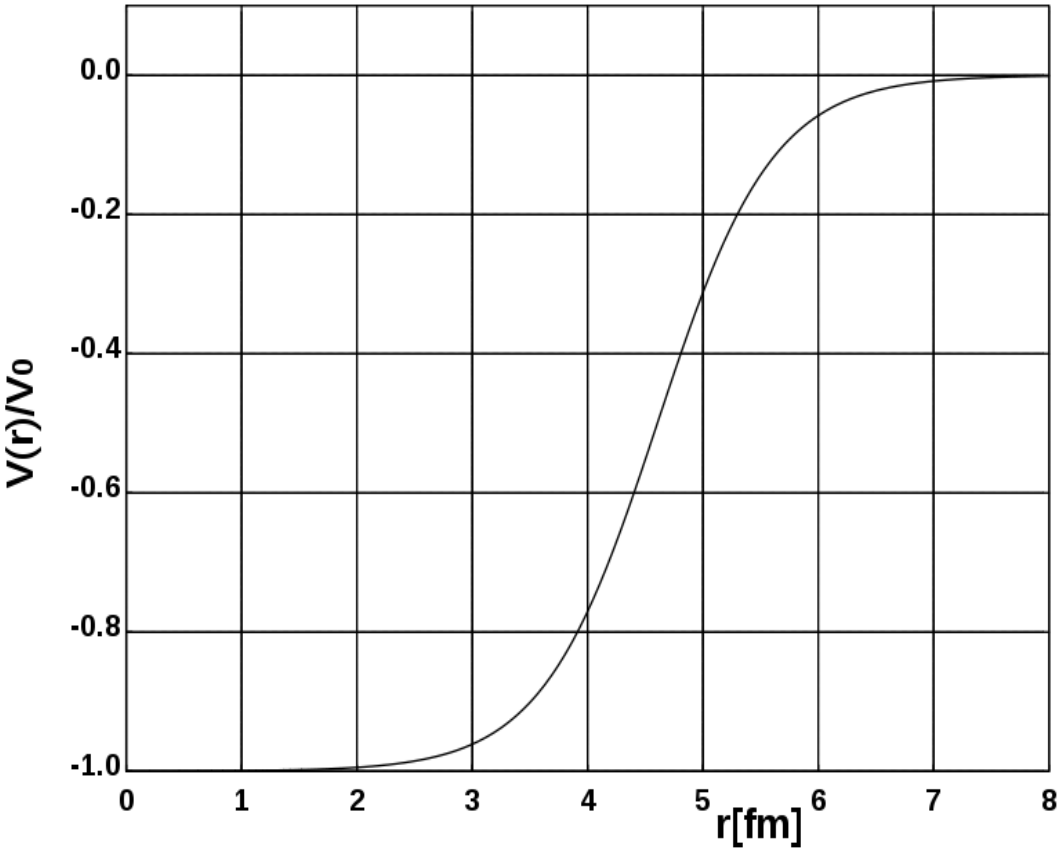

Figure 1.8: A Woods-Saxon distribution for A = 50 and a = 0.5 fm is shown here. This models the nuclear potential for large spherical nuclei [9].

The potential energy of the Woods-Saxon distribution is given by: $V[r] = -\frac{V_0}{1+exp[\frac{r-R}{a}]}$, where V_0 is the depth of the well, r is the radial distance from the center of the nucleus, R is the radius of the nucleus, and a is the skin depth. A key characteristic of this potential is that it is quite uniform for most of its radial distribution, but then it tapers off at the periphery of the nucleus smoothly, completing a potential well. This particular tapering off has a finite thickness that is the skin depth of the nucleus. This is because the nucleons obey Fermi-Dirac statistics, and that their energy piles up throughout the depth of the Woods-Saxon potential. This means that the energy at a given radius in the Woods-Saxon potential is proportional to the density of nucleons at that radius within the nucleus. An example of a Woods-Saxon potential is given in Figure 1.8.

Even though modelling the distribution of nucleons using the Woods-Saxon potential is reasonably correct, the actual distribution is certainly not smooth event by event, because the individual nucleons are an important part of the nuclear structure. There are certainly fluctuations in the distributions of nucleons within a heavy ion, so that any two heavy ion collisions are not expected to produce the same particle multiplicity at a given b.

The Glauber model [11, 12, 13] handles the random arrangement of individual nucleons within colliding nuclei. This is created by randomly distributing nucleons, each of which have proton-proton collision cross section, within a total nuclear collision cross section derived from the width of the Woods-Saxon potential. Under a large number of collisions in simulation, this handles the statistical fluctuations. Within the Glauber model, it is assumed that nucleon-nucleon collisions happen in straight lines. This is quite reasonable because the average nucleon-nucleon momentum transfer $Q \sim 1$ GeV is much less than the total momentum per nucleon of the heavy ion beams involved. The Glauber model, then, shows how many nucleon-nucleon collisions are expected from each class of collisions with a given average impact parameter b. When the Glauber model is implimented in a Monte Carlo, it can show the number of participants (N_{part}), the number of nucleons that collided at least once in a heavy ion collision, in each event.

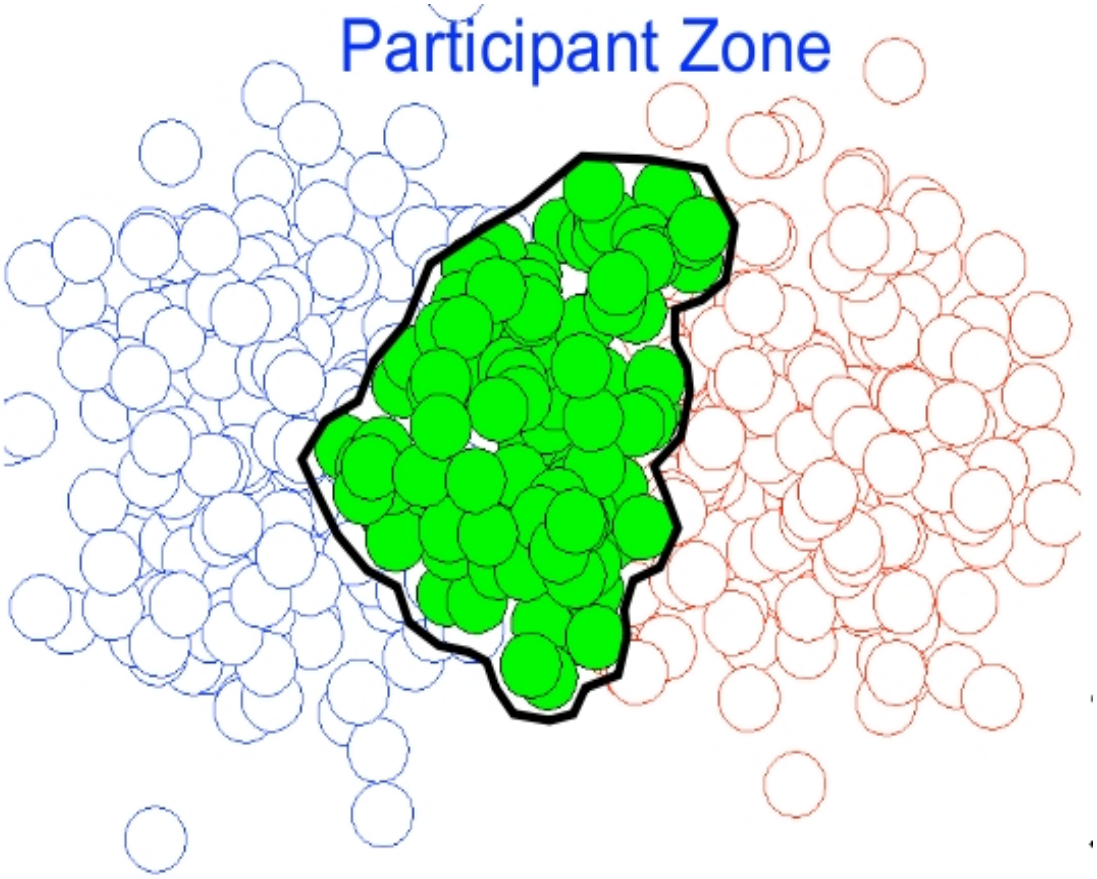

Figure 1.9: A Glauber model picture of a typical heavy ion collision is shown here. The red and blue circles stand for the spectators, and the participants are shown in solid green. Each of the nucleons are modelled to have the total cross section in pp collisions.

The number of nucleons that do not interact are called spectators. However, it is possible in these simulations to achieve an average N_{part} that is a non-integral value. The number of collisions (N_{coll}) is distinct from N_{part} because nucleons can collide more than once in a given event. N_{coll} is proportional to the nucleon density, and this is therefore consistent with how the Glauber model is formulated. An picture of how the Glauber model handles a typical heavy ion collision is given in Figure 1.9.

Since the spectators do not participate in the heavy ion collisions, they are independent of the collision products. This makes them not only derivable under simulation, they are also directly measurable in a model-independent way. It is not possible, however, to do this with N_{part} because the participants are essentially destroyed by creating new collision products in each event.

With the Glauber model in place, the most fundamental parameter in the geometry of heavy ion collisions can be derived. This parameter is called the centrality. In heavy ion collisions, N_{part} between two colliding nuclei is not constant event by event, and is not even constant with impact parameter b. It is important to monitor N_{part} in each collision by deriving the centrality. The impact parameter b is more intuitive and can be compared to the centrality. The impact parameter, b, is defined as the closest distance between the centers of the two colliding nuclei. Centrality, then, is the fraction of events that have an impact parameter smaller than a given percentile of all collisions, so that b scales in the *same direction* as the centrality. It is important to pay attention to this *forward* scaling with b because it is easy to erroneously interpret the centrality with a backward scaling with b. Since b has a statistical, but not deterministic, connection to centrality, N_{part} can only be statistically bounded by centrality ranges. So, a centrality range is inversely correlated to the average number of participants, $< N_{part} >$. The centrality limits are therefore defined by collisions where $< N_{part} >$ achieves a maximum at 0%, and $< N_{part} > = 0$ at 100%. Collisions that are closer to 0% centrality are said to be central, and those that are closer to 100% are said to be peripheral. Since so many heavy ion collision parameters depend on centrality, measuring it is crucial to

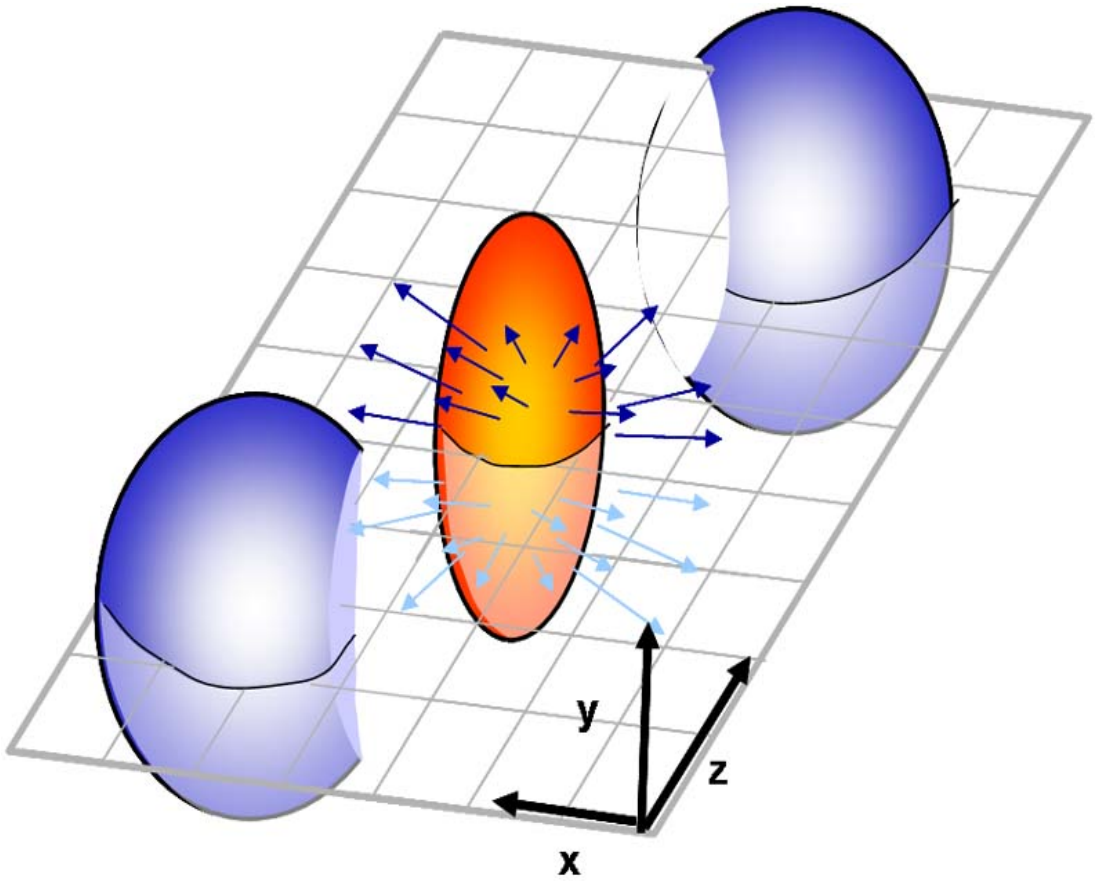

Figure 1.10: An arbitrary, and yet idealized, nuclear overlap is shown here. The shape of the QGP formed from the collision, in orange, is made apparant from the intersection of the overlapping nuclear cross sections, in blue. The arrows show the directions of the particles produced by the QGP.

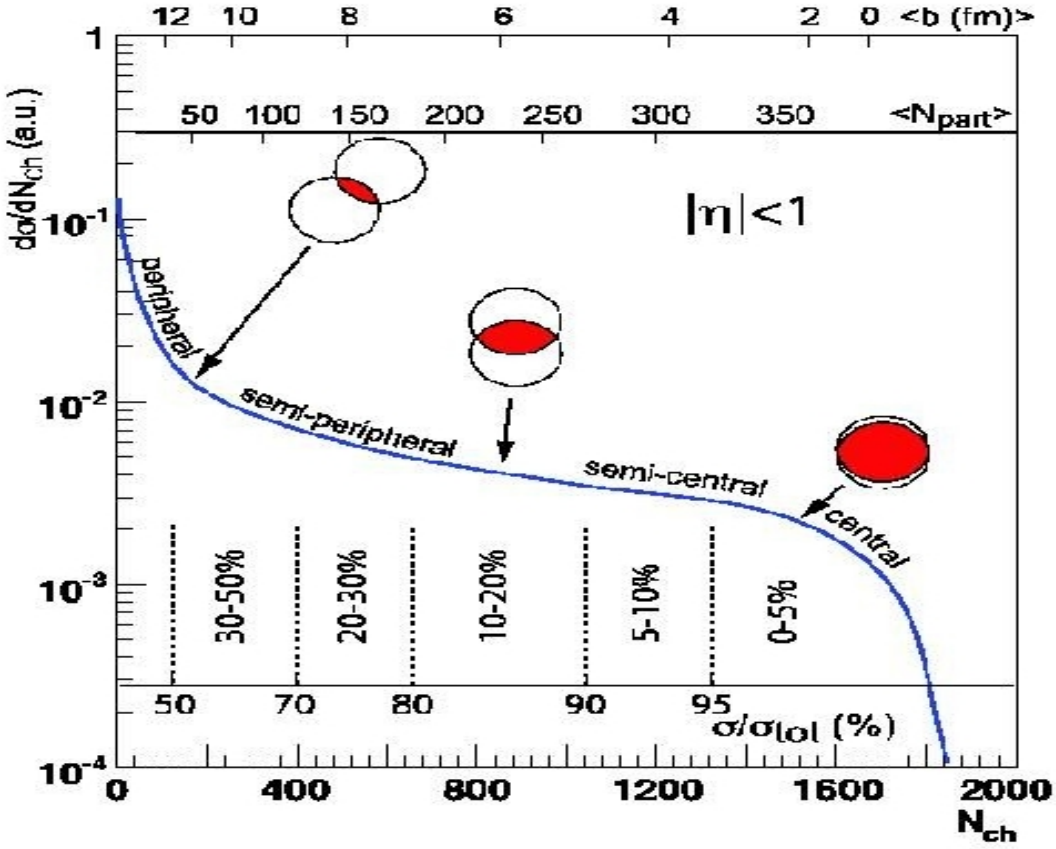

Figure 1.11: A plot of how the charged particle multiplicity, N_{ch}, changes with centrality, shown dividing the plot into vertical cuts, is shown here. The percentages of the total N_{ch} define the centrality classes as integration is performed backward from greatest to zero N_{ch}. This lets centrality scale in the same direction as impact parameter.

understanding how the physics depends on the size and shape of the hot system that is created in heavy ion collisions. A typical scenario of the idealized concept of centrality is given in Figure 1.10, and a plot of how the shape of the average nuclear overlap changes with centrality is given in Figure 1.11.

There are many things to study in heavy ion physics that depend on the centrality. Some of the most important are: quarkonia suppression, elliptic flow, QCD hydrodynamics, and jet quenching. Each of these studies depends on the centrality because each depends on a geometric quantity, which the centrality handles in the most fundamental way.

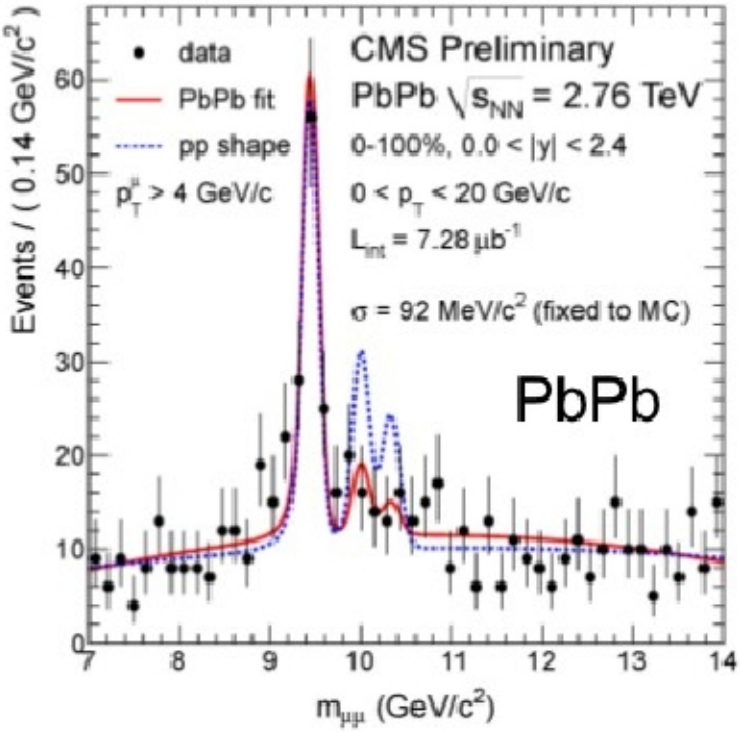

Figure 1.12: The production of Υ in pp collisions, given in blue, seems to be suppressed in PbPb collisions, given in red. The suppressed excited states of the Υ suggest that they are "melting" in a QGP [14].

J/ψ and Υ are mesons made of quarks of the same flavor, charm and bottom, respectively. They are great observables to test modifications to QCD theory because they must be modelled as color-anticolor bound states of quarks, which simplify QCD

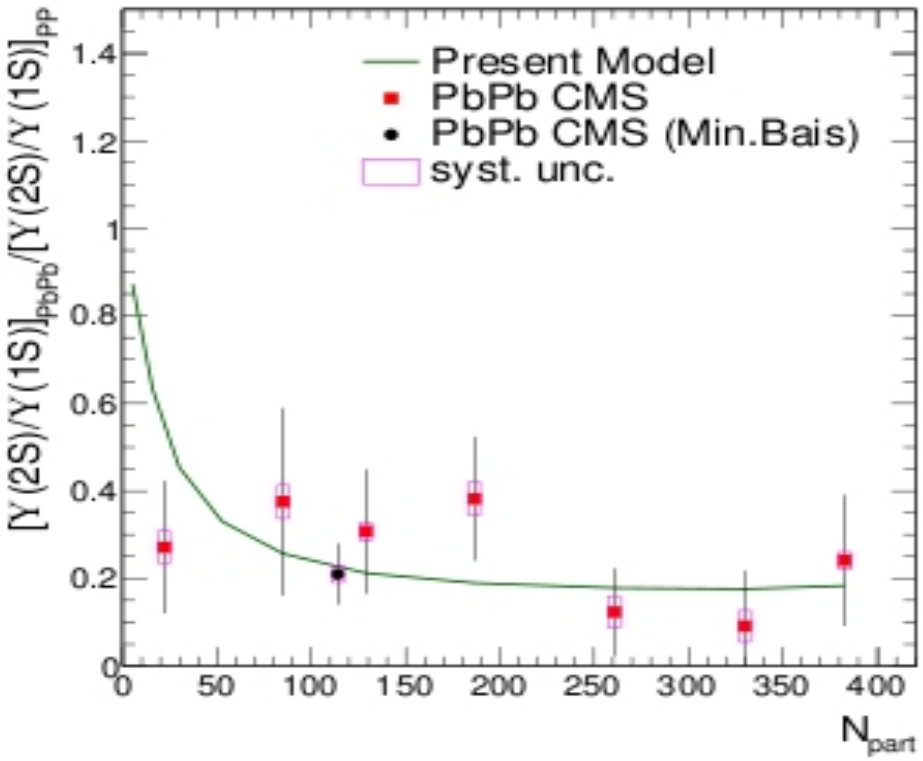

Figure 1.13: The ratio of the relative signal of the first excited state of Υ compared to its ground state in 2.76 TeV PbPb collisions to the analogous signals produced in pp collisions is shown here. This shows how suppression changes with the centrality. With better statistics, the results are expected to match the model.

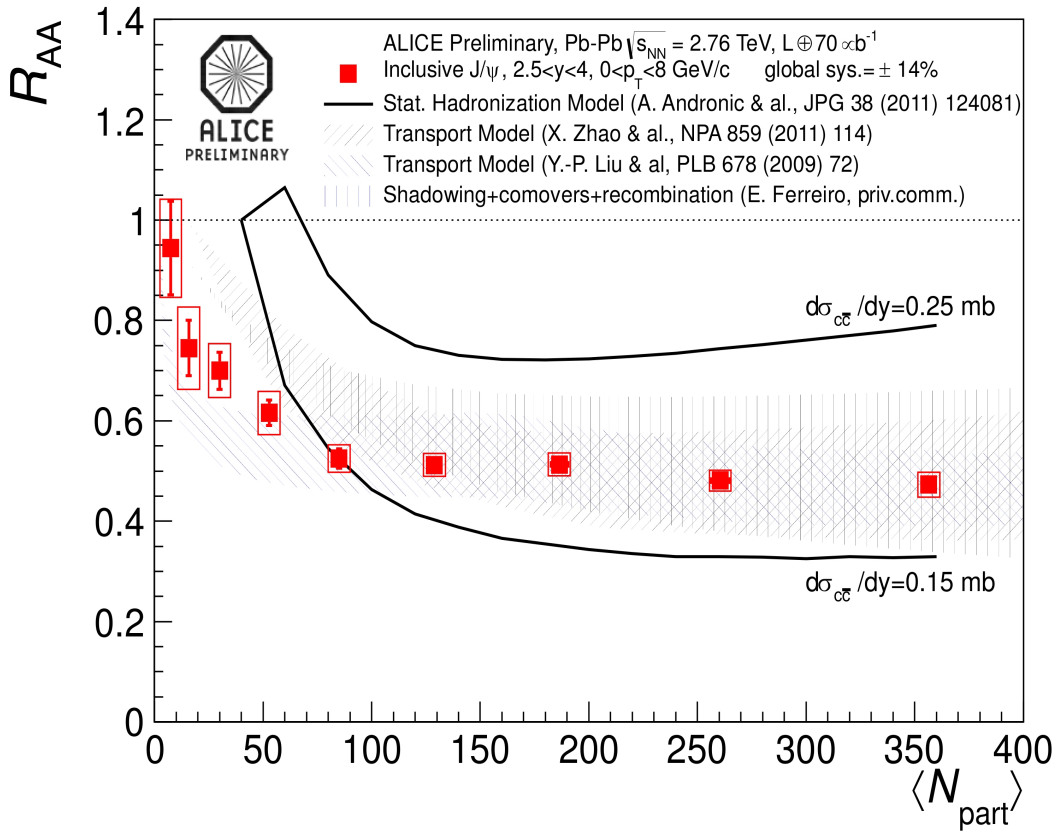

Figure 1.14: The centrality dependence of J/ψ suppression is shown here. The ratio in the excited state signals like in Figure 1.13 is not shown here. The analogous quantity, the nuclear modification factor, R_{AA}, is shown instead [15].

calculations. Mesons of this type are called quarkonia, and suppressions of their excited states have been observed in heavy ion collisions as compared to pp collisions [16, 17, 18, 15]. It is believed that this is happening because the excited states of quarkonia are "melting" in a suspected QGP. The Υ suppression is of especially great interest because the b quarks they are made of are produced in heavy ion collisions with non-relativistic momenta, due to their large intrinsic mass. This rules out pQCD theory and reveals more about the nonperturbative QCD regime of a suspected QGP. Figure 1.12 shows an example of Υ suppression in PbPb collisions. The amount of suppression, like so many other heavy ion observables, is also dependent on the centrality. This centrality dependence of the suppression is shown in Figure 1.13. Figure 1.14 shows the centrality dependence on J/ψ suppression. In Figure 1.14, $R_{AA} = N_{PbPb}/(N_{pp} < N_{part} >)$, where N_{PbPb} is the total particle multiplicity in PbPb collisions and N_{pp} is the total particle multiplicity in pp collisions.

Another important finding in heavy ion collisions is elliptic flow [19, 20, 21]. When viewed along the beam direction, particles produced in the heavy ion collisions are distributed anisotropically in momentum space. This particle flow suggests that the hot and dense matter created after the collision has a remarkable similarity in shape to that of the overlapping cross section of the two colliding nuclei. This has been called elliptical flow because the particle flow suggests that the supposed QGP created in the collision has an ellipsoidal shape. The particle flow is modelled as a proportionality to a Fourier decomposition of cosine distributions in momentum space. The second order cosine term dominates where all others approach statistical limits. The particle flow therefore can be represented by: $\frac{dN}{d\phi} \propto 1 + 2v_2[p_t]cos[2(\psi - \phi)]$ where N is the number of particles at a given azimuthal angle with the beam direction, ψ is the angle defined by the participant plane, ϕ is the azimuthal angle in the laboratory, v_2 is the second Fourier coefficient in the cosine series, and p_t is the momentum transverse to the beam direction. With this proportionality, v_2 becomes the parameter that reveals how much elliptic flow resulted from a given collision.

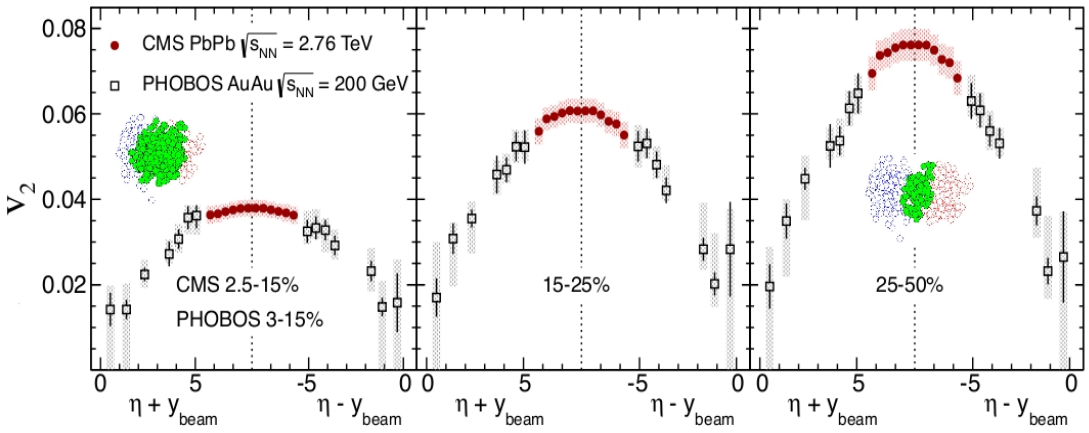

Figure 1.15: The v_2 dependence on centrality is given here. The centrality ranges are confined to each plot, and a cartoon of how the nuclear overlap looks from the Glauber model is respective to each centrality range [19].

The elliptic flow should be proportional to the eccentricity of the supposed ellipsoidal QGP. This eccentricity is given by: $\epsilon = \frac{<y^2>-<x^2>}{<y^2>+<x^2>}$, where ϵ is the eccentricity, y is proportional to the semimajor axis of the ellipsoid, and x is proportional to the semiminor axis. Since this varies with the impact parameter of each heavy ion collision, it is therefore dependent on the centrality. A plot of v_2 versus rapidity is given in Figure 1.15.

The eccentricity defines the boundary condition of QGP candidates. It can be used in various hydrodynamic analyses, and this is very important because the hydrodynamics of such QGP candidates allows for the computation of their time and volume evolution. They seem to show that the QGP is a fluid approaching the quantum limit of specific shear viscosity. This viscous quantum limit, given by the shear viscosity to entropy ratio ($\frac{\eta}{s} \sim \frac{1}{4\pi}$), deemes the QGP a "perfect fluid" [22, 23] This is a fairly loose term indicating the resemblance of the *specific* shear viscosity to the quantum limit and not the ease at which the fluid flows. As a matter of fact, the QGP is about 1000 times more viscous than room-temperature pitch. To be fair, however, the thermodynamics between pitch and the QGP is certainly not similar. Figure 1.16 shows the hydrodynamical limit of the shear viscosity as the temperature of the suspected QGP changes. Here, the centrality

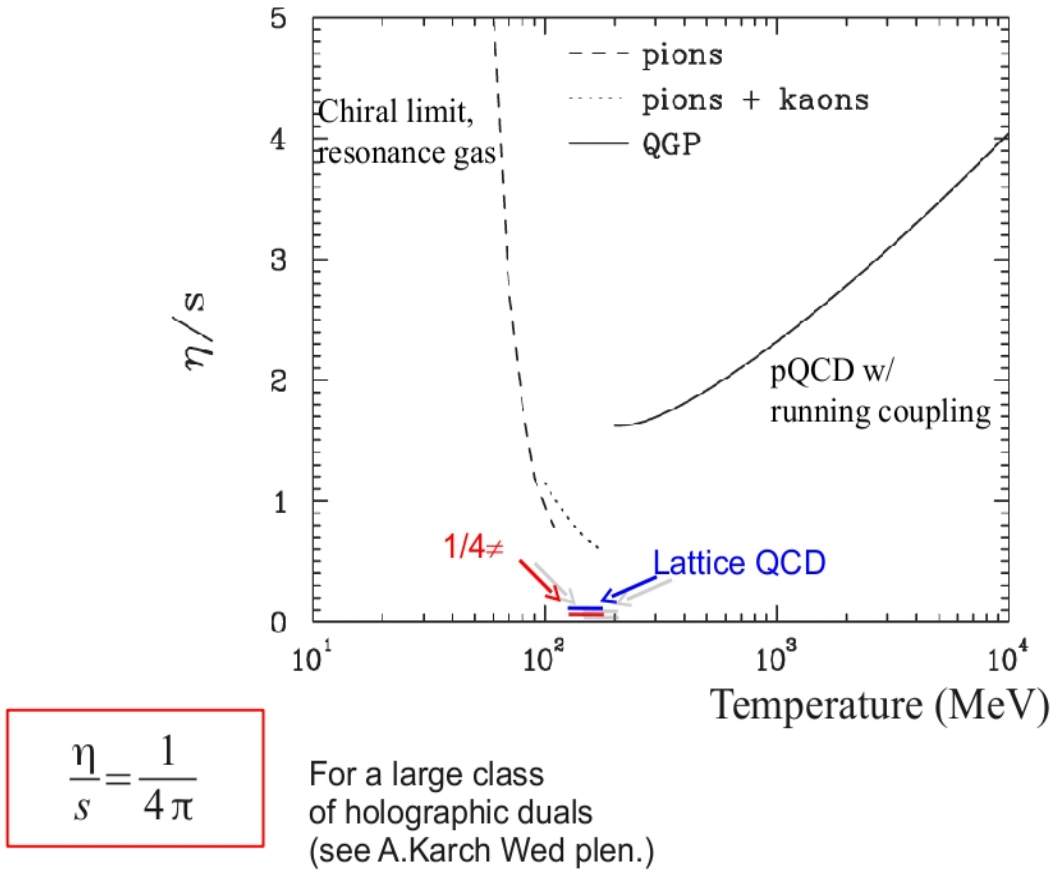

Figure 1.16: The specific shear viscosity of quark matter is shown to approach the quantum limit here [14].

helps define the boundary conditions for hydrodynamic simulations.

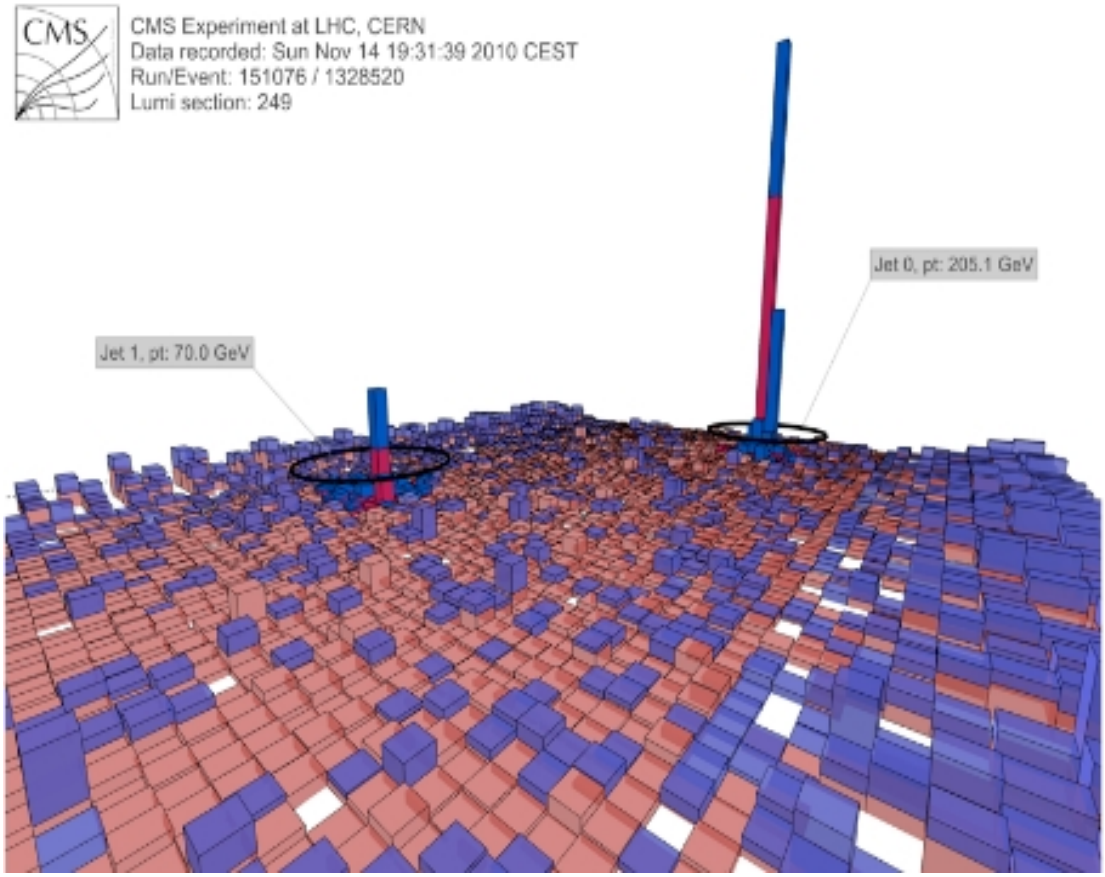

Figure 1.17: An energy deposit per solid angle map of the CMS experiment is shown here for an arbitrary time interval that captured two jets. A jet is shown to have a significantly quenched and momentum-conserving counterpart [24].

Another important discovery in heavy ion collisions is jet quenching [25, 26, 27, 28]. Jet production is well known from QCD theory, but the discovery of quenching is exclusive to heavy ion physics. Figure 1.17 shows an event display of this phenomenon very clearly for two jets. Since momentum must be conserved, it is reasonable to assume that a jet produced in one direction will be associated with a momentum-conserving jet in the opposite direction. There are various analogs for conserving momentum in rarer, higher-order jets also. However, often in heavy ion collisions, a strong jet signal is often produced with a much weaker, spread-out jet signal. This weaker jet is the quenched

jet. It is a strong suggestion that a QGP has produced quark matter that loses more momentum in one direction than its would-be momentum-conserving counterpart going in the other. The weaker jet is associated with propagating through more QGP than its momentum-conserving counterpart because, in general, it is far more likely to form jet-producing quark-quark pairs away from the centroid of the QGP than it is otherwise. The reason why this depends on the centrality is because the energy loss of the jet is proportional to the path length of its trajectory through the QGP [29]. The set of possible path lengths of jets is certainly dependent on the geometry of the QGP, and is therefore dependent on the centrality. This study, however, is still quite inconclusive because it is not known what this dependence is, even though it is known that the dependance exists. So, the centrality is definitely crucial to discovering something new about jet quenching.

Chapter 2

Scope

"Centrality is what the analysis is centered upon..."

2.1 History of Deriving the Centrality

Since the centrality is such an integral part of any heavy ion physics analysis, it is essential to make sure there is as direct a measurement of observables as possible to derive it. The standard observable used by the Compact Muon Solenoid experiment to derive the centrality is the energy deposit in the forward hadronic calorimeter (HF). The energy deposit in HF is read out as the energy flow in the transverse direction, E_T. This is done by scanning E_T summed from both sides of HF. For each event, the centrality is defined as that percentile of minimum bias events that have a larger energy in HF. Figure 2.1 shows the HF E_T distribution in PbPb collisions.

There are many interactions resulting from colliding beams at CMS. There are nuclear collisions, electromagnetic events, beam-gas events, and anomalous noise. The minimum bias events fit the minimum criteria needed to satisfy a nuclear interaction, and this is relevant to centrality because centrality is only defined for nuclear interactions. So, the minimum bias events are the fraction of events that result from a nuclear collision compared to all the events generated in CMS during colliding beams. This

implies filtering the heavy ion data through the use of the CMS trigger system to select these good events. This trigger is tuned to the timing of colliding bunches at the CMS interaction point (IP). This trigger tags events whenever there is a coincidence in both sides of HF, or the BSC. The threshold for this coincidence in HF is that each side of HF from the IP must have three towers or more registering an energy deposit of at least 3 GeV. This filters electromagnetic events or ultraperipheral collisions and beam-gas events, which, in general, are not symmetric on opposing sides of the IP. This selection is enhanced by requiring also that a vertex can be reconstructed with at least two tracks, and that they must trace to the expected collision zone through the beam paths. HF anomalous noise is also filtered by requiring that the timing of signal between its long and short length optical fibers is correlated. Triggering on events that satisfy all these criteria captures nuclear collisions.

Although the trigger can filter out the events that are not generated by nuclear collisions, it cannot tag them all. The trigger rejects events when E_T is smaller than 3 GeV in HF. This corresponds to very peripheral nuclear collisions, and the trigger is 99% efficient for the full energy spectrum in HF. Therefore, 99% of all the events expected to be generated from nuclear collisions is shown in Figure 2.1.

Energy ranges in HF are defined by equal numbers of events between centrality classes. The scheme used by the CMS experiment is to divide this evenly into 40 centrality bins each containing 2.5% of the total number of events in HF. An intuitive picture for how this is done in not 2.5% bins, but 5% for brevity, is shown in Figure 2.1. To compensate for the trigger efficency, the last centrality class handles the remainder of the events, and the rest of the centrality classes contain the fraction of all events without trigger limitations.

Centrality is inversely correlated with N_{part}, the number of nucleons that collide at least once during a heavy ion collision. With the present state of understanding, every nucleon in a heavy ion collision has two options to its role in the collision. One option is believed to leave a nucleon transformed into part of the hot, quark-gluon plasma

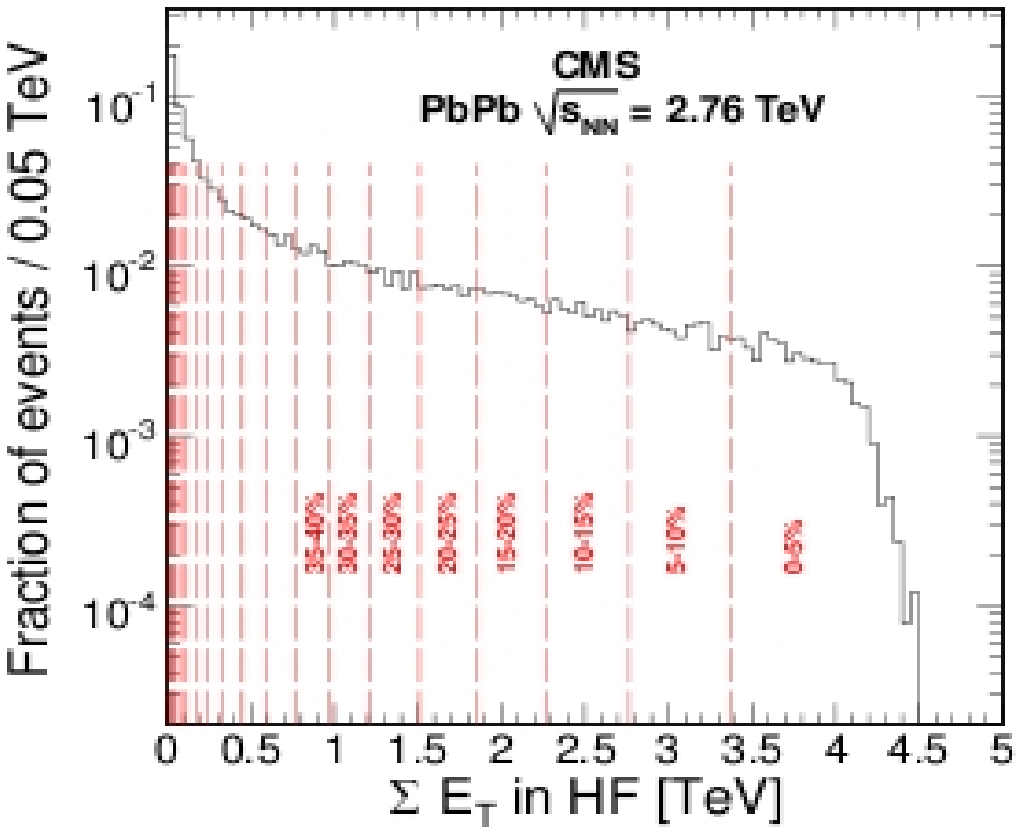

Figure 2.1: The centrality cuts against the HF energy distribution are shown here. They are simply vertical cuts to the energy flow in HF in the transverse direction [30].

that is created in the collision. The other option leaves the nucleon a non-reacting spectator that immediately leaves the reaction in the same direction as the incoming beam. It follows that any reasonable sample of the reaction products away from the beam direction provides a measure of centrality. The most central collisions produce the largest number of products because, clearly, more nucleons participate in the collision in these cases. Here, the centrality is derived using the signals from the silicon pixel detectors, and the signals from the forward hadronic calorimeter (HF).

A complementary method of determining centrality is by measuring the amount of spectator matter. For reasonably central collisions, the spectator matter is completely disintegrated into its respective protons and neutrons. In this case, the number of neutrons is a constant fraction of the number of nucleons that become spectators. A representative sample of the large angle reaction products is proportional to the number of nucleons that go into the interaction region. Because every nucleon either reacts or becomes a spectator, a plot of the number of spectator neutrons as a function of pixel counts or HF signal should be a straight line. For more peripheral collisions, for which the amount of spectator matter becomes large, some of the neutrons leave the reaction as part of small nuclei, either by not separating initially or by recombining after the reaction. In this case, the number of neutrons is no longer a constant fraction of the total spectator matter, and the line is no longer straight. The fixed target experiment, NA49, [31] derived the centrality by directly measuring all of the spectators, and is an example of how deriving the centrality can be done under ideal conditions.

One limitation of fixed target experiments, however, is in the center-of-momentum energy produced. This can be circumvented by the use of colliders, which achieve much higher energies. Heavy ion physics has made use of the Relativistic Heavy Ion Collider (RHIC) to achieve this end. Collider experiments, however, utilize large magnetic fields to bend the beams. Since spectators can be charged, some spectators are bent away from the forward detectors by the magnetic fields. This phenomenon happens when neutral spectators acquire charges after nuclear breakup by strongly interacting after

the collision, which is called coalescence. Monte Carlo analyses of RHIC experiments are reinforced by routines that take coalescence into account, but centrality analyses suffer loss of spectators in datasets. Although efforts are made to recapture charged spectators, these efforts do not measure such spectators directly.

Another major challenge colliders pose to spectator measurements is in the limited apertures available to capture them. High energy beams in collider experiments usually have very large closing distances before reaching their respective interaction points, so forward detection is usually located far downstream of the beams after their crossing. Since spectators begin their journeys at beam momentum, there is very limited space to build detectors at pseudorapidities corresponding to spectator momenta.

At RHIC, PHENIX [32] made use of two forward detectors, the zero degree calorimeters and the beam-beam counters (BBCs), to measure spectators in a collider experiment setup. The results are often plotted as a "banana plot," which, in this case, is constructed from events according to zero degree calorimeter versus beam-beam counter responses. When the banana plot is divided into even nuclear collision cross sections, the plot is organized into regions of centrality. This shows that centrality is still derivable in a collider experiment. Figure 2.2 shows how the centrality is derivable by dividing the phase space into regions of equal numbers of events.

There are actually fewer neutral spectators than expected in every banana plot. This is where coalescence becomes important, where neutral spectators often acquire charges after collisions by strongly interacting with charged spectators. The object that coalescence produces the most is the deuteron. A JAM simulation provides a "coalescence afterburner" at RHIC to take this effect into account [34]. It was estimated that up to 30% centrality, the number of neutral spectators reaching the ZDC is in good agreement with the JAM simulation. Even though not all of the neutral spectators in peripheral collisions make it to the ZDC, the correlations between forward spectators and transverse momentum particles are also correlated with centrality. So, neutral spectators are still good observables for deriving the centrality.

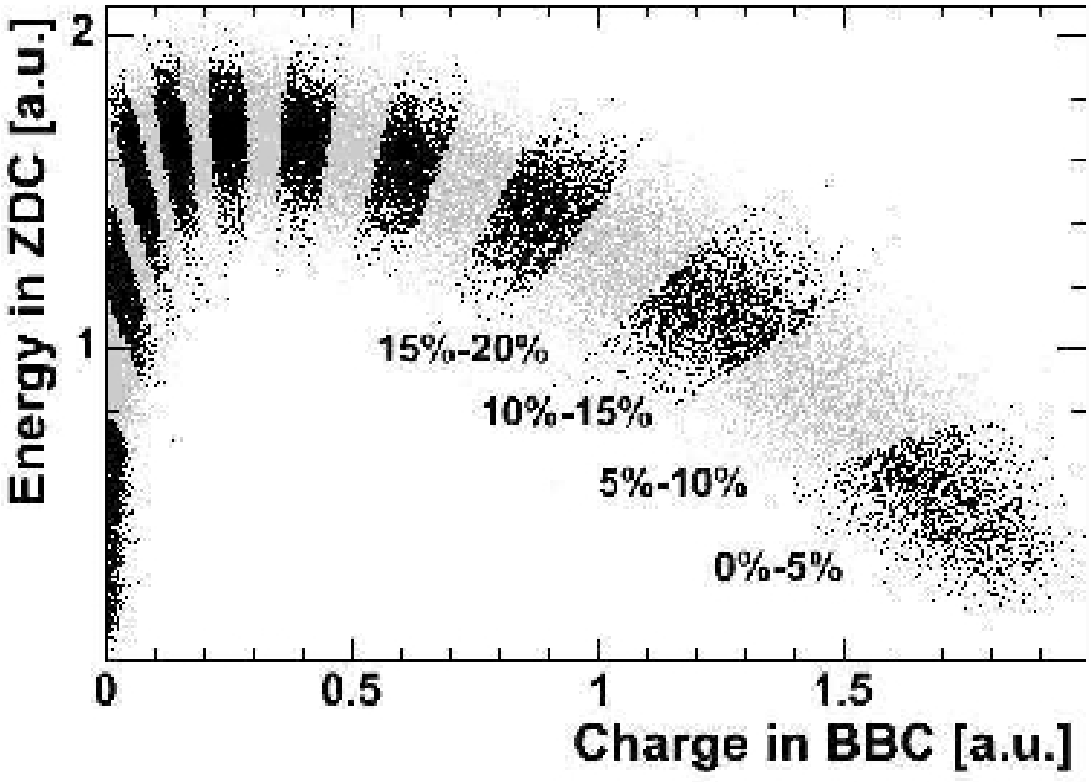

Figure 2.2: A plot of the ZDC energy versus beam-beam counter (BBC) multiplicity (up to y = 2.0, where y is the rapidity) from the PHENIX experiment is shown here. This measurement is somewhat analogous to ZDC versus pixel multiplicity at the CMS experiment for use in obtaining a centrality measurement there. Therefore, this plot is an historical standard that the CMS centrality measurement at CMS using ZDC is based upon [32]. The plot is taken from [33].

The implication of measuring neutral spectators to derive the centrality holds as long as it can be shown that results from previous generation experiments that measured them apply to the current physics constraints that hold at the Large Hadron Collider (LHC). At RHIC, ^{197}Au nuclei were collided up to $\sqrt{s_{NN}} = 200$ GeV. These gold nuclei are spherical, and the charges within them are distributed uniformly. At the LHC, in this analysis, ^{208}Pb nuclei are collided at $\sqrt{s_{NN}} = 2.76$ TeV. These nuclei are also spherical with uniformly distributed charge. When the charged particle multiplicity is plotted with N_{part} for heavy ion collisions at RHIC and also LHC, it can be shown that the physics looks very much the same. As long as the data from RHIC is weighted by the energy density increase at the LHC, the charged particle multiplicity looks the same [30]. This means that moving to a new energy regime will not prevent previous analysis techniques of spectator matter from staying valid. This is seen very clearly in Figure 2.3.

Deriving the centrality with the HF detector inevitably implies measuring both components of momentum, namely transverse momentum, p_t, which is perpendicular to the beam momentum, and forward momentum, p_z, which is along the beam momentum. It would be useful to separate both of these momentum components in another measurement. Although it is not practical to try this with p_t completely, it is possible to measure particles that are dominated by p_t compared to p_z in the pixel detector. The pixel detector also does not detect all particles, only charged particles and some photons which convert into electron-positron pairs. However, it is known that the number of charged particles is directly proportional to the total number of particles in the collision. It is also known that the total number of particles produced in each collision is proportional to the total energy of the collision. This means that the total pixels registering a charged particle hitting the pixel detector in each heavy ion collision is proportional to the energy deposit in its pseudorapidity coverage. Naturally, this means that finding correlations in the signals between the zero degree calorimeter (ZDC) and the pixel detector can be used to sort events by the centrality within very reasonable constraints

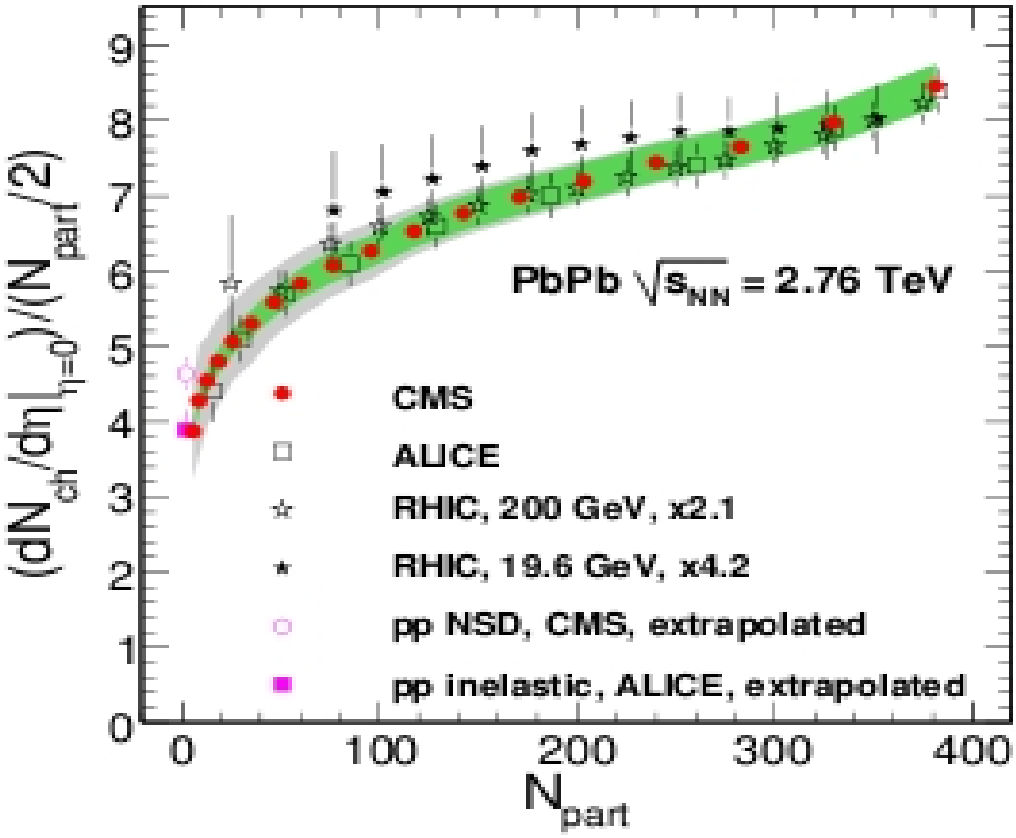

Figure 2.3: A comparison of the charged particle multiplicity and N_{part} is shown here. With a proper weighting of the energy density, this shows that previous generation experiments reveal an identical centrality dependence within identical analyses [30]. The green bands show the systematic uncertainties affecting the scale of the measurements, and the gray bands are the total systematic uncertainties.

on p_t and p_z.

The pseudorapidity, η, range of the pixel detector is low enough at $|\eta| < 2.5$ compared to the ZDC at $|\eta| > 8.3$ to separate the energy deposits in the ZDCs and the pixel detector. This effectively keeps the momentum of particles detected by the pixel detector reasonably orthogonal to the momentum of the particles detected by the ZDCs. One of the weaknesses of deriving the centrality from the HF detectors is that they cannot directly measure spectator neutrons. Since they fly by at beam momentum per nucleon after each collision, they contain essentially zero p_t. The ZDCs are not only ideal for measuring spectator neutrons, but exclusively measure them. This means the advantage of using the correlation between the ZDC and pixel detector signals is twofold. The separation of both orthogonal components of momentum p_t and p_z are harnessed from two separate detectors, and the direct measure of spectator neutrons in the ZDCs is utilized.

2.2 Research Aim

This research aims to use the correlation in the ZDC signals and pixel multiplicity to sort heavy ion collision events by their centrality. A direct display of how the spectator neutrons fit into the centrality analysis is also made after the events are sorted by centrality. This display is plotted as a neutron spectrum for the ZDCs. Comparisons are made between the centrality derived from the HF detectors and the centrality derived from the ZDC versus pixel correlations. The same minimum bias trigger criteria is used as in the HF centrality analysis to make the comparison as transparent as possible.

Chapter 3

Experimental Setup

"No. They are not zero degree calorimeters because the LHC tunnel is cold..."

3.1 Large Hadron Collider

The Large Hadron Collider (LHC) [35] is the latest generation accelerator facility that is designed to accelerate protons up to 7 TeV per beam. The design luminosity if the LHC is $10^{34} cm^{-2} s^{-1}$. On the 21st of April in 2011, the LHC broke the luminosity record of its previous holder, the Tevatron, by achieving $4.67^{32} cm^{-2} s^{-1}$. It is essentially a conversion of the Large Electron-Positron collider (LEP) and is located at the European Center of Nuclear Research (CERN). The LHC proton beam energy has reached 4 TeV per beam as of the summer of 2012. It is a synchrotron accelerator which uses the timing of Radio Frequency (RF)-cavities to "kick" particle beam bunches at intervals that allow the bunches to all achieve the same momentum once the acceleration process is complete. It stores beams in a circular ring, so superconducting magnets are employed in the LHC tunnel to steer the beams. The circumference of the ring is 27 km and is located deep underground. With these dimensions, at the maximum beam energy, the main cryogenic dipole magnets that keep the beams on circular paths have been

designed to generate fields of up to 8.3 Tesla.

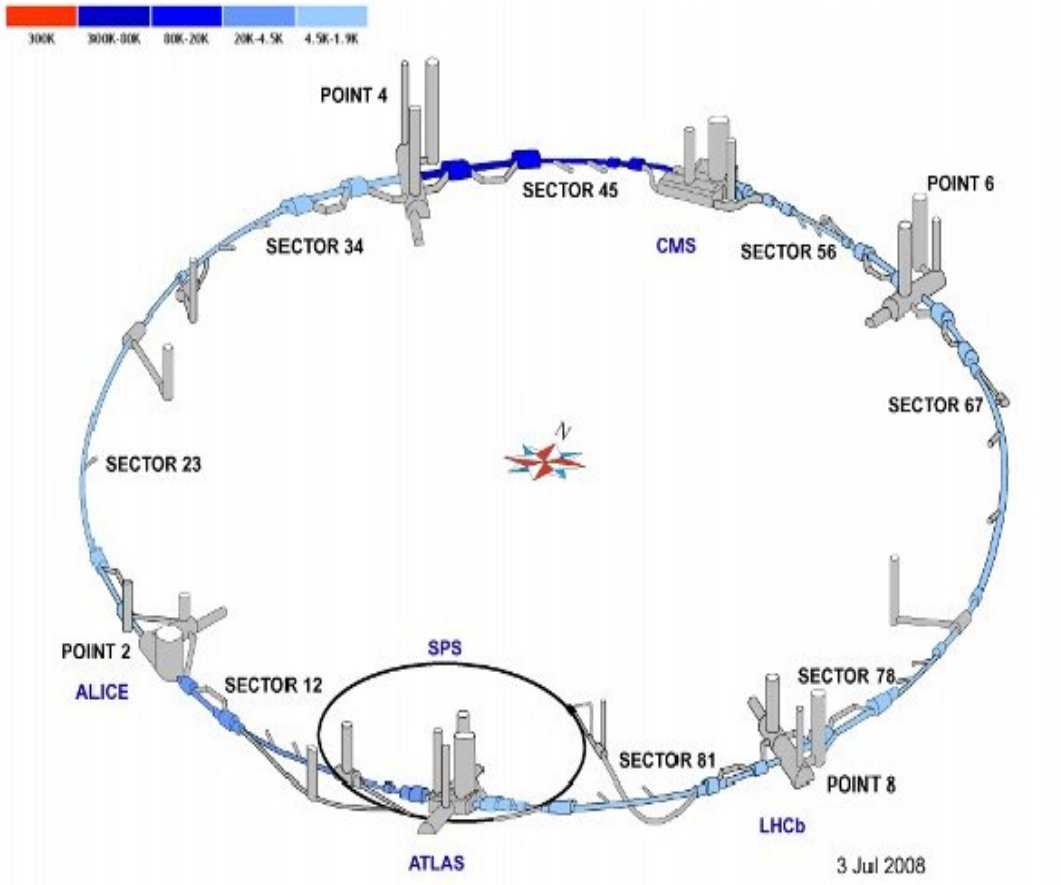

Figure 3.1: The LHC is shown here. The locations of each experiment are labeled.

The LHC houses four main large experiments measuring the most energetic man-made collisions to-date. They are ATLAS (A Toroidal LHC Apparatus) [36], ALICE (A Large Ion Collider Experiment) [37], LHCb (LHC-beauty) [38], and CMS (Compact Muon Solenoid) [39]. CMS is at the heart of this analysis, so the focus of this chapter is aimed at CMS. A picture of the orientation of the LHC experiments is given in Figure 3.1.

The LHC is fed by several older accelerators at CERN before servicing all the experiments in it. A depiction of this is given in Figure 3.2. The first step is the LINAC, or linear accelerator. It produces proton beams of 50 MeV or Pb ions at 4.2 MeV per nucleon [40]. This is fed into the PS, or Proton Synchrotron [41]. Combined with the

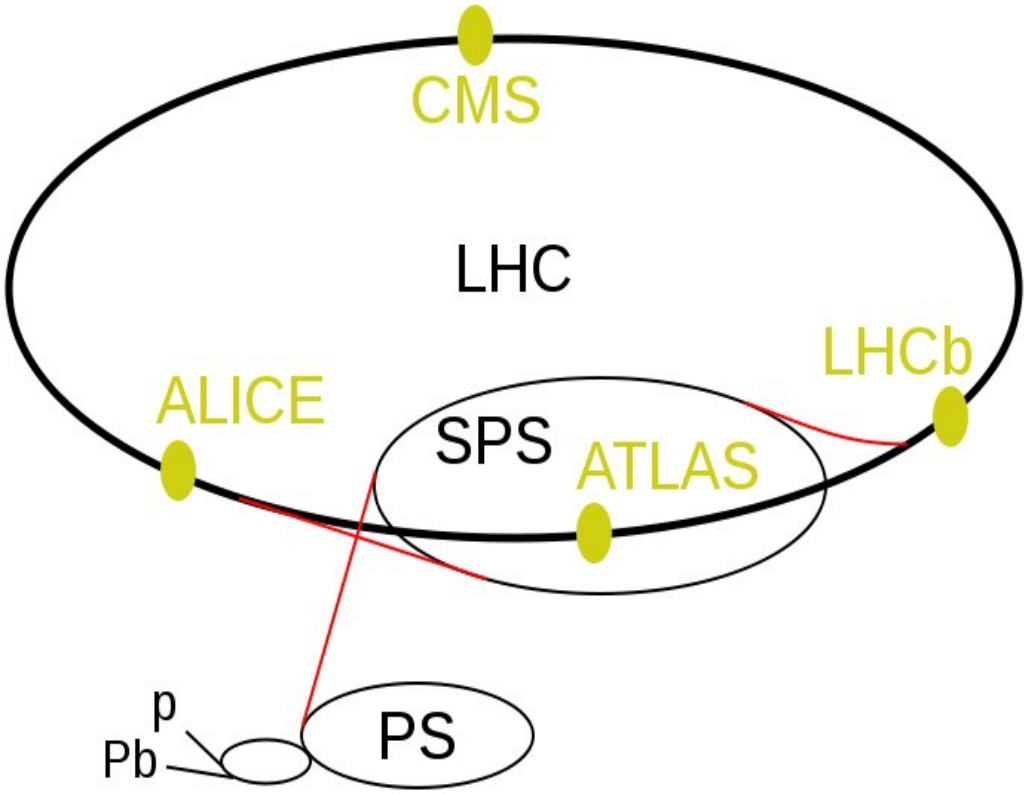

Figure 3.2: An assembly of the accelerators feeding the LHC is shown here.

booster, the PS can accelerate protons into the next section of the LHC beam injection, the Super Proton Synchrotron (SPS), at 28 GeV [42]. After this, the SPS can accelerate protons to 450 GeV before they are finally injected into the LHC.

3.2 Compact Muon Solenoid

The LHC contributes to the heavy ion physics by incorporating Pb-Pb beams into the program. The center-of-mass energy, given by one of three Mandelstam variables: $\sqrt{s_{NN}}$, at the LHC is a factor of 14 higher than RHIC. $\sqrt{s_{NN}}$ is essentially double the energy per unit nucleon in a reference frame where the forward momentum of colliding beams sums to zero, which makes $\sqrt{s_{NN}}$ an invariant. This is not the total momentum of the beams in this frame, because the transverse momentum of the beams is slightly non-zero due the crossing angle momentum necessary to cross the beams. The Compact Muon Solenoid (CMS) measures observables in this next generation of heavy ion physics while utilizing its signature 3.8-Tesla field generated by the 6-meter-radius superconducting solenoid within it. The relevant subsystems of CMS that contributed to this analysis were the ZDC, the forward hadronic calorimeter (HF) [43], the beam shower counters (BSC) [43], and the pixel detector, which is a part of the inner silicon tracker [44]. The coordinate system used in CMS is defined by the x-axis, which points positively to the center of the LHC ring, the y-axis, which points up, and the z-axis, which points in the counterclockwise beam direction when observing through the y-axis. The interaction point (IP) at CMS is the place where most of the beams collide at CMS. The angular coverage of each subsystem of CMS is parameterized by the pseudorapidity, η, where $\eta = -ln[tan[\theta/2]]$ and θ is the angle from the z-axis pivoted from the IP. A cartoon of the arrangement of these and more subsystems at CMS is given in Figure 3.3. A transverse slice of CMS to show the relevance of this arrangement to particle identification is given in Figure 3.4.

The first layer of CMS surrounds the IP and is called the silicon tracker [44]. Here,

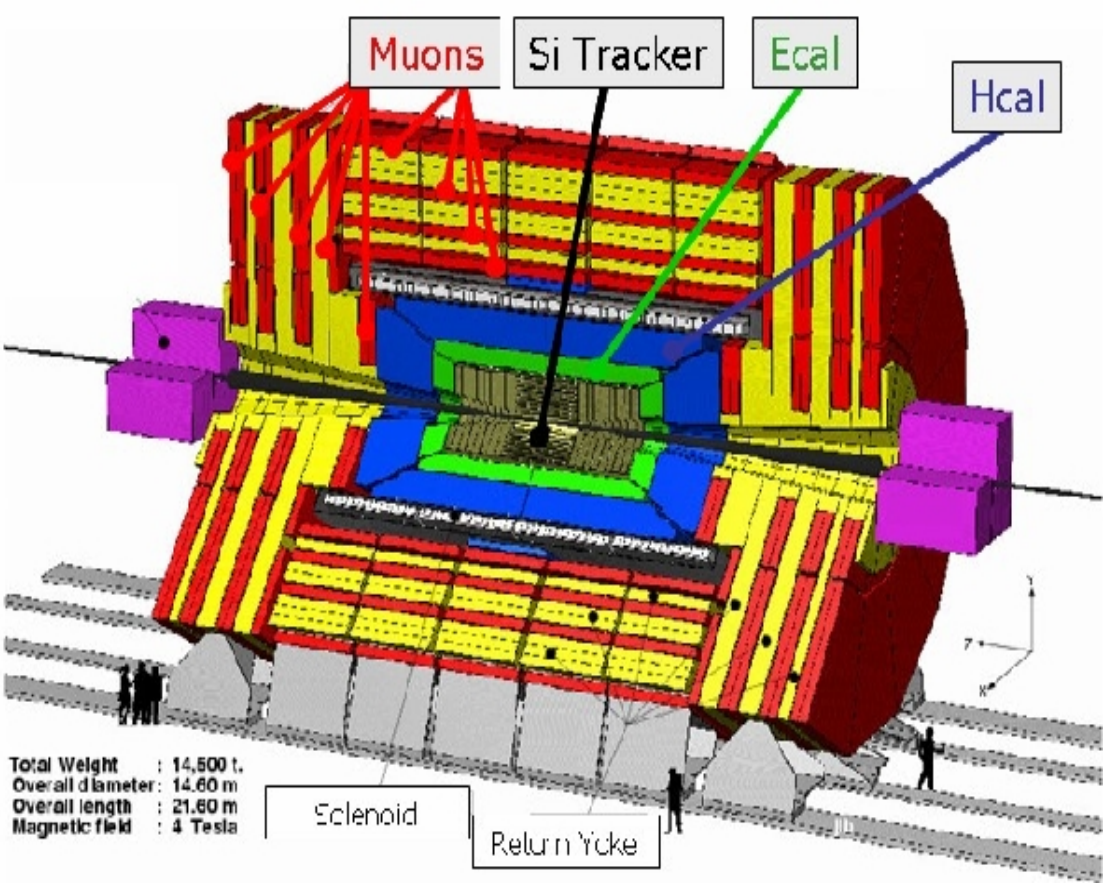

Figure 3.3: A cutaway view of CMS is given here. The purple region also shows HF, a forward hadronic calorimeter. CASTOR and the ZDCs are not shown here.

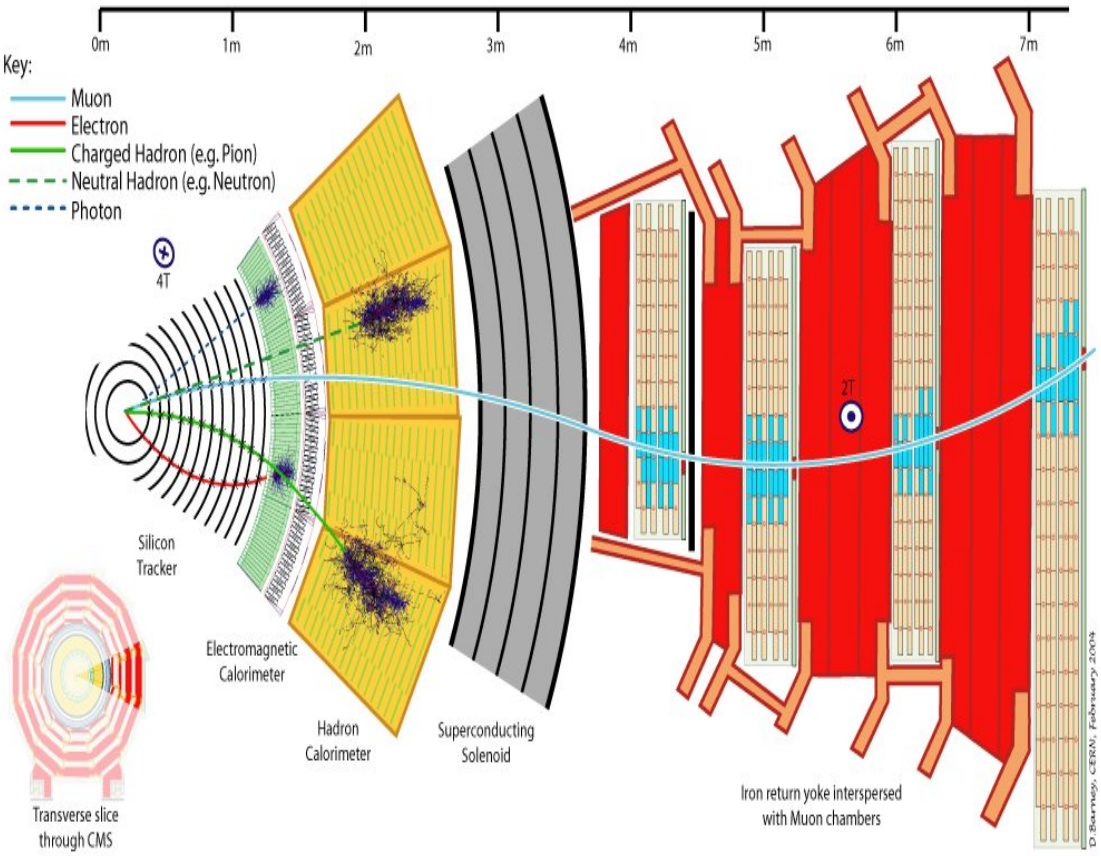

Figure 3.4: A transverse slice of CMS is given here. Some examples of interactions of different particle types are color-coded.

silicon semiconductor plates track particle trajectories on the way into the next layer of CMS, and the tracks are traced to their interaction vertices. The curvatures of particle trajectories identify them with a charge-to-momentum ratio. Neutral particles will remain in straight trajectories. These trajectories and vertices, combined with the interactions at each subsequent calorimeter identify particles produced from the IP. In all, there are 76 million channels in the silicon tracker.

The pixel detector is essentially the first three layers of the silicon tracker. It is a series of 66 million silicon pixels arranged in a cylinder coaxially with the beampipe. This means most of the tracker channels are alloted for the pixel detector at one pixel per channel. The η coverage of the pixel detector is $|\eta| < 2.4$. In this analysis, the pixel detector served to provide only the number of pixels that registered a hit in each event. This is the number of charged particles that registered a hit in a single pixel, called the pixel multiplicity. This quantity is proportional to the transverse energy flow into the pixel detector.

HF is a tiled steel and quartz fiber heterogenous Cherenkov calorimeter with a maximum axial radius of 1.3 meters. It is situated 11.2 meters from the interaction point, and this gives it a pseudorapidity coverage of $3.0 < |\eta| < 5.2$. The steel plates within are divided in azimuthal angular wedges of 20 degrees each. Further segmentation in the η direction results in a $(\delta\eta \times \delta\phi) = 0.175 \times 0.175$ solid angular resolution with both units in radians. The steel plates are absorbers that are grooved to fit quartz fibers which route Cherenkov light to photomultiplier tubes. The design is similar to the ZDC, except the ZDC utilizes tungsten absorbers instead of steel.

The BSCs are scintillator tiles designed for providing coincidence triggers. They are located at both 10.9 meters and 14.4 meters on either side of the IP. These tiles served as the basis for the minimum bias trigger used in this analysis.

3.3 CMS Zero Degree Calorimeters

The ZDCs are a pair of detectors situated 140 meters downstream of the interaction point at CMS, and are situated between the beampipes on either side. It is clear that at 140 meters away from the IP, the ZDCs measure exclusively forward neutral spectators. The ZDC is a sampling Cherenkov heterogeneous quartz-based calorimeter with tungsten absorbers. It consists of an electromagnetic (EM) section of 33 tungsten plates sandwiching quartz fiber that routes Cherenkov light to phototubes. The EM section has 1.7 centimeter segmentation in the x-direction, completing 5 segments. The last section of the ZDC is the hadronic section which consists of 24 tungsten absorbers tilted 45 degrees from the vertical towards the outgoing beam direction. This is an attempt to match the Cherenkov angle of the shower lightcone. The effective radius of the ZDC is about 4 cm. In this analysis, in order to capture as much energy from forward neutral spectators as possible, both sections of the ZDC detector are used to measure events [39].

In order to measure spectator neutrons, and even forward photons, the design of the ZDCs must have the ability to overcome several challenges. The first challenge is the limitation due to physical space. The ZDCs are situated on either side of the z-dimension of CMS, 140 meters away from each side of the IP. This distance actually places the ZDC inside the LHC tunnel, which is a unique location for any detector within the CMS experiment. A diagram of this setup is given in Figure 3.5.

The ZDCs are sampling Cherenkov detectors, which collect particle showers' Cherenkov light from incoming high-energy particles. A schematic of a single ZDC is given in Figure 3.6 [45]. These particles produce showers that exceed the speed of light in quartz fibers, which causes the particles to release the light. The ZDCs are situated on either side of the z-dimension of CMS, 140 meters away from each side of the IP. Such a location certainly creates additional challenges. Also, this distance away from the IP assures not only the detection of particles produced at zero degrees, but also allows for

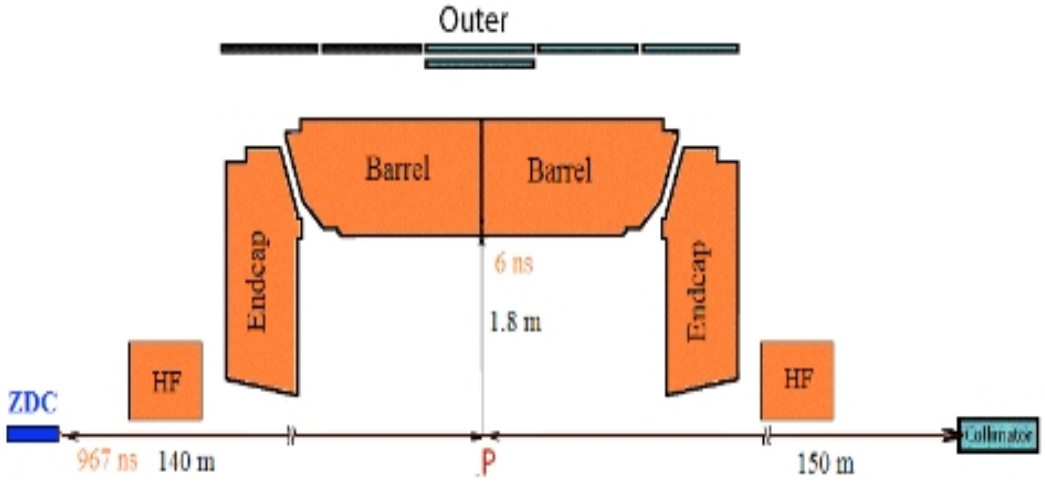

Figure 3.5: The location of one ZDC relative to the CMS experiment is given here along with the location of a beam collimater inside the tunnel. The hadronic calorimetry system in CMS is only included in the diagram for brevity.

exclusive neutral particle detection. All of the incoming charged particles from the IP at CMS are curved away from the ZDCs by superconducting magnetic dipoles that steer the beams together. Since the energy of the charged particles must be equal to or less than the beam energy upon production, they will never make it to the ZDCs.

The ZDCs are dual calorimeters consisting of an electromagnetic section and a hadronic section. The electromagnetic section, considering its location from the IP, exclusively picks up forward photons. These forward photons produce purely electromagnetic showers in the tungsten and the light is picked up by the quartz fibers sandwiched in-between the tungsten plates. The ZDC electromagnetic section is 19 electron radiation lengths long. On average, each photon travels one radiation length before converting into an electron-positron pair. This essentially destroys the photons. This length is substantiated by tungsten plates where quartz fibers are sandwiched in-between. This tungsten is divided into 33 sections along the z-direction.

In addition to the z-direction dimensions in the electromagnetic section, there is segmentation in the x-direction. The fiber is divided into five 17 millimeter strips

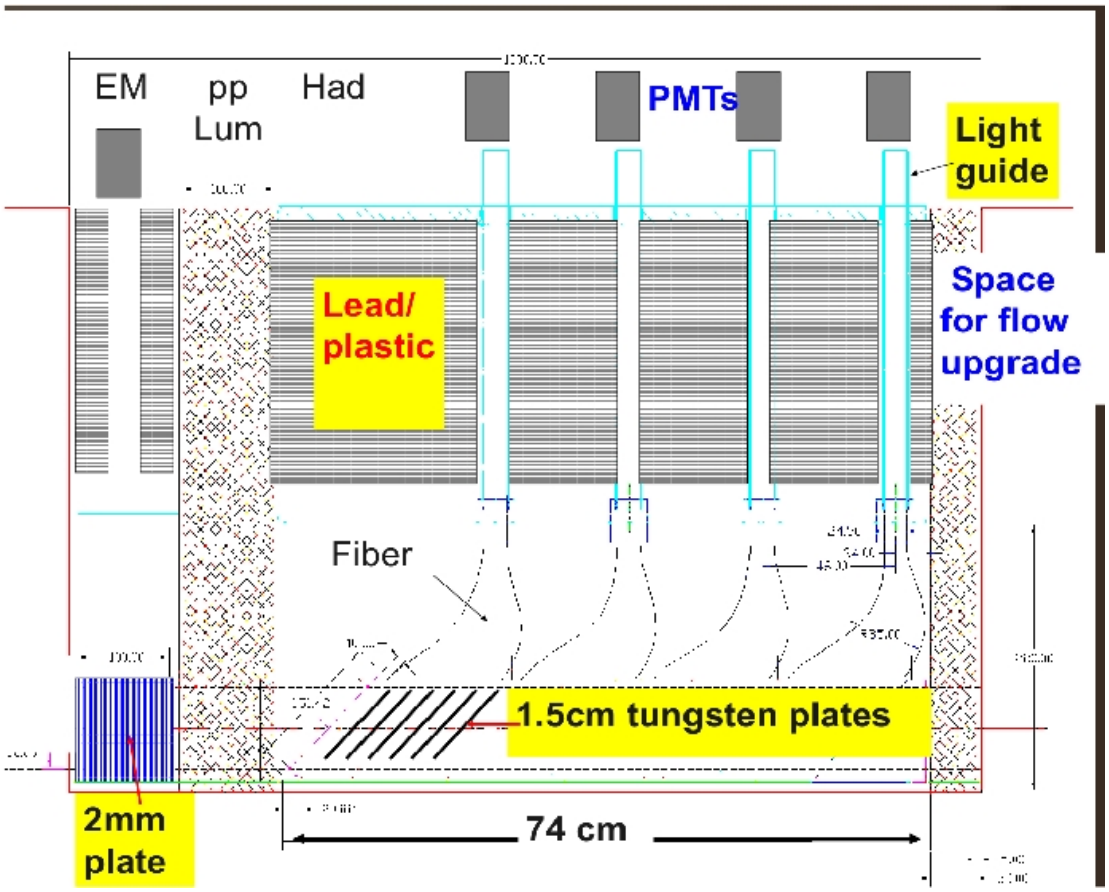

Figure 3.6: A schematic of a single ZDC is given here. Note that there are actually five EM section PMTs unlike the single PMT representation shown here to save drawing space. The z-direction runs horizontally and coplanar to the schematic. The "pp Lum" section is a placeholder for the BRAN Luminosity Monitor, which is not a part of the ZDC.

stacked in the x-direction. A picture of how the ZDC channels are situated in the CMS coordinate system is given in Figure 3.7. So it is not possible to bend the fibers with the space constraints (the ZDCs situated very tightly between the beam pipes) to achieve y-segmentation in the same fashion. However, processes that are dependent on the x-direction can be measured where they are warrented. The location of the ZDCs relative to the beam pipes is given in Figure 3.8. This means that there are five phototubes in the electromagnetic section that are dedicated to each segment in the x-direction.

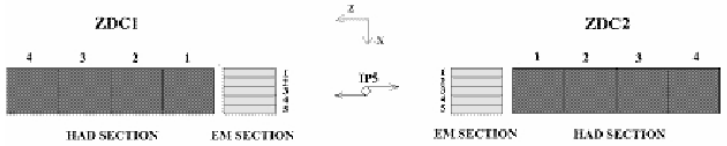

Figure 3.7: The arrangement of both ZDCs is shown here relative to the CMS coordinate system. The y-coordinate points out of the page.

The hadronic section is designed to detect incoming forward neutrons, the only neutral hadrons to be statistically detectable by the ZDCs at this distance from the IP. The hadronic section follows the electromagnetic section in the z-direction path away from the IP. This is necessary because the 19 electron radiation lengths of the electromagnetic section make one hadronic interaction length. It is applicable here to actually define this section's length in terms of neutron interation lengths because the neutron produces very high momentum leading fragments. This means that the electromagnetic section produces a neutron preshower en route to the hadronic section, where the majority of the light from forward neutrons is collected. It is unfortunate that there is a space between the two sections for luminosity monitoring because this produces some shower leakage in the x and y-directions. However, this can be worked out with calibration. When the length of the hadronic section where the tungsten is not located is subtracted away from the total length of the hadronic section, this yields a true length of 5.6 hadronic interaction lengths. Effectively, only the tungsten counts for this length. This length therefore minimizes leakage in the z-direction, and can

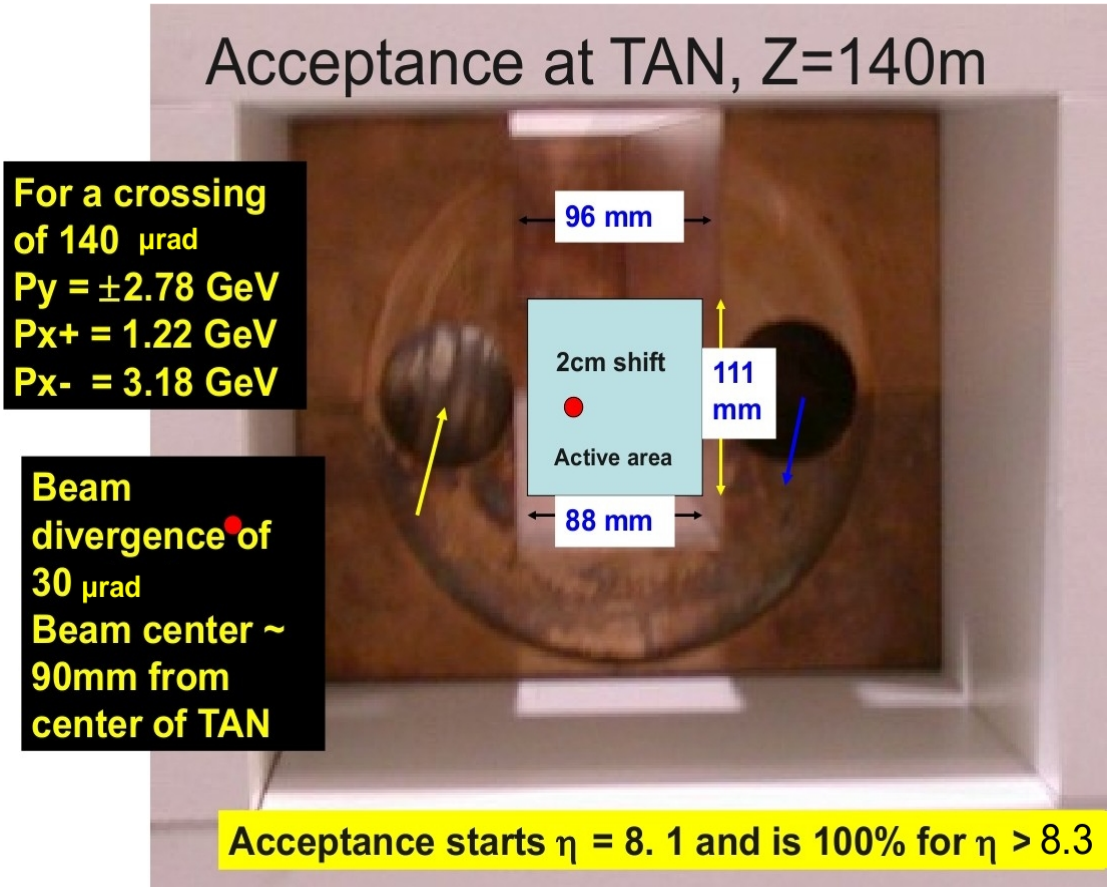

Figure 3.8: The ZDC location relative to the beam pipes is shown here. The ZDCs take up all the possible space in the x-direction.

certainly be calibrated for. This length is substantiated by 24 45° tilted tungsten plates sandwiched in-between the quartz optical fibers. This tungsten and fiber sandwiching in both ZDC sections is shown in Figure 3.9.

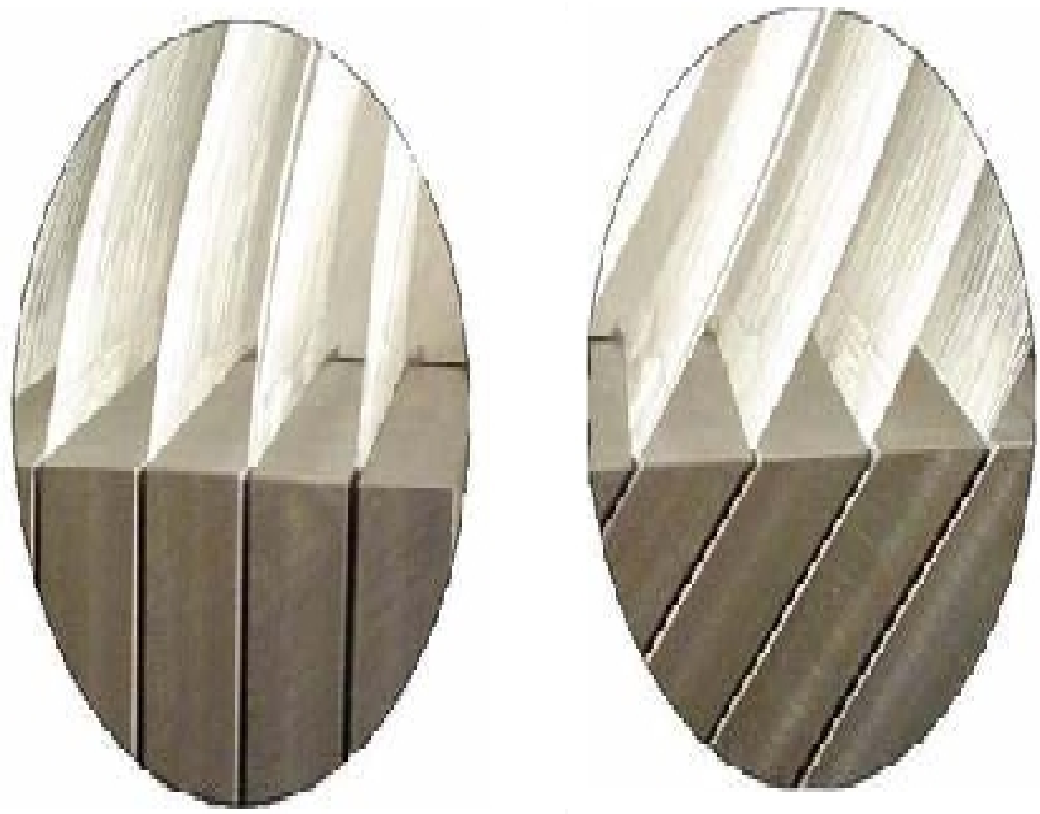

Figure 3.9: A photo of the tungsten and quartz fiber sandwich is shown here. On the left is the vertical setup of the EM section, and on the right is the setup of the 45 degree slanted arrangement of the hadronic section.

The design of both the main sections of the ZDCs is based on the theory of how electromagnetic and hadronic showers work. Purely electromagnetic showers are generated by photons and leptons. In purely electromagnetic showers from photons, the photons are transformed in the calorimeter absorbing medium and produce annihilation pairs of electrons and positrons. These leptons interact electromagnetically again and produce more annihilation pairs, resulting in a shower of these leptons. This continues

until the energy and momentum of the incoming photon is exhausted, or the lepton shower leaks out of the calorimeter. In electromagnetic showers produced by leptons, the shower is generated by the same mechanism as the shower cascade from photons. The field from the showers of leptons is substantiated by photons, the electromagnetic force carrier. These photons are converted into the annihilation pairs that drive the showers in every case. This reaction is always expected to be highly linear with incident particle momentum because the photons are essentially destroyed when they are converted into annihilation pairs. This means that for every photon, only one annihilation pair is produced during its destruction. The shower can cascade into more annihilation pairs with the interaction of the absorbing medium by more photons, but those photons are *also* destroyed in the production of more annihilation pairs.

Hadronic shower generation is more complicated, and are caused by hadrons interacting with a calorimeter's absorbing medium. They are actually combinations of electromagnetic events and hadronic events, so there is a lot more particle generation in every shower for that reason alone. For all the hadrons, there is still an electromagnetic component of the showers generated even by neutral hadrons. The majority of the energy in hadronic showers is initially carried by pions. One third of these pions, on average, are neutral pions. These have a short half-life of about 10^{-17} seconds and are converted into two gamma rays. These gamma rays behave like the photons in electromagnetic showers and generate such events accordingly. What is different about the neutral pions, however, is that they are hadrons themselves. The shower particles are of such low energy that they can no longer create more particles. This holds true for the other two-thirds of the particles, mostly charged pions, which last longer at a lifetime of about 10^{-8} seconds, and so they create more hadronic showers. This makes hadronic showers much longer than electromagnetic showers because the hadronic response is self-replicating and the nuclear force is short range [47]. This is also further complicated because the incident hadron, always a neutron in this case, is not destroyed either, and keeps generating more pions. This self-replicating behavior of hadronic showers causes

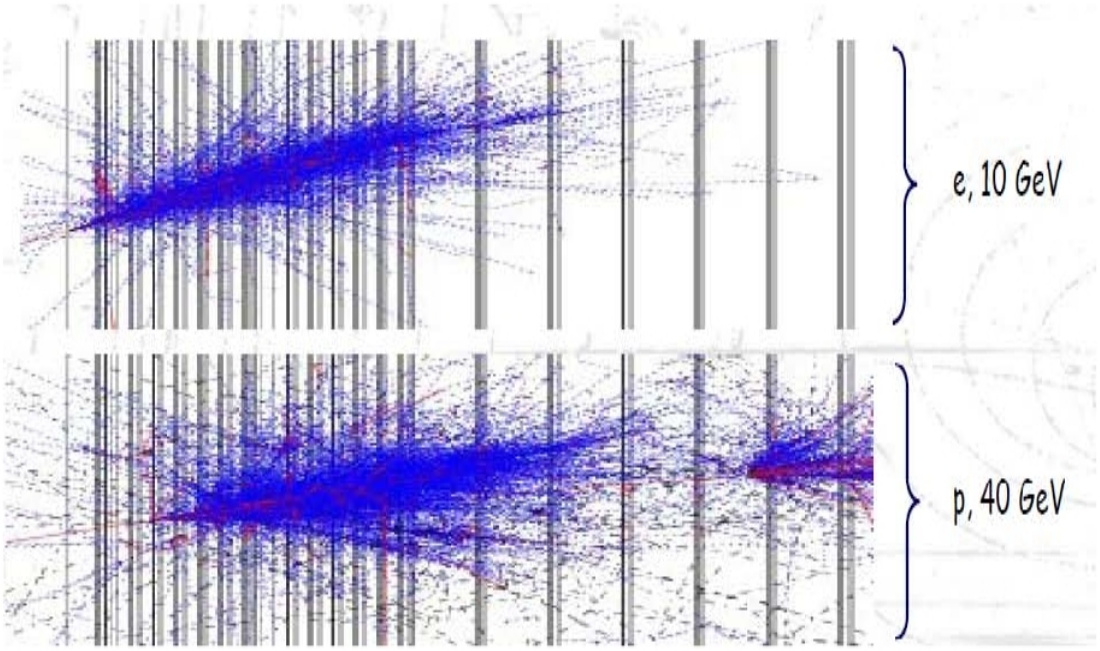

Figure 3.10: A cartoon is shown here of a purely electromagnetic shower, on top, and an hadronic shower, on the bottom. They are both from simulations. The purely electromagnetic shower is from an electron, and a proton forms the hadronic shower. Note that the hadronic shower has both an electromagnetic preshower and a hadronic shower [46].

the momentum response of the ZDCs to hadrons to be somewhat non-linear. A cartoon of how this works is given in Figure 3.10.

The way both types of particle showers work motivates two key features of the design of the ZDCs. The electromagnetic section is placed in front of the hadronic section in order to create a preshower that effectively makes the hadronic section longer. This is important to minimize the shower leakage in the beam direction of incident neutrons. The second feature is to make the hadronic section of the ZDCs much longer than the electromagnetic section, because of the self-replication of hadronic showers. In the electromagnetic section, the neutron interaction length is nearly as long as the length of the electromagnetic showers.

The ZDCs are from the heterogenous class of calorimetry, which means that the absorbing medium and the active medium are separate. The absorbing medium is made of tungsten chosen for its density to maximize the production of particle showers. Surely, depleted uranium has been noted for its density in past calorimeter designs, but shipping it intercontinentally would certainly cause a stir with customs officials. Not-to-mention, tungsten is simply safer to work with and easier to machine into shapes that are useful for the current design. Perhaps the most important reasons to avoid depleted uranium are that it is flammable and poisonous. The amount of logistical difficulties with depleted uranium outweigh the density benefits over tungsten by quite a lot. The active medium is the material that produces the Cherenkov light. In the case of the ZDCs, this is quartz optical fiber. The quartz fiber receives particle showers from incoming spectators that pass through the tungsten, and the particle showers exceed the speed of light in the quartz. This is possible because quartz has a refractive index greater than one, and in this case, is very close to $\sqrt{2}$. This is an important feature of the active medium because of the way the Cherenkov angle is defined, which for the ZDC fibers, is 46°. Even though it is not exactly $\sqrt{2}$, it is easier to machine metals into 45°, which is close enough.

The Cherenkov angle is given by: $\cos\theta = \frac{1}{n\beta}$, where θ is the Cherenkov angle, n is

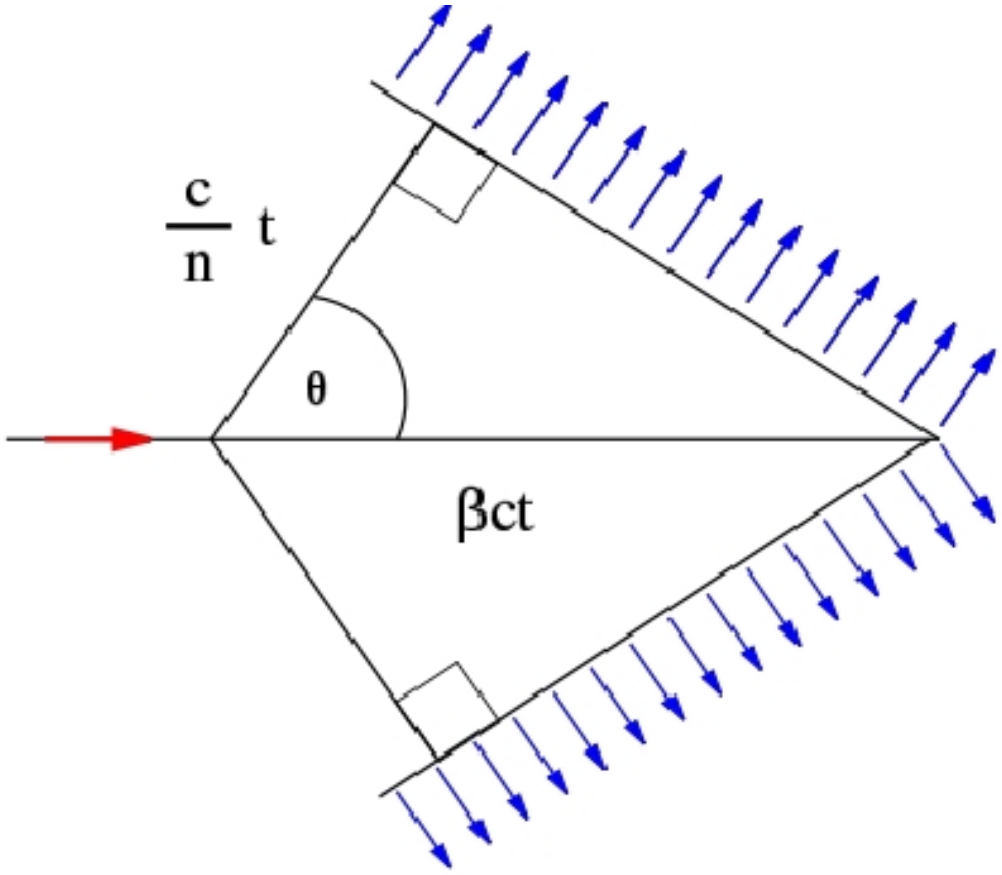

Figure 3.11: The geometry of the Cherenkov angle is given here. The incident particle particle path is given in red, and the Cherenkov light paths is given in blue.

the refractive index of the active medium, and β is the speed of the particle in units of the speed of light in the vacuum. A diagram of the derivation of the Cherenkov angle is given in Figure 3.11. Since the particle showers propagate with group velocities nearly equal to the speed of light in nearly all cases, the Cherenkov angle loses its β dependence and is left only depending on the refractive index. In the case of the quartz fibers, $n \sim \sqrt{2}$, which means that the Cherenkov angle for the particle showers in the quartz is essentially always 45°. This was exploited in the hadronic section of the ZDCs by tilting the tungsten and fiber by this angle. This maximizes the amount of light that the fibers can pick up from the particle showers to optimize the photomultiplier tube signal. There is limited space and the fibers are notoriously hard to bend, but at least one part of the Cherenkov cone can be coincident with the fibers in this ZDC design in the hadronic section.

Each section collects light via Hamamatzu R7525 phototubes [48] with a bi-alkali photocathode. The quantum efficiency for this model is specified as 10%. The voltage divider calibration in each phototube base can be optimized for linearity by setting proper high voltages, which are unique to each phototube. The gains are 100,000 in each channel. This was calculated already in time for the heavy ion run in 2010. Tables of each phototube's high voltage settings are given in Table 3.1 and Table 3.2.

Table 3.1: ZDC Minus PMT High Voltage Settings 2007

PMT Channel	PMT Serial Number	Voltage (V)
EM Section 1	CA3770	995
EM Section 2	CA3771	1125
EM Section 3	CA3772	1045
EM Section 4	CA3773	1075
EM Section 5	CA3774	1055
HAD Section 1	CA3764	1325
HAD Section 2	CA3765	1200
HAD Section 3	CA3766	1175
HAD Section 4	CA3767	1150

Table 3.2: ZDC Plus PMT High Voltage Settings 2007

PMT Channel	PMT Serial Number	Voltage (V)
EM Section 1	CA3777	1170
EM Section 2	CA3779	1250
EM Section 3	CA3780	1170
EM Section 4	CA3782	1150
EM Section 5	CA3784	1200
HAD Section 1	CA3786	1275
HAD Section 2	CA3787	1425
HAD Section 3	CA3788	1400
HAD Section 4	CA3789	1450

Chapter 4

Zero Degree Calorimeter Development

"There are only 18 channels to test. This shouldn't be too hard..."

4.1 CMS Zero Degree Calorimeter Construction

The CMS zero degree calorimeter construction begins with the fabrication of a copper box. The copper alloy being used is 110 copper alloy 14 which is an alloy of tellurium and copper [49]. A copper box electrically grounds the ZDC to the TAN, which is grounded to the LHC tunnel, it removes heat well, and it is the same copper the TAN is made of to prevent corrosion by the electrolysis of two dissimilar metals. The copper box is constructed from six rectangular plates that meet to form a rectangular prism. The interface of each edge of the plates is stair-stepped to constrain light to bounce at least three times before seeping through an edge upon assembly. This minimizes light leakage. There are also grooves cut into the copper to hold the tungsten in place. This is shown as an aluminum prototype for the hadronic section in Figure 4.1.

The next step in constructing the ZDC is to machine the tungsten absorbing medium.

Figure 4.1: An aluminum prototype is demonstrated here to show how the copper box is machined to hold the tungsten plates, which the plates, in turn, hold the optical fibers.

The tungsten type used in the absorbing medium is KULITE 1800. Each tungsten plate in the electromagnetic section has been premachined to 2 mm x 85 mm x 100 mm. Each tungsten plate in the hadronic section has already been premachined as a right parallelepiped slanted at the shortest dimension to 45° with the dimensions 10 mm x 85 mm x 151 mm. The hadronic section plates each had a fillet applied at the vertical edges by a mechanical belt sander in order to remove the possibility of the edges cutting the delicate optical fibers upon transporting the ZDC. The transport of the ZDC is not a one-time scenario, as it is removed from the TAN after key physics runs to let it radioactively cool down.

The fibers are a high-OH silica/silica type manufactured by Polymicro Technologies. The fibers have a core diameter of 0.6 mm, a clad diameter of 0.66 mm, a buffer diameter of 0.71 mm, and a numerical aperture of 0.22. [50]. Each fiber was initially cut to the length of 750 mm. The fibers have to fit in-between tungsten plates at the bottom of the ZDC assembly and be fed through fiber bundle tubes. The design of the ZDC is very conservative, so every possible space between the tungsten plates is filled with fiber. In all, 135 fibers fit in one layer between the tungsten plates in both sections. This implies that trimming is required to constrain the fibers flush with the bottom of the tungsten plates and the subjacent interface with the phototubes. This trimming was applied by bundling the fibers in a ZDC prototype, marking the trimming points on the fibers, and finally applying the cutting. This was essentially trivial for the hadronic section, because the channels situated along the z-direction are clones of one another. The electromagnetic section is more complicated because the channels segment the x-direction in 17 mm strips that fill the full 85 mm coverage. The hadronic section covers 85 mm in the x-direction also, but is not segmented. There was not enough space to situate the electromagnetic section phototubes within a line in the x-direction, so they were tightly packed in a "dice" arrangement resembling the facet of a six-sided die representing the number five. A picture of this assembly, called a readout box, can be viewed in Figure 4.2. This exhibits "square closest-packing" of the five phototubes in

the electromagnetic section. This made the routing of the fibers and trimming more difficult, but analogous to the hadronic section fabrication. The differences in the fiber routing between the electromagnetic and hadronic sections are given in Figure 4.3. The electromagnetic section fibers are routed to each channel by matching phototubes to x-segments that cause the fiber bundles to cross over each other the least. The hadronic section readout box is similar to this, but only contains one phototube per box. A picture of the fiber bundling in the hadronic section is also seen in Figure 4.1.

Since the tungsten radioactively heats up during irradiation by spectator matter, the phototubes should be sheilded from high energy and thermal radiation. This shielding is provided as a 30% boron-polyethylene and lead plate sandwich between the phototubes and the tungsten situated in the y-direction. There was not enough space to handle this shielding in the electromagnetic section as there was in the hadronic section. The location of the shielding is also labeled in in Figure 3.6.

4.2 CMS ZDC Test Beam Setup

There were test beam runs taken with the ZDCs in the summers of 2006 and 2007. To do this, the ZDCs were brought to the H2 test beam area at the Super Proton Synchotron (SPS) at CERN. A 400 GeV proton beam was bent onto a primary Be target that was capable of producing particle showers for selection by momentum and particle type. The two particles that were selected were the positron, for testing the electromagnetic section alone, and the negative pion for testing the total ZDC. The beam had an energy range selectable from 10 to 350 GeV. The test has served to provide an energy resolution measurement as well as mapping the nonlinear response of the ZDC for both electromagnetic and hadronic events.

The H2 area test beam was monitored several times upstream of the ZDC on its test platform. Various wire proportional chambers were used to map the x and y coordinates of the beam. In addition to this, there were Cherenkov gas threshold counters as well as

Figure 4.2: A photo of an EM Section ZDC readout box is shown here.

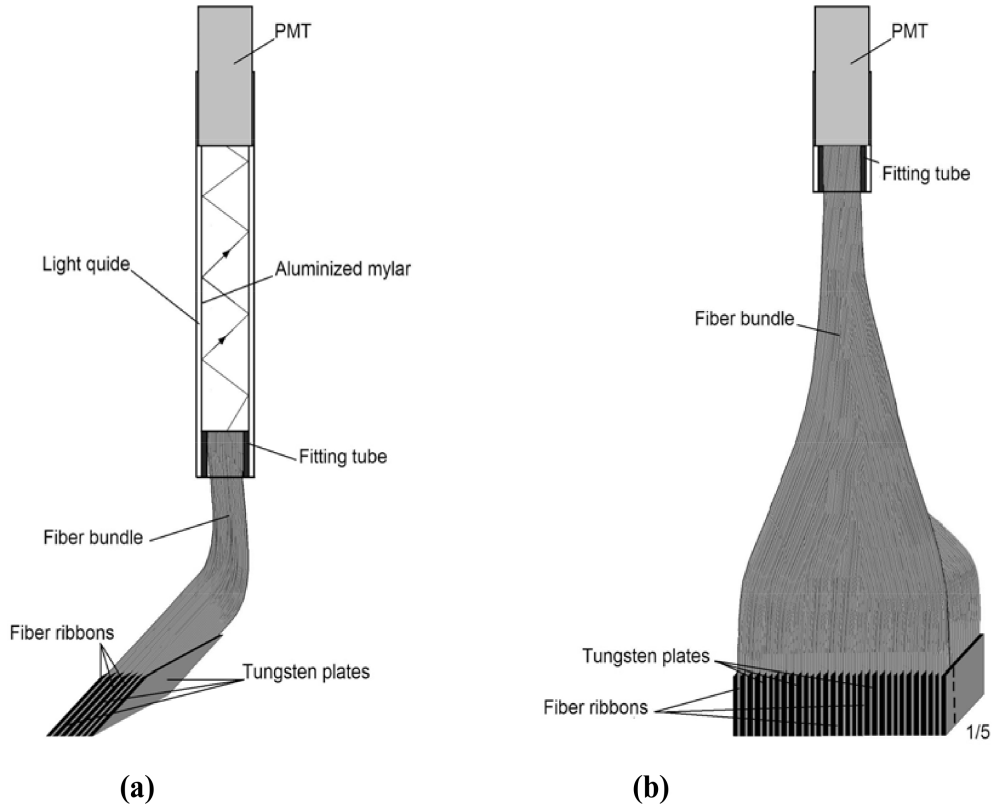

Figure 4.3: The hadronic section fiber arrangement is shown as "a," and the electromagnetic section is shown as "b." The light guide is no longer used in the hadronic section as the fiber runs the whole length to the phototube for each channel. In "b," the fiber bundles must cross at some point with a "dice" arrangement between channels.

scintillating counters to monitor both the luminosity and momentum of the beam. With this setup, the beam alignment, luminosity, and momentum is not only well known, but found to be very stable during the test beam efforts on the ZDC. A detailed schematic of the beam monitoring during the ZDC test beam setup is given in Figure 4.4 [45].

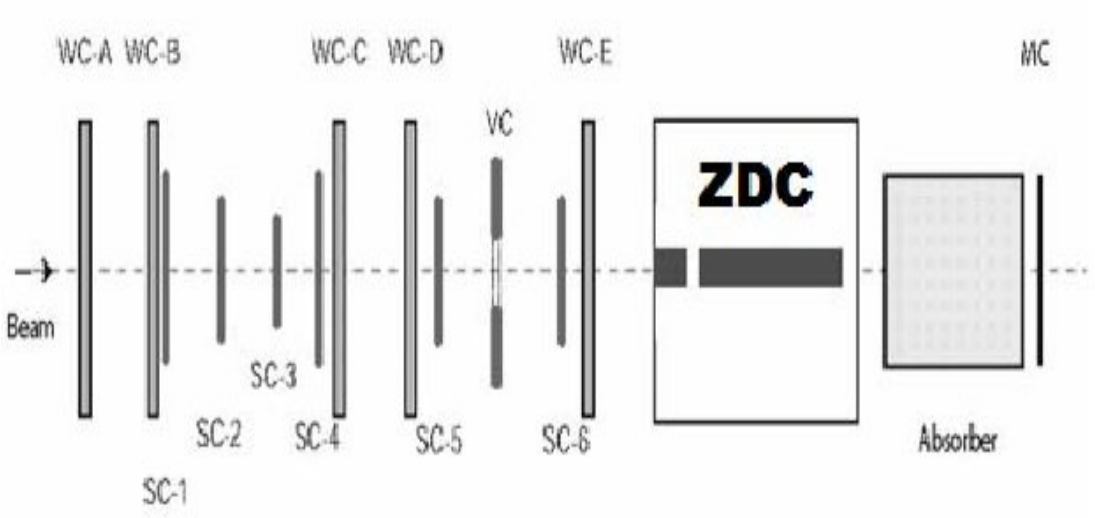

Figure 4.4: A schematic of the test beam setup is shown here [45]. "SC" stands for the location of scintillation counters, "WC" as wire chambers, and "VC" as Cherenkov counters.

In late July 2006, the first ZDC was assembled at the H2 test beam area at CERN. In this year, the 204-meter signal cables that are for use in the tunnel were used. First, the minus side EM section was tested. The EM section was placed on a manually operated hydraulic tray. This table had electronic control, which was rigged to the counting house where shift workers could operate it by remote control. The table had height adjustment for vertical alignment of the EM section into the beam as well as horizontal alignment. Hydraulic jacks lifted the table arrangement vertically while a motorized jackscrew could be twisted to control the horizontal position of the table.

High voltage cables provided by the H2 test beam personnel were attached to the high voltage connections on the readout box attached to the PMTs for high voltage supply. A temporary multi-channel high voltage power supply was also provided by the

H2 test beam personnel for use in energizing the PMTs. Voltages to supply each PMT were previously calibrated by Oleg Grachov and are the same voltages used when the ZDCs were installed in CMS.

Also, in late July 2006 during the last day of shifts, the minus side hadronic section was tested. It was fully assembled at the end of the test beam time that was allotted for the ZDCs, so the test beam data is not as numerous for the hadronic section in 2006 as it is for 2007. This test was strictly to examine if the hadronic section would be operational with essential event detecting components to show if the design was successful. This actually proved successful in a qualitative sense, but reliable quantitative data is limited to test beam from 2007. This is important because it offers a comparison to test beam data in between summers where the test beam setups had changed. The only relevant changes apply to ZDC connections and high voltage of the PMTs, not the testing the hardware itself with the beam.

There is no reference signal for the purposes of noise cancellation after installation of the ZDCs in the LHC tunnel. During the summer 2006 test beam, it was found that the resolution improvement was negligible when comparing the signal by itself to the addition of both reference and signal data. This was tested one-at-a-time in several ZDC channels during test beam efforts. The time to test this was 2006 when the signal cables were available, as they were not in the 2007 test. Since the reference cables would have cost $46,000 in additional funds for the ZDCs, it was not worth adding a reference cable to each ZDC channel by a cost-to-benefit consideration.

During late June and July 2007 test beam runs, both calorimeters were fully assembled and tested. There were some differences in the test setup. First, the signal cables were being pulled in the tunnel by qualified CERN personnel during ZDC test beam shifts, so they were unavailable for the tests. However, H2 personnel provided some coaxial cable for signal measurements. Now, although this cabling had a different impedance, capacitance and had different lengths than in 2006, it proved essential in testing the response of the calorimeters at low energies. The differences in the corre-

sponding data between two test beam setups from different years can be compared to analyze the true response of the calorimeter with the 204-meter signal cabling in the LHC tunnel. The main advantage in the 2007 data, however, is that the data are more numerous during 2007 test beam runs, and that both calorimeters were tested at the same time. So the less plentiful data in the 2006 test beam runs are useful for comparison in that the test beam setup resembles the actual CMS installation setup more than the 2007 test beam setup does. There are about 20,000 events per one beam momentum tested for each section, and this totals about 500,000 events for one section and 500,000 for the other [45].

4.3 Signal Response of ZDC

Testing the electronics for a uniform timing between channels is essential before any additional testing can continue. The timing is shown to be well uniform in all sections for both 2006 and 2007. The timing resolution is 25 nanoseconds, which is the same time resolution necessary to resolve single bunches at the LHC at maximum capacity. This timing resolution interval is defined as a timeslice, and a window of 250 nanoseconds containing the ZDC signal is called a timeslice plot when plotted as a histogram of ten timeslices. When the ZDC is installed into the CMS experiment the timeslices are synchronized to the LHC clock. All channels show peak response localized to timeslice 4, and the decay is consistent with the characteristic PMT behavior. An example of successful timing of combined ZDC channels is given in Figure 4.5 [51].

The linearity in the energy response of the ZDC is modeled first by fitting a response to test beam data at different energies. This starts with data both from the EM section alone and EM and Hadronic sections together from 2006. Although the data is less than the data acquired in 2007, the response is more accurate because we actually used the 204 meter signal cables that summer, where in 2007, they were not used in the tests.

The ZDC signals from pure electromagnetic events were found to be Gaussian distri-

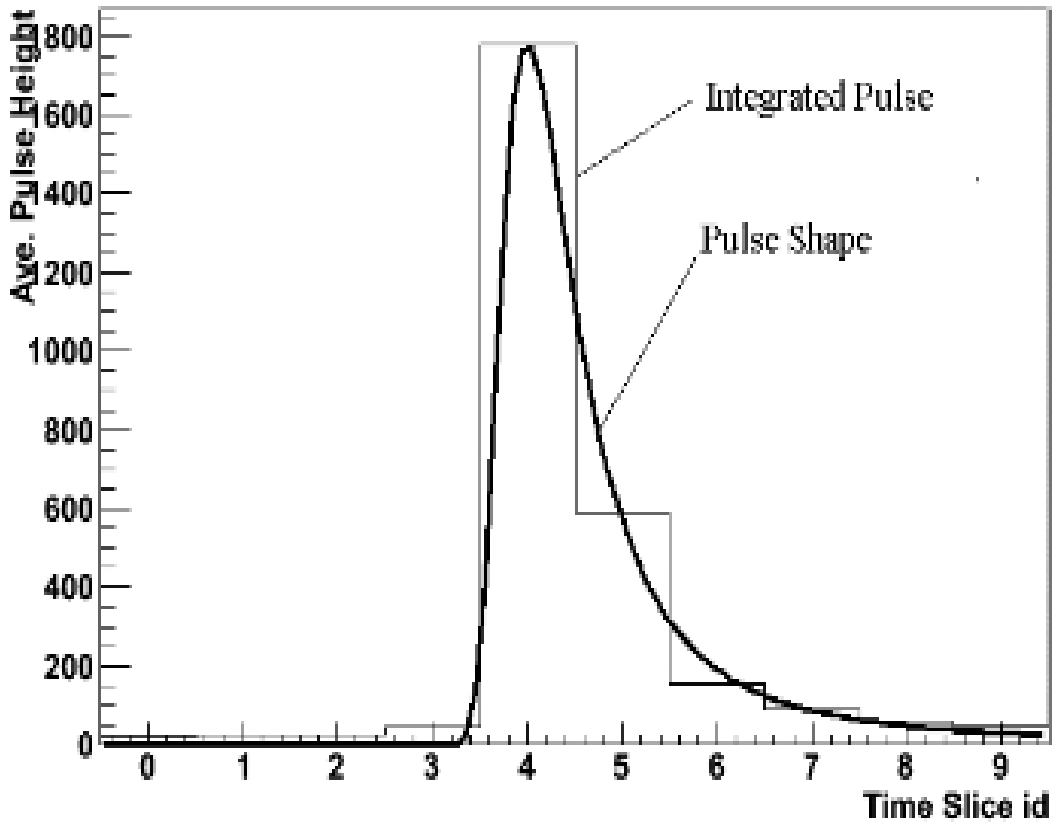

Figure 4.5: The timing profile of the combined ZDC channels is given here. Most of the PMT spike is localized to timeslice 4, and drops off with characteristic PMT response in each channel.

butions, and the signals from hadronic events were found to be Landau distributions [52, 53]. An example of a pure electromagnetic response is given in Figure 4.6. An example of the ZDC response to hadronic events is given in Figure 4.7. Because neutrons are hadrons, this means that spectator neutron peaks should be fit to Landau distributions from heavy ion running. This is performed in Chapter 6.

The energy resolution and the linearity of the EM section can be plotted from these fits. The combined test beam results for the EM section from 2006 and 2007 is documented to show the energy resolution in Figure 4.8 and Figure 4.9.

The energy resolution of the hadronic section can be plotted from these fits also. The combined test beam results for the hadronic section from 2006 and 2007 is documented

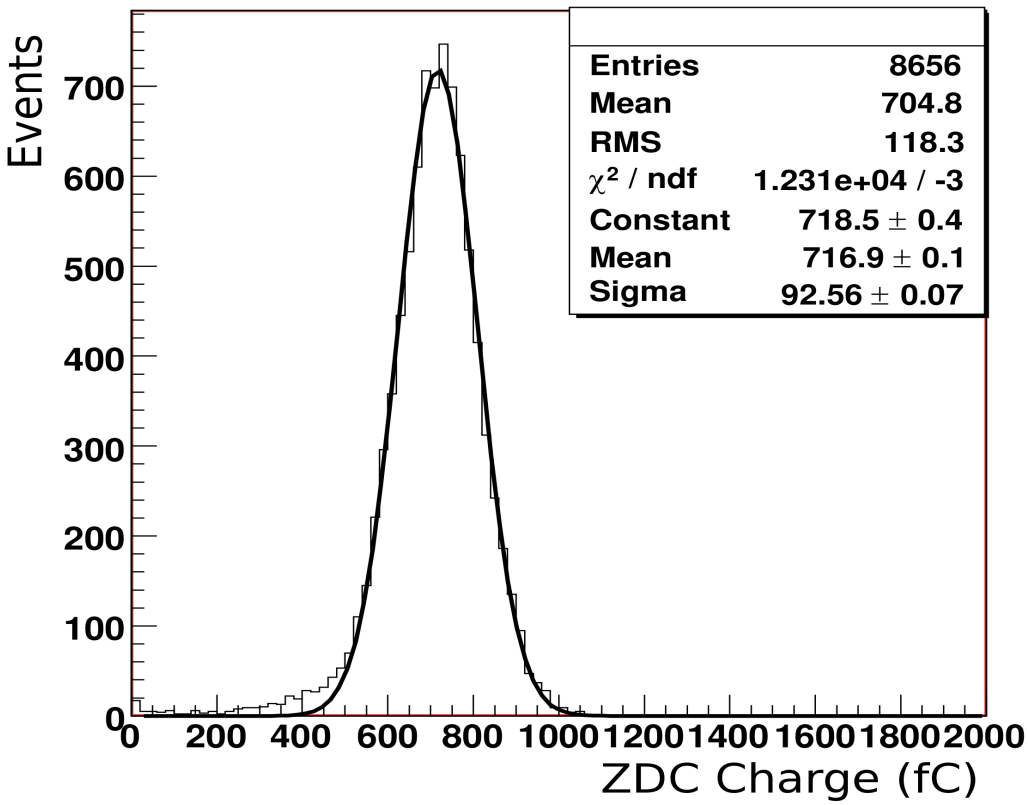

Figure 4.6: The EM section ZDC response of 50 GeV positrons is shown here. This is meant to illustrate the Gaussian response of the ZDC to pure electromagnetic events.

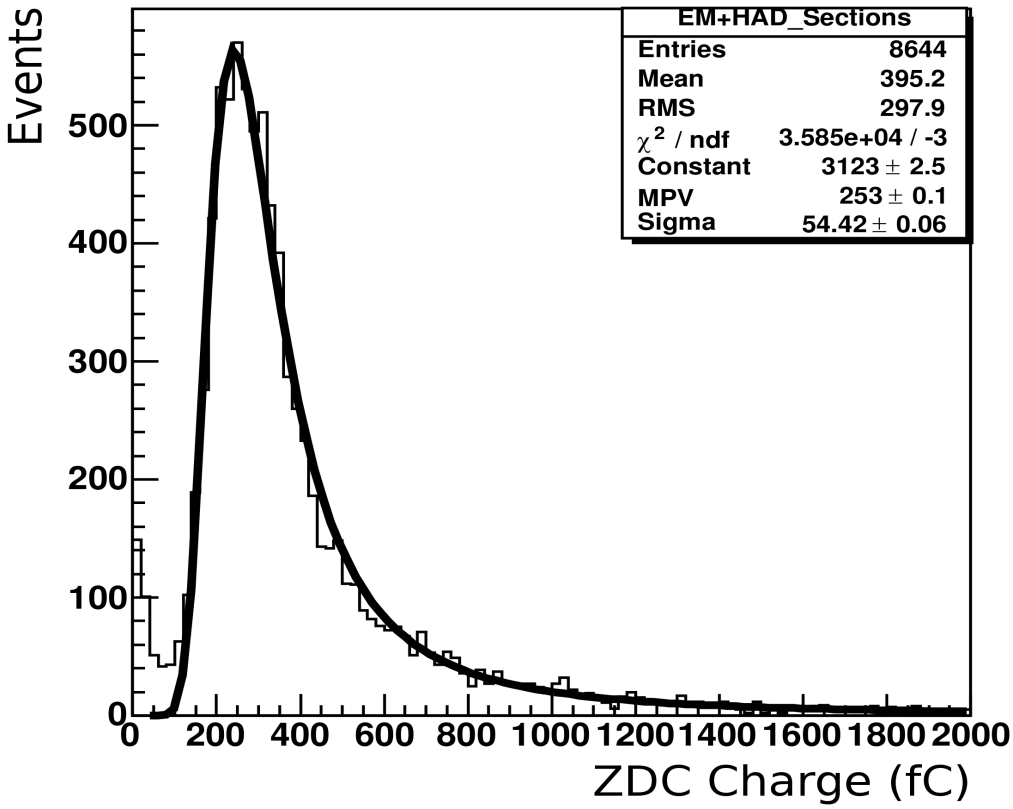

Figure 4.7: The ZDC combined EM and hadronic section response of 300 GeV negative pions is shown here. This is meant to illustrate the Landau response of the ZDC to hadronic events.

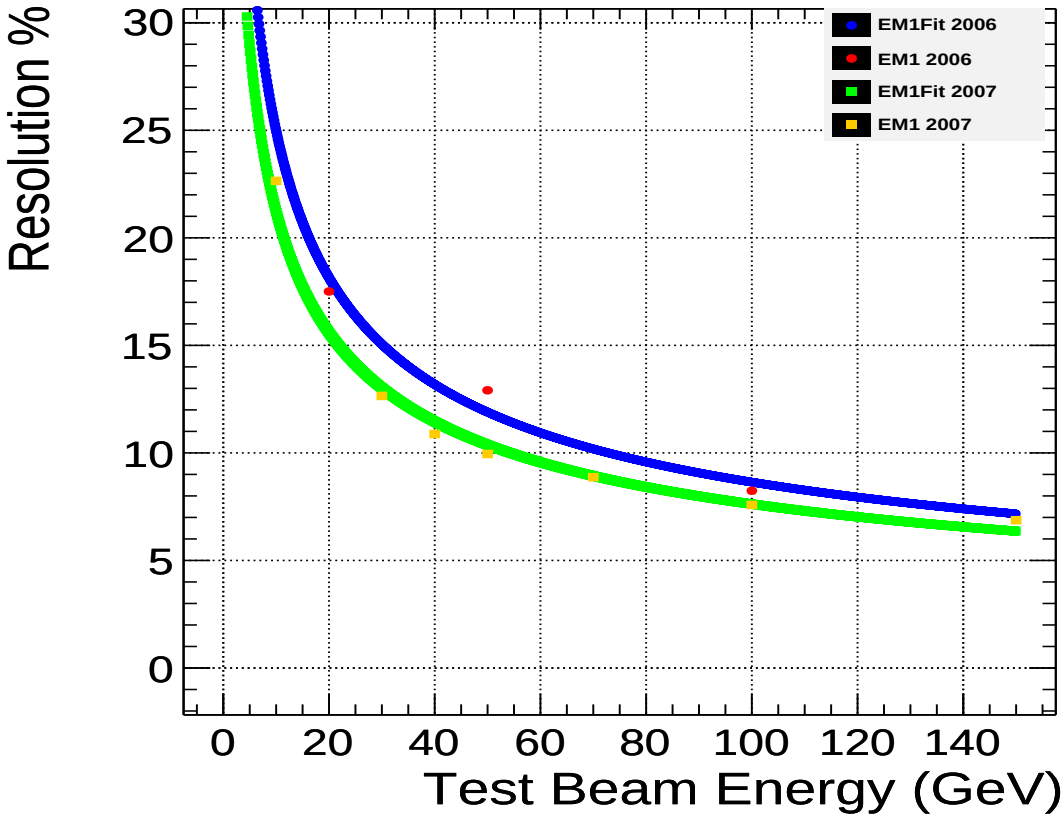

Figure 4.8: The ZDC minus electromagnetic signal response versus test beam energy is shown here for both test beam setups. The response is proportional to $1/\sqrt{energy}$.

to show the energy resolution in Figure 4.10 and Figure 4.11.

4.4 CMS ZDC Signal Path

The ZDC signal path is presented in Figures 4.12 and 4.13. This signal is a voltage sent by 204-meter length coaxial cable from the LHC tunnel to the CMS counting house where the phototube voltage is digitally processed. This cable routes the signal with a transmission speed of 0.75c. With a length of 204 meters and this transmission speed, it allows the ZDC signal to arrive in time for the Level 1 trigger at CMS. The voltage is sent to a charge integrating encoder (QIE) that converts the voltage from each ZDC channel into a charge. There is a characteristic impedance of the QIE of 50 Ohms, and

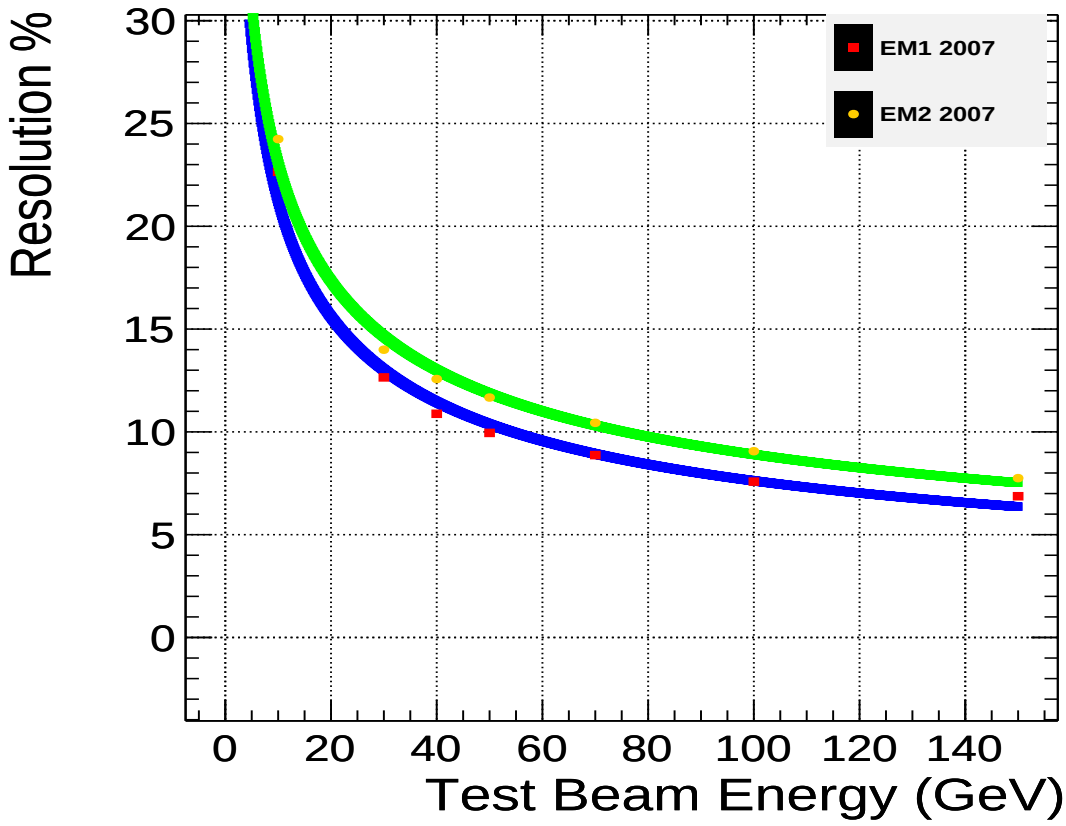

Figure 4.9: The ZDC plus and minus electromagnetic signal response versus test beam energy is shown here for the test beam setup in 2007, when both ZDCs were fully assembled. The response is proportional to $1/\sqrt{energy}$.

this effectively converts the voltage signal from each phototube into a current. This current is sent to one of four capacitors in each channel within the QIE for the analog calculation of an integral to obtain a charge measurement. The charge measurement is *linear* with the voltage, and is the standard step to digitizing phototube signals in calorimetry. The integration time is set as 25 nanoseconds, which is the minimum time between beam bunches at the LHC. This integration time interval is synchronized to the LHC clock. This current is integrated for 25 nanoseconds and converted into charge, but the processing time is between 75 and 100 nanoseconds, which accounts for the four capacitors. The capacitors are daisy-chained to handle the processing time. This

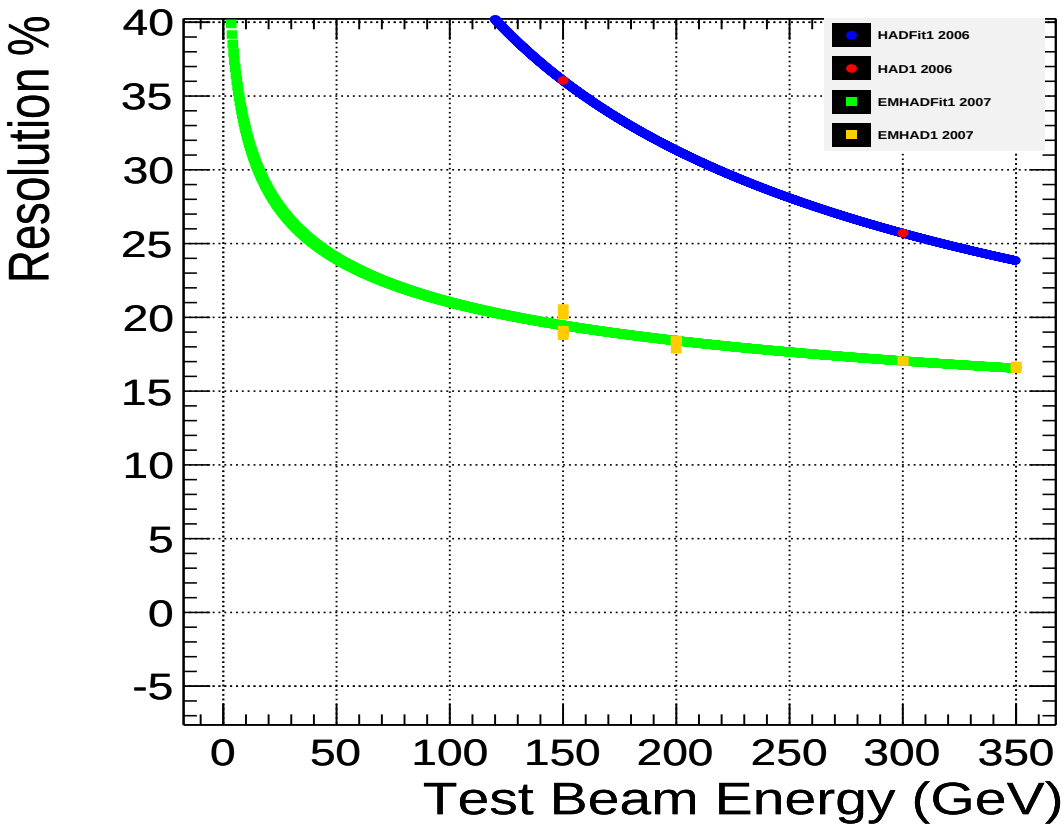

Figure 4.10: The ZDC minus hadronic signal response versus test beam energy is shown here for both test beam setups. The response deviates from linearity.

processing of the charge measurement of each channel converts the signal into a seven bit binary integer. This allows for a maximum number of analog-to-digital (ADC) bytes of 128, each of which has been calibrated by the QIE manufacturer to have an integrated charge associated with it. The scaling of the ADC bytes is logarithmic to maximize the dynamic range of the QIE response. Its range is piecewise linear and divided into quarters, each of which is roughly a power of ten higher charge than the previous quarter range. So, the first 32 ADC bytes run from roughly 1 to 10 femtocoulombs, the second set of 32 runs from about 10 to 100 femtocoulombs, the next 32 run from 100 to 1000 femtocoulombs, and the last set of 32 from 1000 to 10,000 femtocoulombs. The exact ADC channel to charge conversions are given in Table 4.1 and Table 4.2.

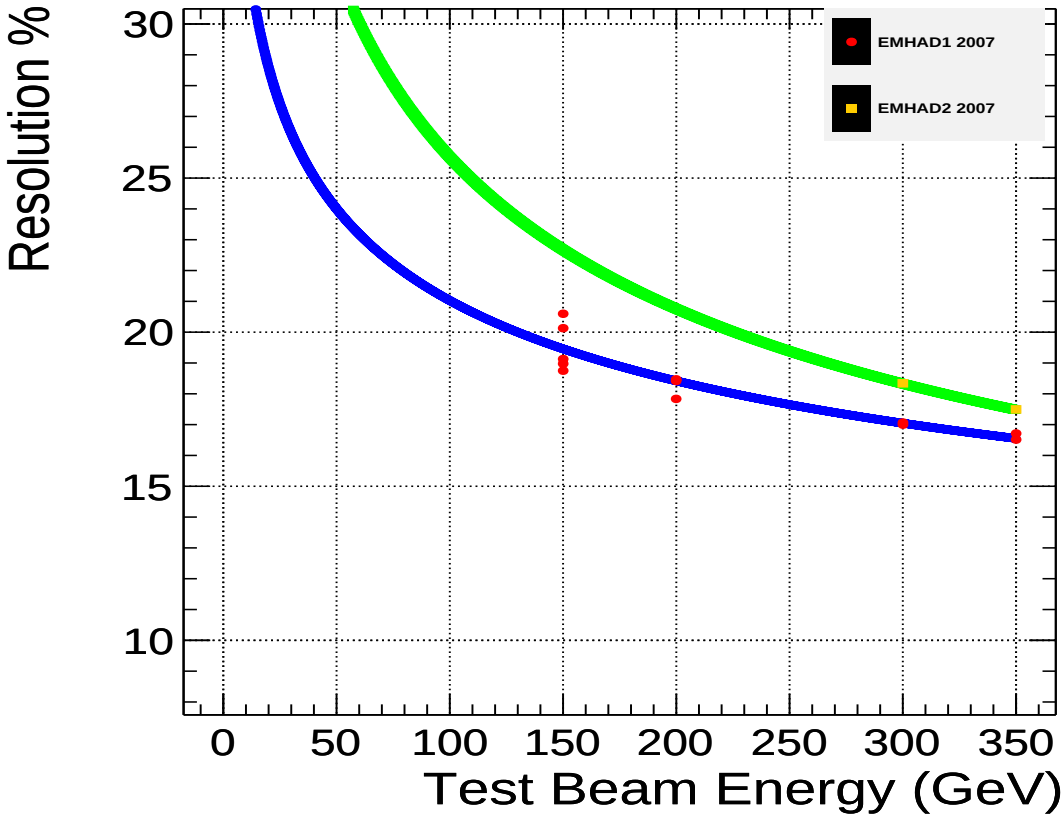

Figure 4.11: The ZDC plus and minus hadronic signal response versus test beam energy is shown here for the test beam setup in 2007, when both ZDCs were fully assembled. The response deviates from linearity.

It has been checked that a phototube signal less than 20 millivolts after the voltage drop through the cable does not saturate the time-integration of the signal into charge. Since the maximum possible charge the QIEs can handle before saturating is 10,000 femtocoulombs, the maximum input signal voltage can be calculated. This is given by $V = QZ/t$ where V is the maximum voltage, Q is the maximum charge of 10,000 femtocoulombs, Z is the characteristic impedance of the QIE of 50 Ohms, and t is the integration time of 25 nanoseconds. This yields a digital signal saturation voltage of 20 millivolts. This is well below the tube saturation voltage which was found to be ~ 135 millivolts, so only the digital saturation voltage applies here. So, any voltage signal

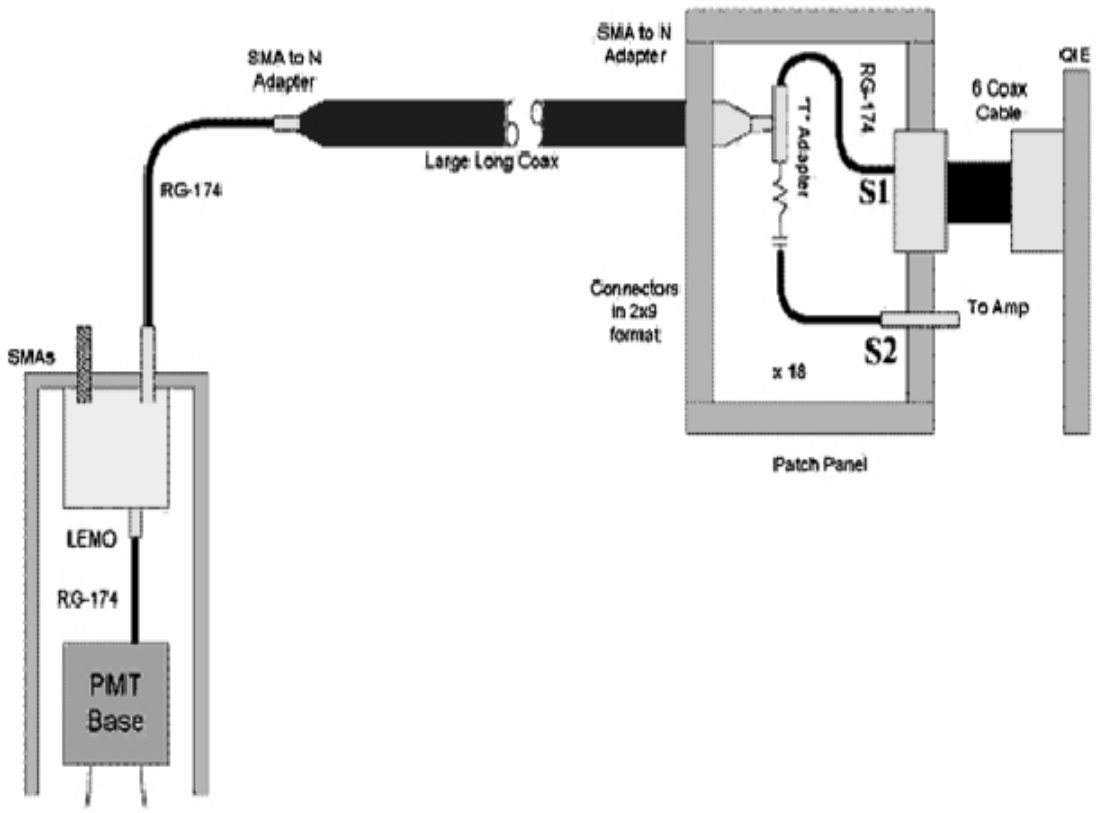

Figure 4.12: A schematic of the signal path from a readout box to the charge integrating encoder (QIE) is shown here. The QIE changes the analog signal from ZDC into a digital one suitable for physics analyses.

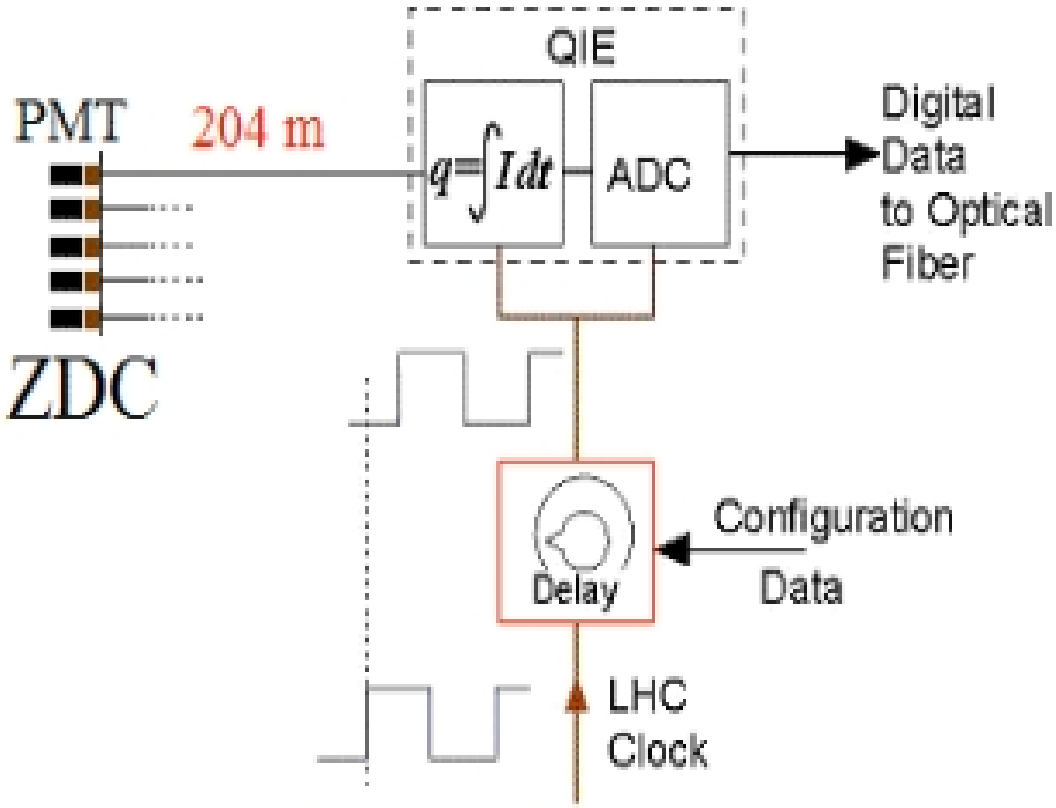

Figure 4.13: A schematic of the ZDC signal processing path is shown here.

above 20 millivolts is digitally clipped at the last ADC byte, which has consequences in the centrality analysis. Saturation was the largest difficulty in the heavy ion run in 2010 for the ZDC, and therefore for the centrality analysis, so it is emphasized here. Hardware and software calibrations are not allowed to change in the transition between proton-proton running to heavy ion running to make comparisons between the generated datasets independent of calibration. So, for the ZDCs, this means that signal from one neutron per bunch crossing, which can fill 75% of the dynamic range of the QIE alone, is increased dramatically. This can increase to essentially 60 times that per bunch crossing in heavy ion running. Fortunately, the phototube signal with this increase reaches about 120 millivolts, which is barely covered by the phototube headroom before the tube saturation of 135 millivolts.

The ZDC signal path is completed by the routing of the ADC counts to the HF detector server farm, where the rest of the networking of the ZDC data into storage servers is handled coincidentally with the HF effort. This means that the ZDC data storage effort "piggybacks" on the HF network. This step is shown in Figure 4.14 from the QIE to HTR box. HTR card is short for "HCAL Trigger Readout" card. This is where the digitized signal from the QIE is processed for use in the CMS framework. Timing, energy calibration, luminosity monitoring, data spooling, and trigger routing are all processed at the HTR card.

The timing is handled with dead-reckoning, and is directly programmed into the HTR firmware. The energy calibration is handled with lookup tables (LUTs), and converts the charge measurement into a corresponding energy in GeV. This was also directly loaded into the firmware. The ZDC signal path is connected to the luminosity monitor, but at the time of the analysis, is not used. The connection is present, but there is no luminosity monitoring framework for ZDC in this analysis. Each of these steps is symbolized in Figure 4.14.

The spooling of the data and the trigger path are each done by sending processed signal into an integrated module on the HTR card called the HTX. HTX is short for

"HCAL Trigger Extension." To spool the data, it is sent to a DCC card which is essentially a network hub for many designated HF channels in this application, one of which has been especially set aside for the ZDC. The DCC unit sends data to the surface of the CMS site where it is stored on various servers ready to be analyzed. This is also symbolized in Figure 4.14.

The HTX also sends data to a GCT module, or the "Global CMS Trigger." This trigger includes an algorithm trigger, and a technical trigger. For the ZDC, a one bit flag registers 1 when $\alpha(EMSum) + \beta(HADSum) \geq \gamma$, where $\alpha = 0$, $\beta = 1$, and $\gamma = 345GeV$, the quarter of the energy of a neutron in 2.76 TeV Pb beams. The bit is 0 otherwise. There are two bits for algorithm trigger and two bits for technical trigger. The two bits for each type flag the signals independently for each side of the ZDC. So, there are four trigger bits available for ZDC. Although they are available, the trigger bits for ZDC were not used, only the minimum bias trigger criteria was used in the analysis.

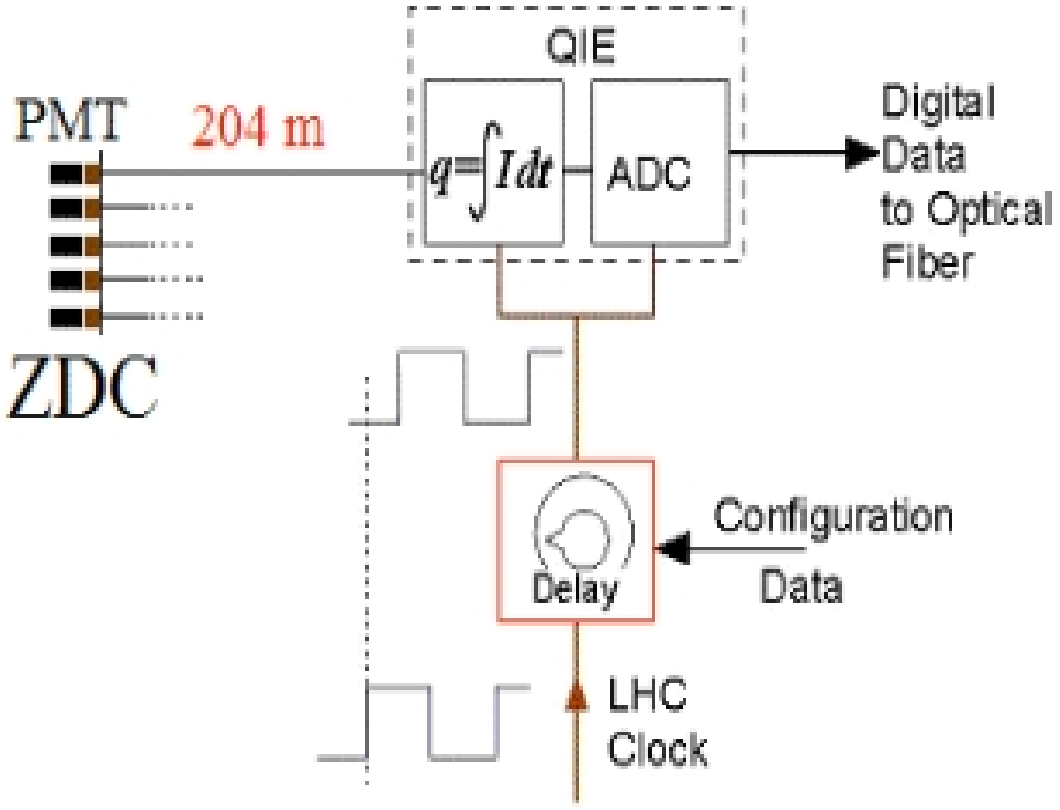

Figure 4.14: A flow chart of the complete control system of ZDC is shown here. The rack locations are given in beige boxes.

Table 4.1: QIE ADC Channels 0 - 63 Charge Conversions

ADC Channel	Charge (fC)	ADC Channel	Charge (fC)
0	-0.5	32	59.5
1	0.5	33	64.5
2	1.5	34	69.5
3	2.5	35	74.5
4	3.5	36	79.5
5	4.5	37	84.5
6	5.5	38	89.5
7	6.5	39	94.5
8	7.5	40	99.5
9	8.5	41	104.5
10	9.5	42	109.5
11	10.5	43	114.5
12	11.5	44	119.5
13	12.5	45	124.5
14	13.5	46	129.5
15	15.0	47	137.0
16	17.0	48	147.0
17	19.0	49	157.0
18	21.0	50	167.0
19	23.0	51	177.0
20	25.0	52	187.0
21	27.0	53	197.0
22	29.5	54	209.5
23	32.5	55	224.5
24	35.5	56	239.5
25	38.5	57	254.5
26	42.0	58	272.0
27	46.0	59	292.0
28	50.0	60	312.0
29	54.5	61	334.5
30	59.5	62	359.5
31	64.5	63	384.5

Table 4.2: QIE ADC Channels 64 - 127 Charge Conversions

ADC Channel	Charge (fC)	ADC Channel	Charge (fC)
64	359.5	96	1859.5
65	384.5	97	1984.5
66	409.5	98	2109.5
67	434.5	99	2234.5
68	459.5	100	2359.5
69	484.5	101	2484.5
70	509.5	102	2609.5
71	534.5	103	2734.5
72	559.5	104	2859.5
73	584.5	105	2984.5
74	609.5	106	3109.5
75	634.5	107	3234.5
76	659.5	108	3359.5
77	684.5	109	3484.5
78	709.5	110	3609.5
79	747.0	111	3797.0
80	797.0	112	4047.0
81	847.0	113	4297.0
82	897.0	114	4547.0
83	947.0	115	4797.0
84	997.0	116	5047.0
85	1047.0	117	5297.0
86	1109.5	118	5609.5
87	1184.5	119	5984.5
88	1259.5	120	6359.5
89	1334.5	121	6734.5
90	1422.0	122	7172.0
91	1522.0	123	7672.0
92	1622.0	124	8172.0
93	1734.5	125	8734.5
94	1859.5	126	9359.5
95	1984.5	127	9984.5

Chapter 5

Centrality Analysis

"They are not called banana plots because of their shape. It is because they drive their analyst 'bananas'..."

The analysis is based on the correlation between the pixel multiplicity and the ZDC energy. Originally a two dimensional analysis was tried but this found to be numerically unstable. The one dimensional linearization method was much more robust.

5.1 The Two-Dimensional "Pivot-Point" Method

Several experiments have sort to measure centrality by combining information from zero degree calorimeters and detectors near central rapidity [31, 32, 54]. Figure 5.1 shows the correlation between the energy in the two ZDCs and the multiplicity of pixel hits for minimum bias events. The trigger and event selection for this dataset have already been described in Section 2.3. The number of pixels is proportional to the energy carried by particles with $|\eta| < 2.4$. In this analysis, the full three-layer pixel detector barrel is used.

The ZDC signal was simply the sum of all the ZDC channels using the pp calibration. This means that the ZDC signal contained some pickup noise and was saturated for some events with a large number of neutrons. Working with this therefore compressed ZDC

data was not a waste of time however since it allowed a fast exploration of the centrality method used in previous generation experiments.

In previous experiments, plots such as Figure 5.1 were known as "banana plots." This nomenclature will be used from now on. In Figure 5.1, the y-axis is given as energy in units of GeV divided by a maximum of 85,000 GeV, and the x-axis is given as the number of pixels that registered a hit in a given event divided by a maximum of 36,000 pixels. Several features of Figure 5.1 are worth noting. First, for events that produced almost the maximum number of pixels the nucleus essentially explodes and their are no spectator neutrons at zero degrees. For scaled pixel values between 0.2 and 1, there is an anti-correlation between ZDC energy and pixel multiplicity. This comes about because of conservation of energy within the collision. If more energy is used to produce a greater multiplicity less is available to go forward. Peripheral collisions, with scaled multiplicity less than 0.1 reveal the physics of nuclear breakup. Such collisions does not contain enough energy to evaporate the nucleus and only break it into smaller nuclei. Such nuclei include stable nuclear states like doubly-magic Helium-4, doubly-magic Oxygen-16, doubly-magic Calcium-40, and many smaller, less stable leftovers like deuterons. Because all of these pieces are charged, they will not make it to the ZDC, because the beam-crossing dipole magnets will bend them away. Such "multifragmentation" events are characterized by large event by event fluctuations [55].

The average response of ZDC in this banana plot is called the profile histogram. This histogram is shown by the black plots superimposed on Figure 5.1. The main goal of making a centrality measurement is to create event cuts which scale with the profile and the nuclear collision cross section. The centrality method must divide the cross section equally into a certain number of centrality bins. The heavy ion group has chosen 40 centrality bins. Cuts must be made to follow the profile while dividing the number of events in the banana plot by 40. Each centrality bin will then correspond to a region of the banana plot between two cut lines. A strategy must be developed to divide the banana plot into 40 distinct sectors that each contain 2.5% of the events.

These sectors must not overlap since any event must lie in one and only one centrality bin.

Previous experiments used linear inequalities between ZDC signals and other detectors to make these cuts. To accomplish this at CMS, the banana plot was divided into the four distinct regions shown in Figure 5.2. Region 1 corresponds to central collisions where the ZDC energy and pixel multiplicity are anti-correlated. Here, it is relatively simple to make cuts that are perpendicular to the profile histogram.

Region 4 corresponds to very peripheral events where there are very few tracks in the pixels. Because there is so little information in pixels for the peripheral collisions we make cuts that only depend only on the ZDC. Regions 2 and 3 correspond to semi-central events where the relationship between ZDC energy and pixel multiplicity is not monotonic. This is the most difficult region to develop cuts. A vertical line at scaled pixel multiplicity of 0.1 separates regions 1 and 2.

Region 2 is a place on the profile that begins with a vertical cut. Since the derivative of the profile of the banana plot changes sign here, cuts must be developed to deal with cuts that don't yield symmetry in the number of events on either side of the profile histogram. This is because only linear inequality cuts are used throughout all regions of the banana plot. This is made into a distinct region because it is the most difficult region to make cuts, and using the region 1 method is not possible here.

Region 3 corresponds to a place on the banana plot where geometric difficulties end from region 2. This region follows the region 1 method as long as possible. Region 4 is the region of peripheral collisions. Here, minimal amounts of pixel multiplicity remain, and the ZDC dominates the banana plot. Because there is so little information in pixels for the peripheral collisions, cuts that only depend on ZDC can be made in region 4.

In Figure 5.3, the region 1 cutting method is illustrated. Here, a fit to the profile is made, and from its derivative with respect to pixel multiplicity, a slope is attainable. In order to take advantage of the symmetry in the number of events on either side of the profile histogram, lines are drawn perpendicular to the profile to separate events

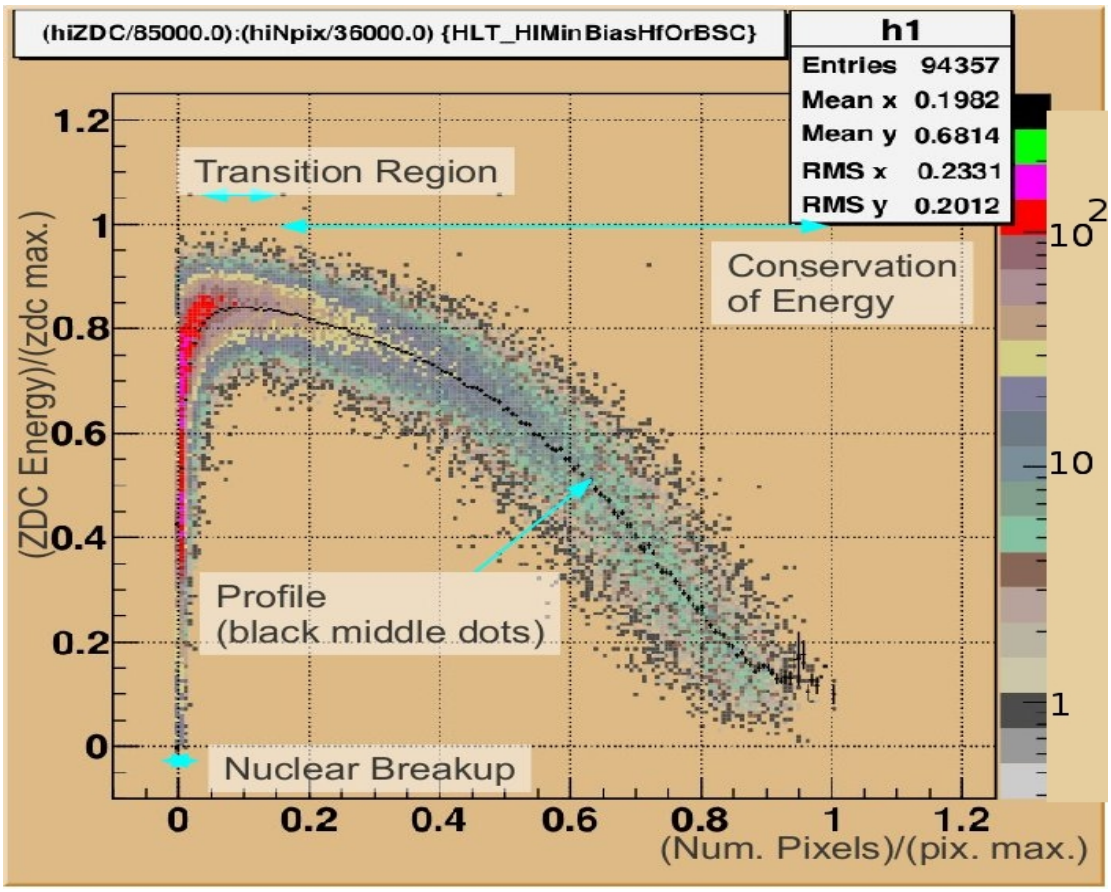

Figure 5.1: A banana plot is shown here. The physics significance in each relevant region is labeled. Each non-black dot represents one or more events with a given value in ZDC and pixel units. The black dots represent the average ZDC values for a given pixel value. This substantiates a profile histogram.

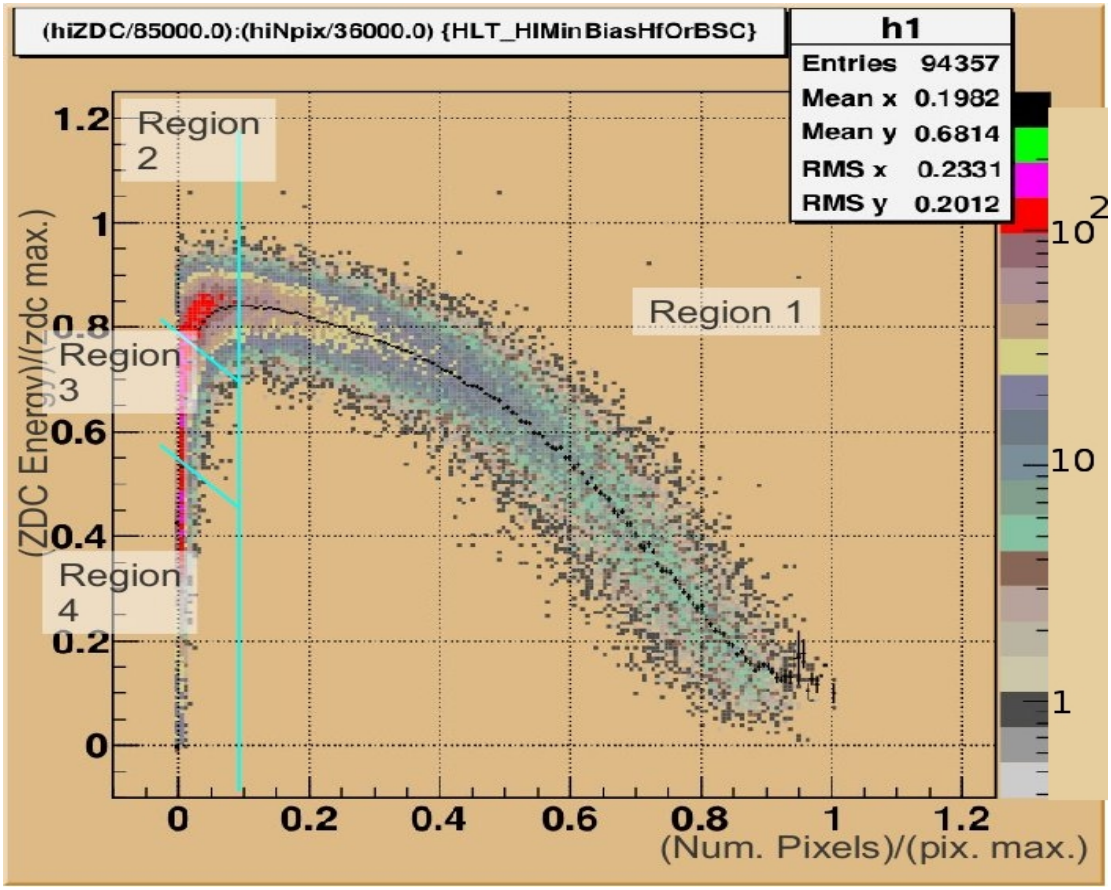

Figure 5.2: A division of the banana plot into four pertinent regions for methodically deriving centrality is shown here.

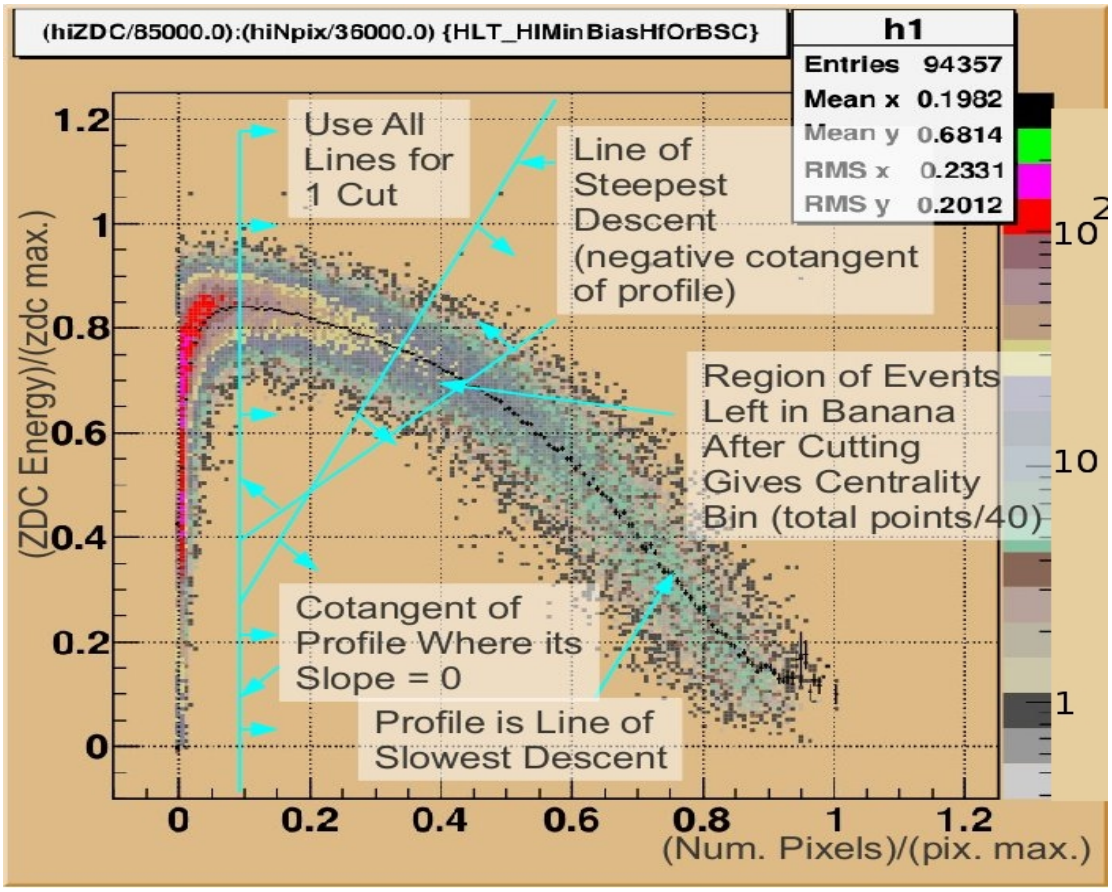

Figure 5.3: A banana plot isolating the first region's method for the measurement of centrality is shown here. The cuts are equivalent to cotangents of the profile histogram superposed over the banana plot.

in different centrality classes. Therefore, the number of events leftover in the banana plot corresponding to a centrality bin is bounded by perpendicular lines on the banana plot. Since the derivative of the fit to the profile is known, the negative reciprocal is also known to obtain the slope of such lines. Additionally, the ZDC-intercept of these lines is also known, because the profile has already be fit to a ZDC value for every pixel multiplicity value. Finally, a linear inequality can be constructed in terms of ZDC and pixel multiplicity in the form of a negative cotangent to the banana plot profile in order to cut events.

The first cut is constructed from a singular linear inequality which cuts all events away from the right end of the banana plot profile. This leads to the events that correspond to the first centrality bin. There is also a vertical cut on everything to the left of pixel multiplicity divided by its maximum value at 0.1058. This is a place where the profile derivative is zero. This vertical cut is common to all subsequent cuts in region 1, and necessarily, its the most simple way to ensure that linear inequalities to not cut on events on the peripheral collision side of the banana plot.

The next cuts in region 1 require two linear inequalities in addition to the common vertical cut already described. Beginning with the first linear inequality, the inequality is reversed to cut on events opposite the previous centrality bin. This determines the upper pixel multiplicity bound of the next cut. The lower pixel multiplicity bound of events corresponds to a linear inequality where the inequality is opposite to that of the upper bound. This lower pixel multiplicity bound is chosen such that the number of events sandwiched in between both linear inequalities is the same number as in the previous events for the previous centrality bin. This process repeats until centrality bin 47.5% is achieved. It so happens that in this measurement, the vertical cut common to all in region 1 is a necessary cut for the last centrality bin in region 1. Curiously, this almost completely divides the nuclear collision cross section in half. The fact that this happens, however, is not physically necessary, just surprising.

In region 2, the radius of curvature of the banana plot profile drops significantly.

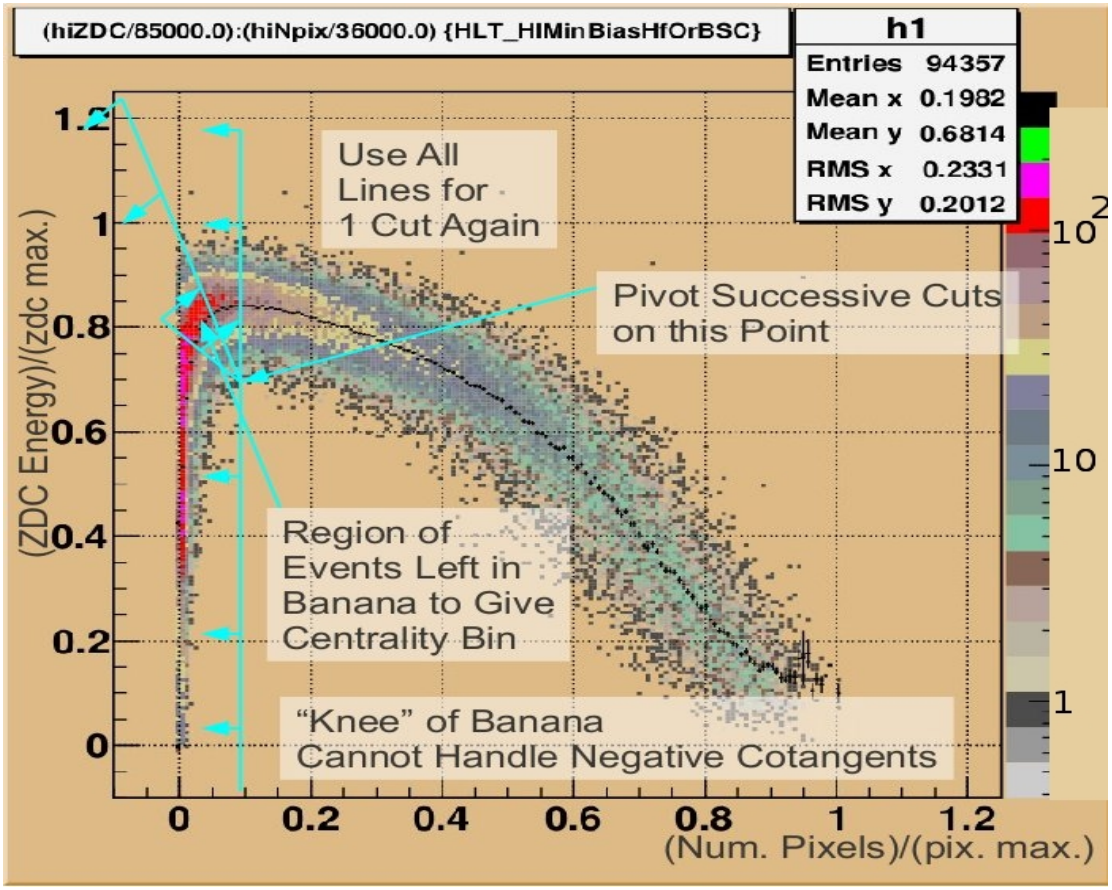

Figure 5.4: A banana plot isolating the second region's method for the measurement of centrality is shown here.

This means that linear inequality cuts that are bounded by cotangents to the profile can intersect in the banana plot where the density of events is nonzero. Although there was finite radius of curvature in region 1, any intersection of the linear inequality bounds happened in regions of the banana plot where the density of events was zero. Intersecting cuts within the banana plot must be avoided since any point can only belong to one centrality class. Since using negative cotangents to the profile will cause problems in region 2, a new method is needed.

In Figure 5.4, this new cutting method is illustrated. A pivot point is used to make successive cuts in this region. To acquire this pivot point, a plot of arbitrary negative cotangents to the profile is created first. Such a plot is given in Figure 5.5. Here, the behavior of the intersecting negative cotangents is studied. It is too naive to expect a common intersection for all negative cotangents, but a place where the density of intersections is greatest *is* something worth looking for. The locus of all intersections of the negative cotangents of the profile with themselves is called the evolute of the profile. The place where the density of intersections is greatest is called the cusp of the evolute. It is this cusp that is the most logical place to make a common pivot point for successive cuts on the banana plot. This is because if a common pivot cannot be found for all negative cotangents, the next best thing is to find a place where they at least come the *closest* to doing so. It turns out that there is a place where this happens very clearly, and curiously, it corresponds to a point intersecting the common vertical cut in region 1. With this amount of convenience in the analysis, it can be quite stunning that this vertical cut is so useful. However, there is one inconvenience that is unavoidable. Since the ZDC has such large statistical fluctuations in region 2, a pivot point is not attainable where it will lie in the banana plot where the density of events is zero. This is unfortunate, but it is kept to a minimum here, as the density of events is at least sparce.

Since all the points necessary to create linear inequality cuts are defined, the method can be described. In similar fashion to region 1 a successive method results. Starting

with the vertical cut selecting all events to the left of the banana plot this time, the slope of the line passing through the pivot point is adjusted such that events toward the vertical cut are selected to contain the same number as they did in each centrality bin in region 1. So, the vertical cotangent and the new pivot point line bound the first centrality measurement in region 2. For successive cuts, the process continues using the previous centrality bin upper bound as a lower bound with opposite inequality, and new pivot point line slopes are adjusted to contain the number of events as in the previous centrality bin. These two line therefore sandwich again the events that correspond to each centrality bin, as was similar to the method in region 1.

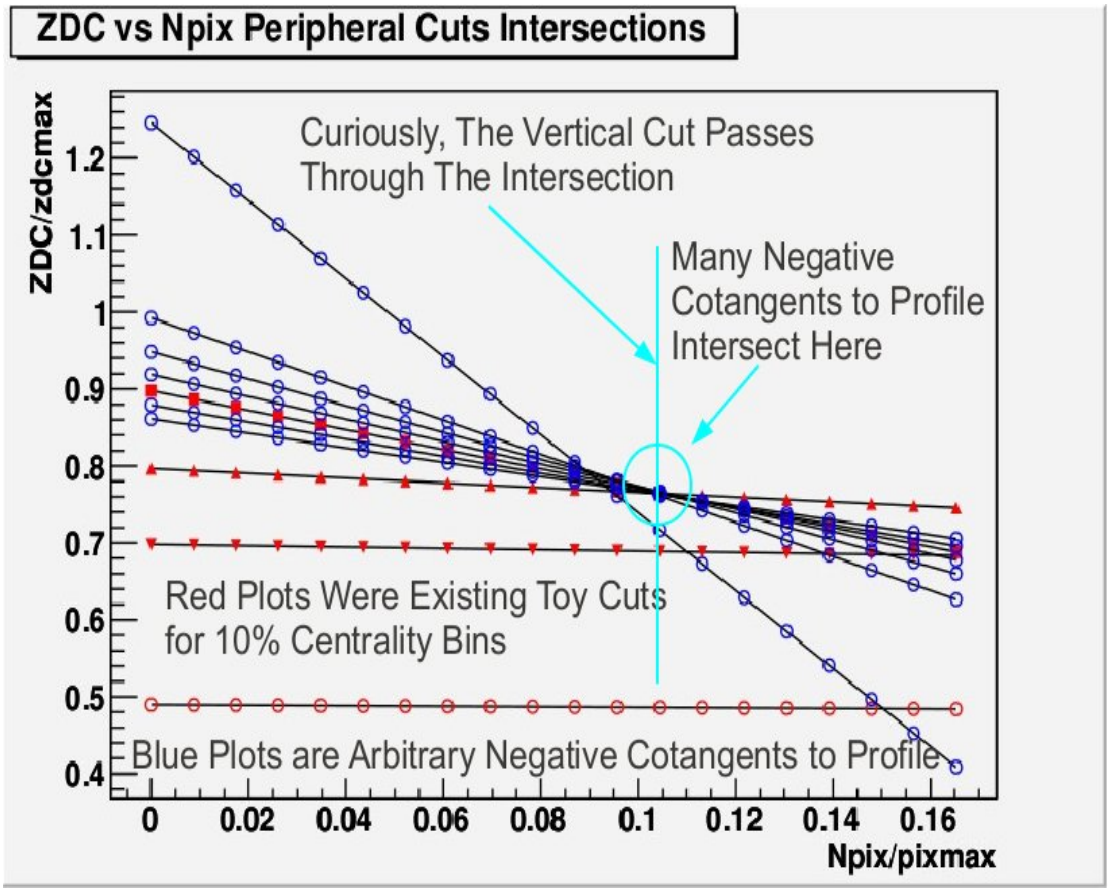

Figure 5.5: The method used to select a pivot point for cuts in the transition region of heavy-ion collisions is shown here.

In region 3, the process from region 1 is continued as shown is Figure 5.2. This

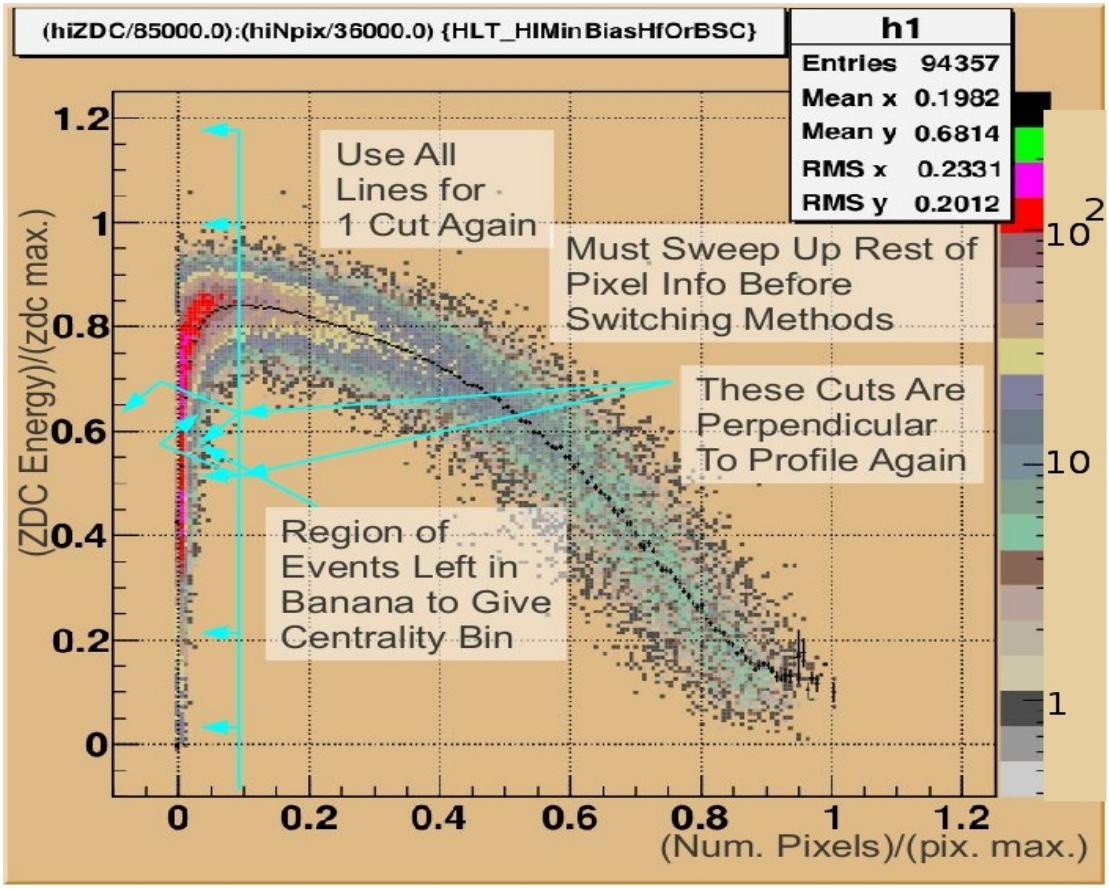

Figure 5.6: A banana plot isolating the third region's method for the measurement of centrality is shown here. This method is the same as in the first region.

is shown in Figure 5.6. It should be noted that the place to define the beginning of region 3 is a place where the slope of the negative cotangent best matches the slope of the line passing through the pivot point in region 2. This is, of course, still under the constraint of keeping the nuclear collision cross section equal between different centrality bins which overrides all other importance. The slope matching phenomenon is a way to make the transition between the two regions as smooth as possible, and this has the effect of preserving the most symmetry of events along the path of the profile. Region 3 begins then at a centrality of 67.5%.

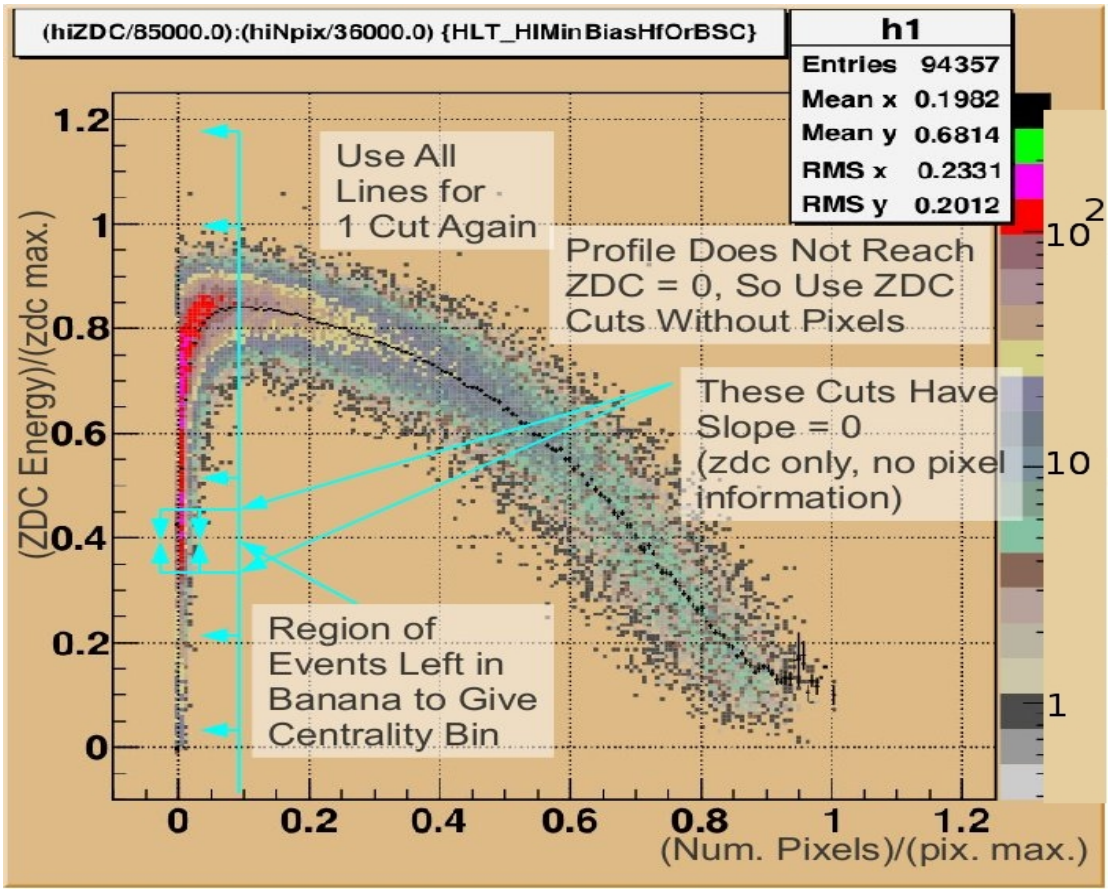

Figure 5.7: A banana plot isolating the fourth region's method for the measurement of centrality is shown here. These are essentially cuts only dependent on ZDC energy.

In region 4, a completely new method begins as drawn in Figure 5.7. This is because the profile of the banana plot defines the average of all ZDC events. So, this naturally

cannot go to zero as the ZDC information spans its full range for peripheral collisions. Therefore, if the region 3 method continues, then it will not be possible to find centrality for the peripheral cases because it will not be possible to cut on ZDC divided by ZDC maximum values of less than 0.4, where the profile intersects zero pixel multiplicity. The most logical place to begin a new method is therefore at the place before the profile intercepts the ZDC axis.

This happens right before the region 3 method allows for a centrality measurement up to 85%. So, for 85% onward, the analysis finishes with region 4. Since there is so little pixel multiplicity here, it is pertinent to make ZDC only cuts. This is actually quite simple, and can use the sandwiching method that has been used in the other three regions and adapt it for ZDC only cuts. The only difference worth noting after this fact is that the trigger efficiency is 99%. So, physically, there were actually more events in the data than were triggered upon. This has been taken into account carefully throughout the analysis by considering not the events in the data sample, but by that number divided by 99%. Then, the number of events in each cut then divides the number of events independent of the trigger by 40. Since there are naturally less events in the sample than this because of the trigger efficiency, there is a remainder left over at the end. Fortunately, in keeping the scheme set up in the previous centrality analysis by the CMS heavy ion group, the remainder of the events trivially go into the last centrality bin. This was correctly taken into account for the last events in region 4.

After this very convoluted and arbitrary method is completed for all four sections, Figure 5.8 shows the result. The number of events corresponding to each centrality bin from the dataset is given in Figure 5.9.

A Monte Carlo does not exist for ZDC to return the average number of participants in the events corresponding to each centrality bin. There was, however, an AMPT Monte Carlo simulation [56] performed on HF energy data. Therefore, a sanity check was performed by reweighting the HF distributions given by the monte carlo corresponding to each centrality bin. This is done by selecting the events from the banana plot in

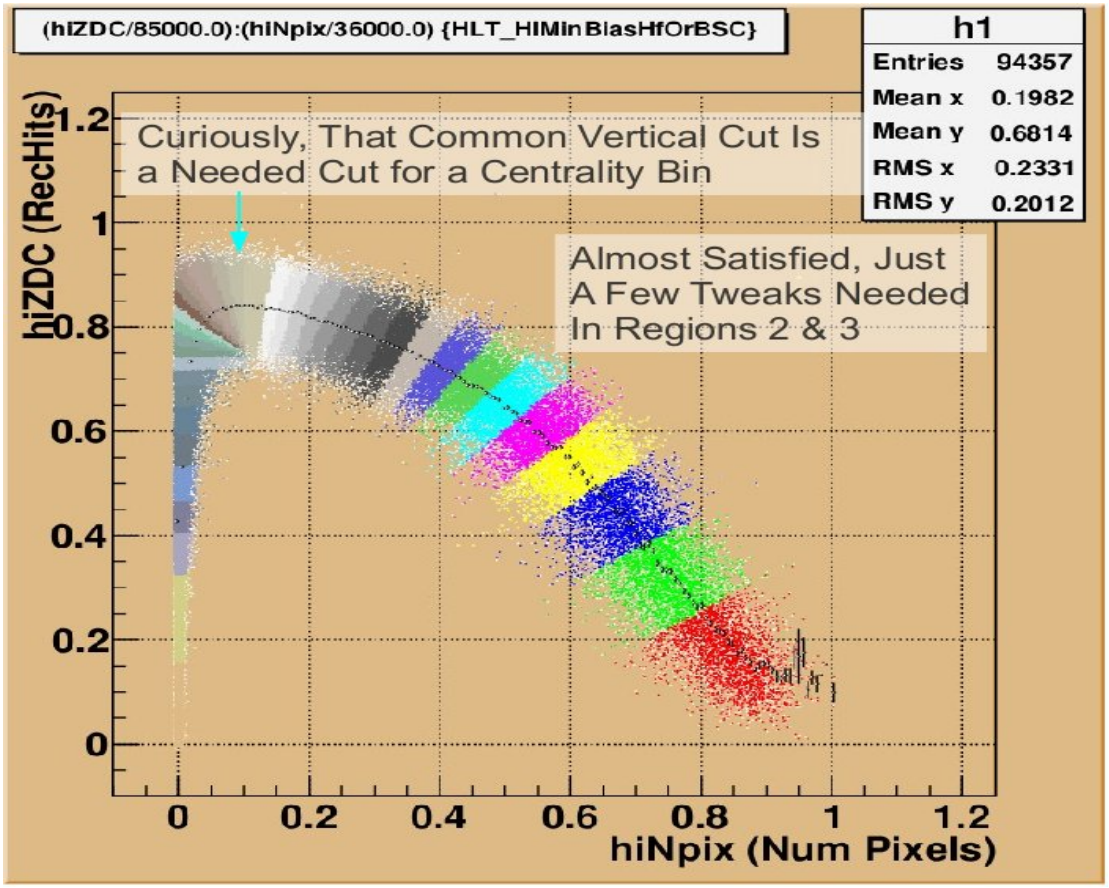

Figure 5.8: A banana plot with 40 color-separated cuts is shown here derived from satisfactory equal nuclear collision cross-section requirements for dividing events. The most peripheral bin gets the remainder of the nuclear cross section to take the trigger efficiency of 99% into account.

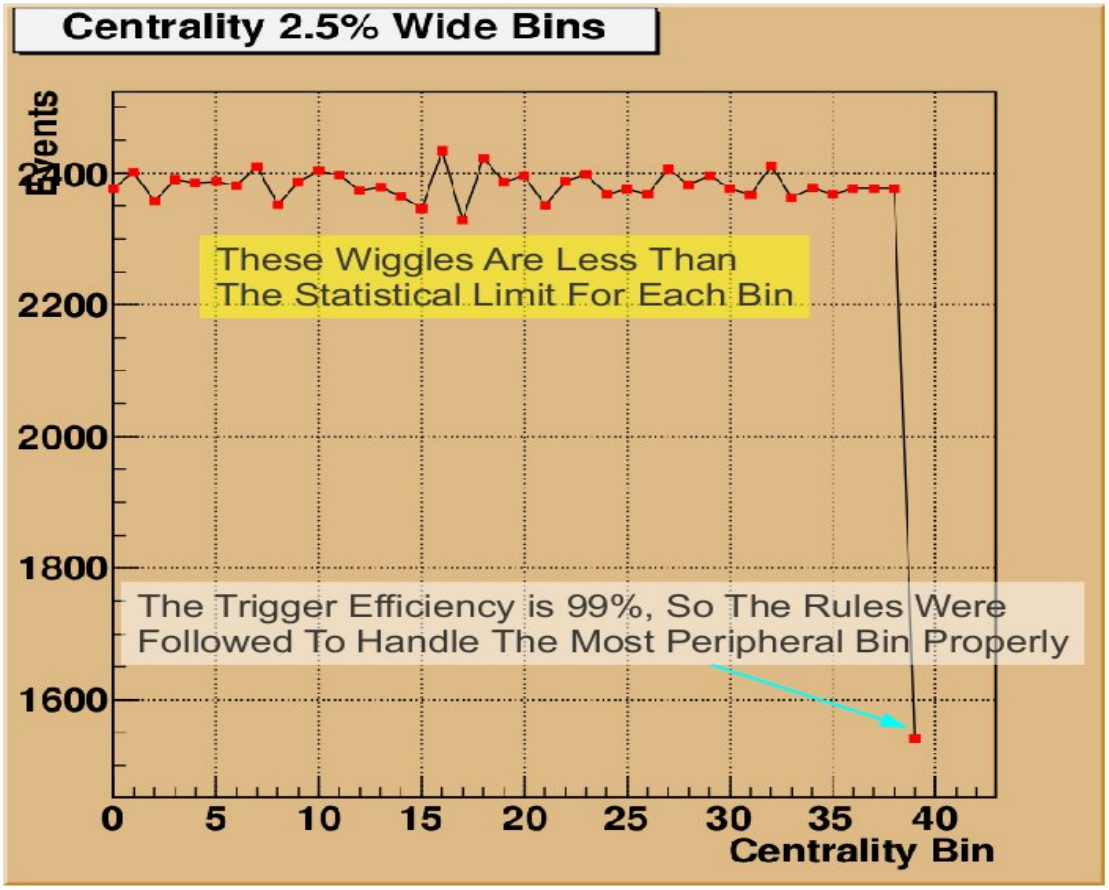

Figure 5.9: The number of events between cuts corresponding to centrality bins is shown here.

each centrality bin and matching them with corresponding events from HF. This is what reweights the HF distributions. Then, the AMPT Monte Carlo is checked for the corresponding number of participants in each HF energy range. A cartoon of how this works is made apparent in Figure 5.10. The comparison of this naively derived average number of participants from the banana plot centralities to those from HF is given in Figure 5.11.

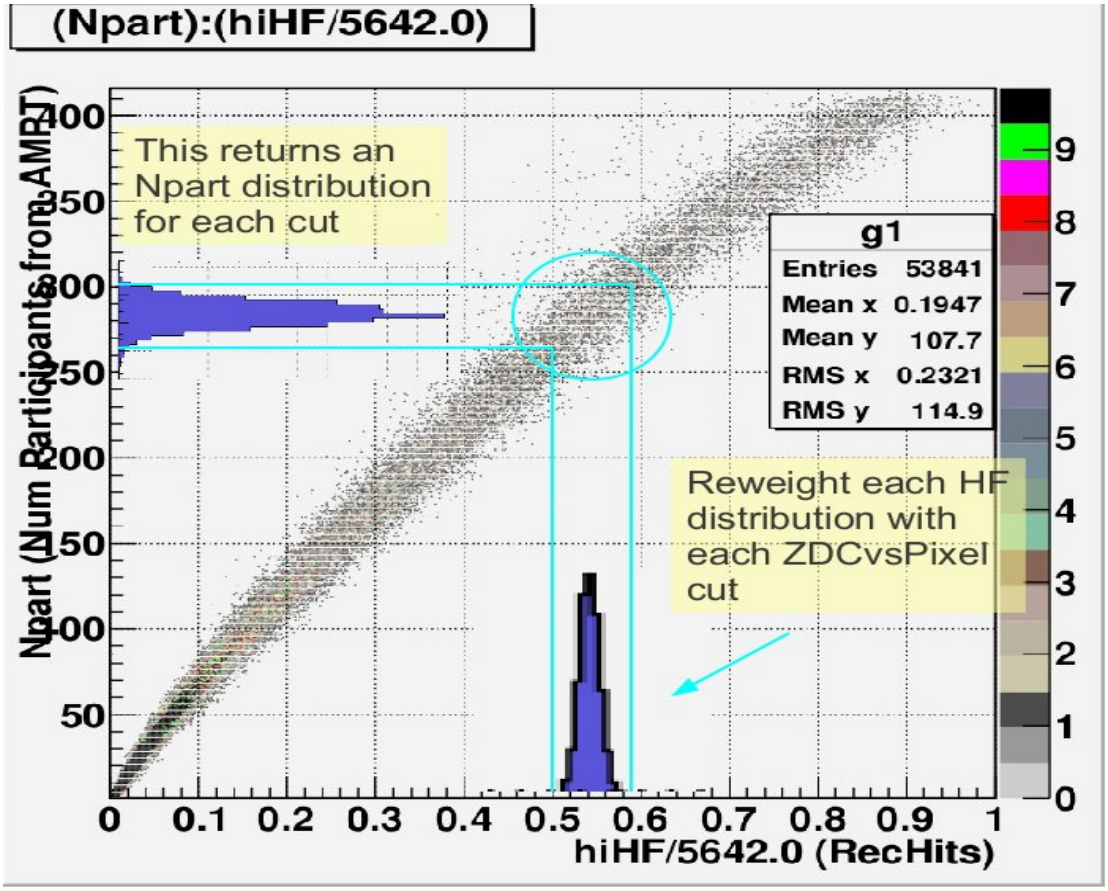

Figure 5.10: The method to derive the number of participants is illustrated here. The HF detector distribution that matches the same cutting criteria as the banana is plotted, and then divided by the total HF distribution for the total events in the dataset. This distribution is mapped to a monte carlo dataset to acquire a corresponding number of participants distribution according to AMPT Monte Carlo.

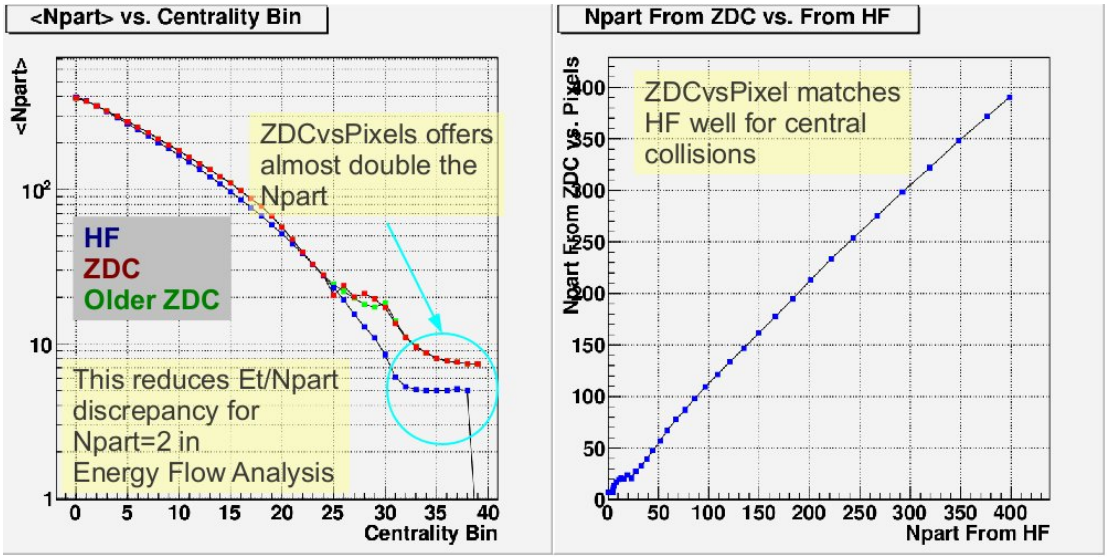

Figure 5.11: A comparison of the number of participants derived from HF and from the banana plot is shown here. The older ZDC plot represents an older set of ZDC cuts utilizing a merger of Regions 2 and 3 using the Region 2 method. This was done to qualitatively estimate the systematic error associated with the difficulty in making cuts in the transition region of heavy-ion collisions.

5.2 Linearized Centrality Method

This section describes several improvements to the signal processing of the ZDC signals that improve the banana plot. Then each event in the banana plot is mapped onto the closest part of the banana plot's profile histogram. This makes it possible to make 1-dimensional centrality cuts, which drastically upgrade the centrality analysis with the ZDC from the "pivot-point" analysis.

There were a couple of key problems with using the "pivot-point" method that are solved by linearizing the banana plot. The first improvement to the centrality analysis is with better signal processing. Without signal processing, the ZDC data becomes digitally saturated because the electronics have a limited dynamic range. This has the effect of actually compressing the ZDC signal when it becomes large. When this happens, semi-peripheral events are too difficult to sort into centrality classes. Also, there is significant noise in the signal that had to be filtered. Fortunately, a method exists to overcome both the saturation and noise difficulties.

The ZDC is timed in well into the CMS clock, and timeslice information has proven reliable. Most of the signal is timed in to timeslice five, and this is where the saturation effect is apparent. It is standard in ZDC analyses to acquire signals in a range that very often includes timeslice five, but data does not need to be plotted from timeslice five in order to show all the signal from ZDC. The addition of signals from timeslices six, seven, and eight proves to reveal all signal from ZDC without any saturation, and the data is observed accordingly in this analysis. Figure 5.12 shows that 90% of the ZDC charge is contained in timeslice five, and it also shows that signals in timeslices seix, seven, and eight are not strong enough to become saturated.

In addition to overcoming the saturation problem, a known problem of significant noise in the ZDC signals also has to be overcome. There are multiple sources of noise. The first source results from the 204 meter electrical cables that feed signal from the ZDC phototubes to the charge integrating encoders (QIEs) in the CMS counting house.

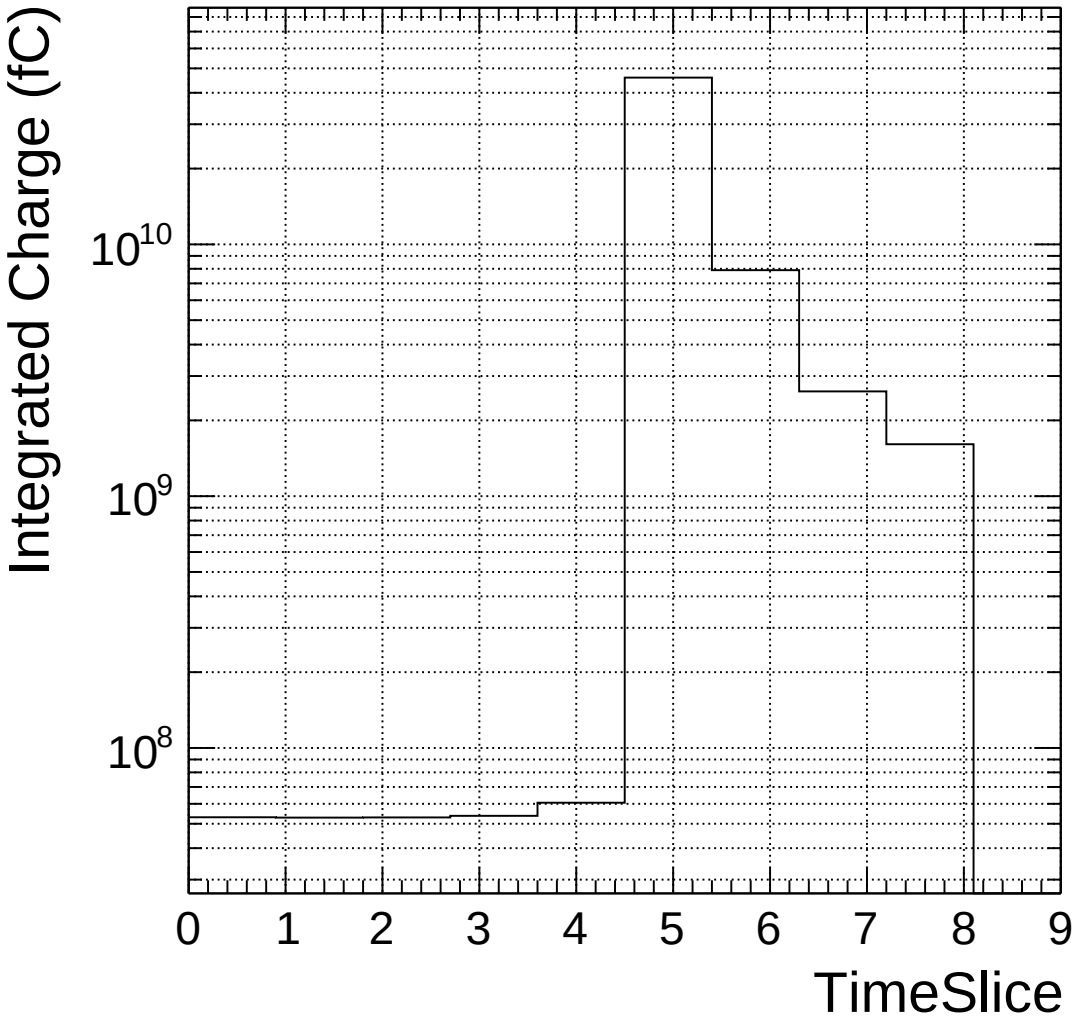

Figure 5.12: A plot of integrated charge readout from the ZDC versus timeslice is shown here. This timing information makes apparent the large amount of signal in timeslice five. Since no loss of information results from adding timeslices six, seven and eight, this was a suitable choice for processing the ZDC signal. Timeslices zero, one and two are certainly noise, and they can be subtracted from the signal measurement to clean up the noise with the same weight.

These long cables are necessary to keep electronics out of the tunnel, where the ZDC is located. It is harder to intervene in the tunnel that it is in the CMS cavern, so keeping maintenance localized to easy-to-access areas is essential for the ZDC. These long cables certainly double as antennae, despite the fact that they are coaxially shielded.

Another source of noise is in the capacitive coupling between the tunnel cable trays and the signal cables. The combination of capacitive coupling effects with long signal paths leads to a low frequency reflection of signal in the cables. The period is on the order of 2 microseconds, which is two orders of magnitude higher than the signal integration time of 25 nanoseconds. This low frequency noise is found to be about 5 millivolts, compared to the maximum dynamic range of about 135 millivolts.

In a fashion consistent with the saturation solution, the noise problem is solved by estimating the noise by considering timeslices zero, one and two. In Figure 5.12, it is clear that the lowest charge signal is localed in timeslices zero, one, and two, which makes this clearly almost all noise. This is a suitable noise estimate in the limit of large numbers of events, and can be subtracted from unsaturated signal. This improved the signal-to-noise ratio significantly for peripheral events, where the ZDC signals drop the least.

The last signal processing step is on the weighting of the electromagnetic section signals to hadronic section signals. These sections exploit different physics processes to distinguish between particles that create both electromagnetic and hadronic showers to those that only create electromagnetic showers. In the case of the ZDC, these are simply the distinctions between showers created by forward photons and those that are created by forward neutrons. In order to properly calibrate the detector for forward neutrons, the two sections must have defined weights that represent the signal divided by the GeV of energy eposited by reactions. In Figure 5.13, it is clear that when the electromagnetic section is weighted at 10% of the hadronic signal, the total signal is independent of the fraction of energy deposited in the electromagnetic section. This has very important ramifications to the detector calibration at large for any analysis, and

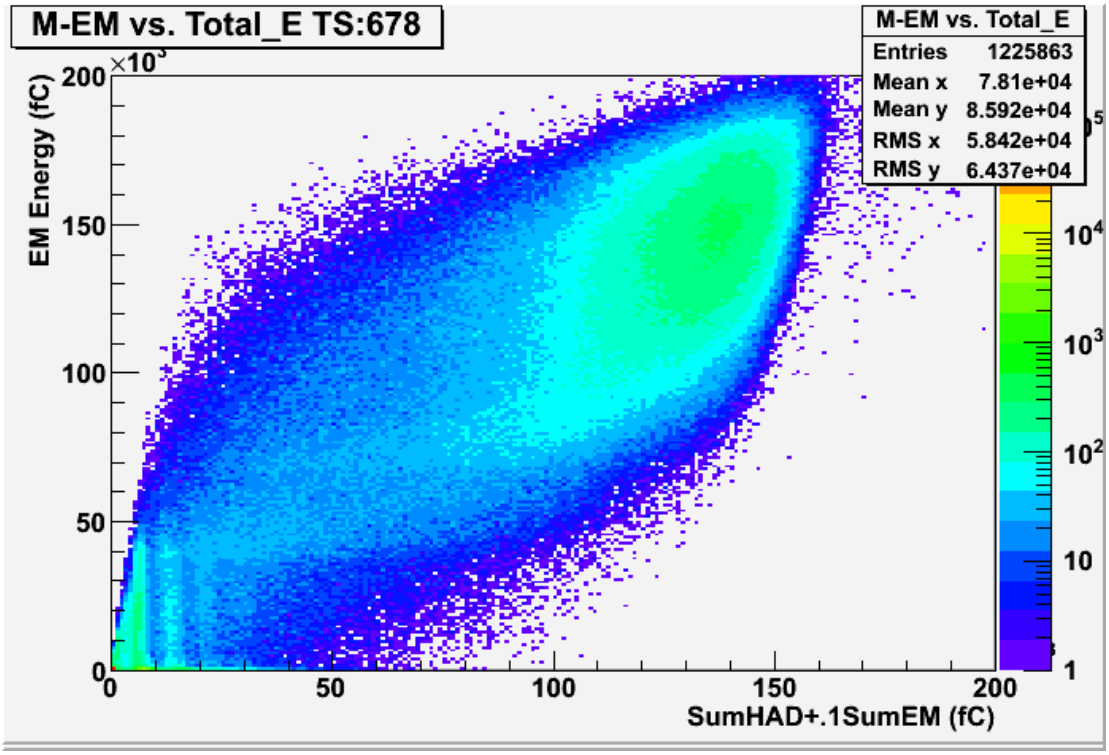

Figure 5.13: A plot of the minus side electromagnetic section ZDC signal versus total signal with 10% weighting on the electromagnetic section is given here. This illustrates the reason to weight the electromagnetic section by 10%. The neutron peaks are clearly visible and gain-matched to measure in consistent detector units between sections this way.

the centrality analysis here is no exception. This analysis must depend on a reliable measurement of spectator neutrons, which Figure 5.13 confidently displays.

Figure 5.14 shows the processed ZDC signal versus pixel multiplicity. The processed signal is given by $ZDC = 0.1 * (EM - EMnoise) + (HAD - HADnoise)$, where ZDC is the processed signal from ZDC, EM and $EMnoise$ are the electromagnetic section signal and noise respectively, and HAD and $HADnoise$ are the hadronic section signal and noise respectively. The region labeled 1 corresponds to central collisions where the nucleus evaporates. Centrality derivations here should be quite model independent, and therefore offer a good sanity check with other centrality methods. Region 2 is the peripheral collision region. Here, the physics is dominated by the nucleus breaking up into fragments of varying size and charge-to-mass ratio, because it is not hit as hard as

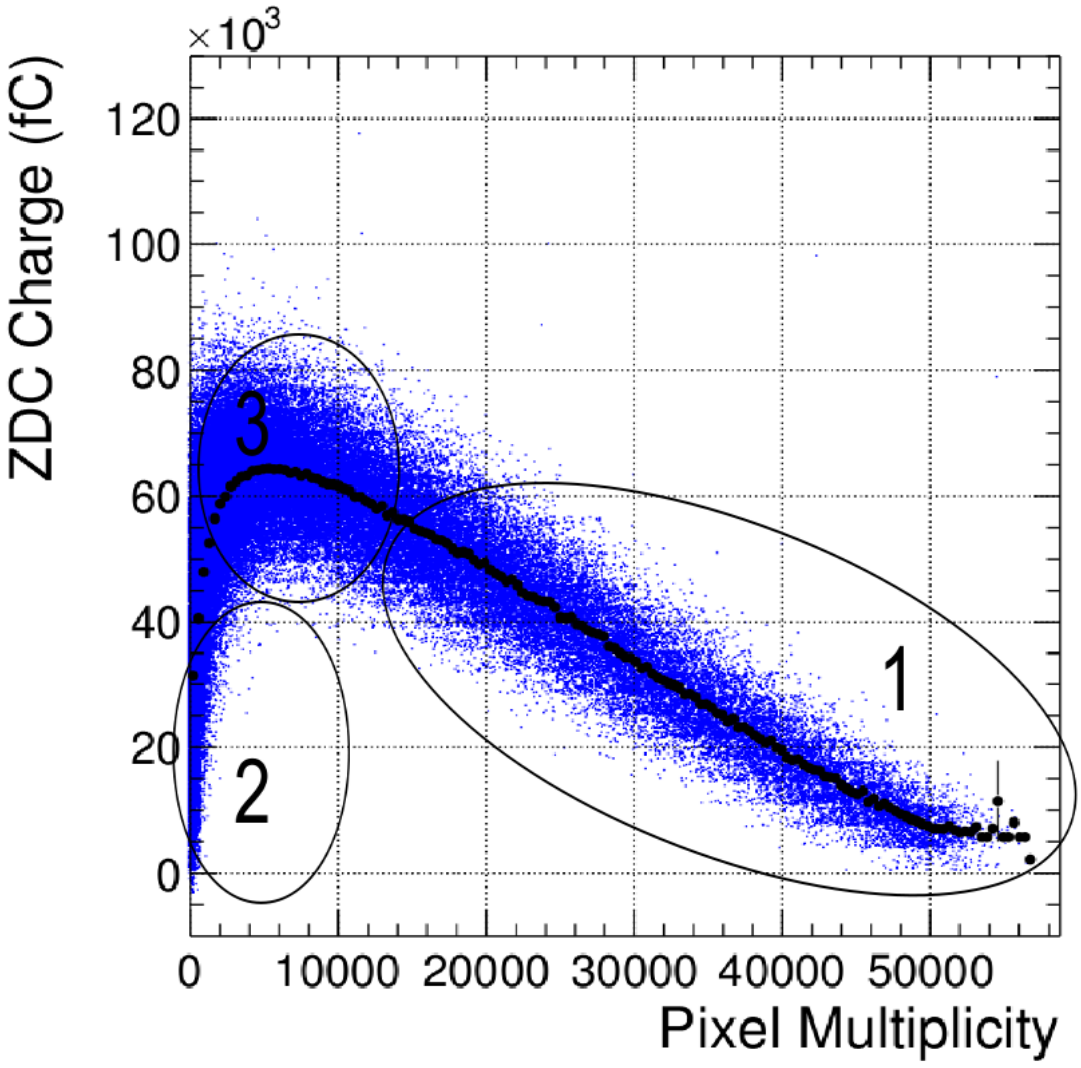

Figure 5.14: A plot of ZDC charge and pixel multiplicity is shown here. This is the rawest dataset useable to obtain a centrality measurement.

in central collisions. This process is known as multifragmentation [55], and it can lead to fewer neutral spectators when comparing with the trend set by evaporative nuclear processes. Multifragmentation tends to set large statistical fluctuations in the number of neutral spectators, so this is why the ZDC response is so broad here. Labeled region 3 is the cusp of the banana plot, and is the transition region of heavy ion collisions. The physics is a mixture of evaporative and multifragmentation effects, and this makes region 3 the most delicate part of the analysis.

A very important point that must be addressed right away is that region 2 is treated separately in the analysis from the others. This is because the profile histogram, which is the average ZDC signal as a function of pixel multiplicity, ends when region 2 begins. The bulk of the centrality analysis depends upon the profile, so a modification to the centrality determination is unavoidable in region 2. Fortunately, it turns out that this begins at centrality greater or equal to 90%, which corresponds to extremely low N_{part}. Therefore, a global linear inequality cut is applied right away to the banana to remove region 2 events from the main analysis. The global cut is: $PIX < 0.10\ XOR\ (-0.045) * PIX + (0.31) > ZDC$ where ZDC stands for normalized ZDC charge, PIX stands for normalized pixel multiplicity, and XOR is the exclusive-or operation. A picture of this global cut is given in Figure 5.15. It should be noted that the slope of the second cut is perpendicular to the profile at zero pixel multiplicity for the sake of continuity. Also, the vertical cut is necessary because the banana is not single-valued in ZDC charge, and interference of the linear inequality cut is avoided at high pixel multiplicity.

Since it is necessary to avoid detector bias in these measurements, a unit convention is selected in both ZDC and pixel hits. With a clean signal in the ZDC by the manipulation of timeslices, there is a strong anticorrelation between ZDC charge and pixel multiplicity. This can be exploited by considering the physics of central collisions, where pixel multiplicity is generally largest. Since the nucleus essentially evaporates in central collisions, conservation of energy causes an anticorrelation between particles produced near central rapidity and forward energy flow. This is what makes analyzing

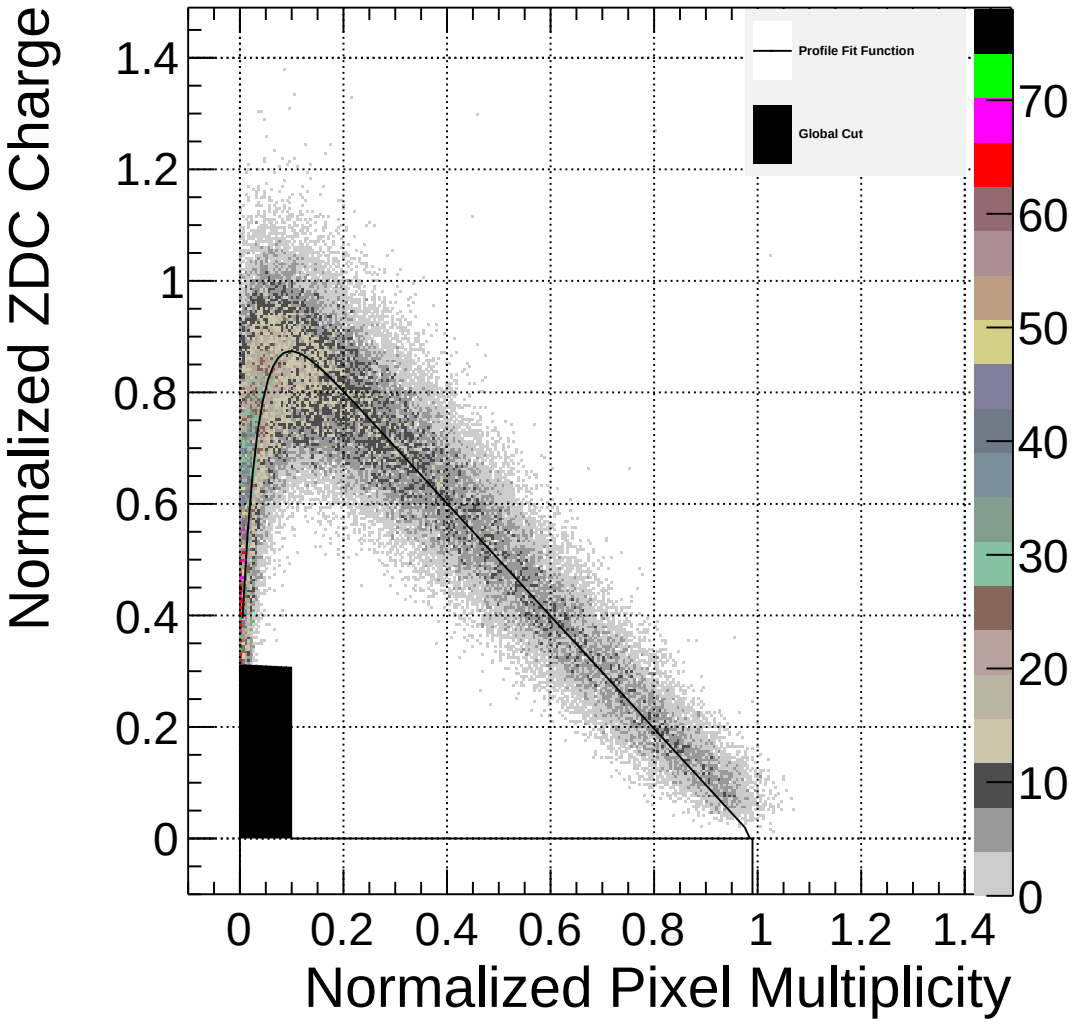

Figure 5.15: A banana plot with the global cut applied, given in black, is shown here.

correlations in the ZDC and pixel multiplicity so powerful in this analysis. The forward energy deposit in the ZDC and the proportionality of pixel multiplicity to energy of high transverse momentum particles is quite idealized. To exploit this, units of ZDC charge and pixel hits are normalized to create a trendline with a slope of -1 between the two for central collisions. This, geometrically, creates a 45 degree trendline of average ZDC signal for a given pixel multiplicity.

Upon setting appropriate detector units, the centrality analysis becomes independent of the gain of the detectors. Additionally, this diagonalizes the metric corresponding to detector signals and also makes plotting square. This choice of units means that both detectors are given equal weight in the determination of centrality. A side effect of this is that visualization is more intuitive upon plotting, since the centrality cuts to the banana plot are two-dimensional. An example of a square banana plot is given in Figure 5.16.

The profile of the ZDC versus pixel multiplicity scatterplot produces a locus of points in ZDC charge that is single-valued with pixel multiplicity. This means the analysis is indeed linearizable. To linearize the analysis, the profile histogram is binned in arbitrary units of arclength. In this way, the scheme that works for central collisions can continue onward because the centrality cuts scale with differential arclength of the profile.

The main complication to making perpendicular cuts to the profile histogram of the banana everywhere is that the transition region of heavy ion collisions causes this to break down dramatically. This is why the method descibed in Section 5.1 was abandoned. Linear inequality cuts that satisfy central collision analyses quickly begin to intersect each other in populated regions of the banana plot within large $\frac{dN}{dZDC}$. It is clear that a generalization of a most model-independent nature is needed to handle a non-linearized scheme involving a two-dimensional analysis of this kind.

The best way to parameterize events to the arclength of the profile histogram is by analyzing which events are closest to a given arclength of the profile. It is better to have a profile histogram that is smooth, so it is fit to a smooth curve that plots ZDC

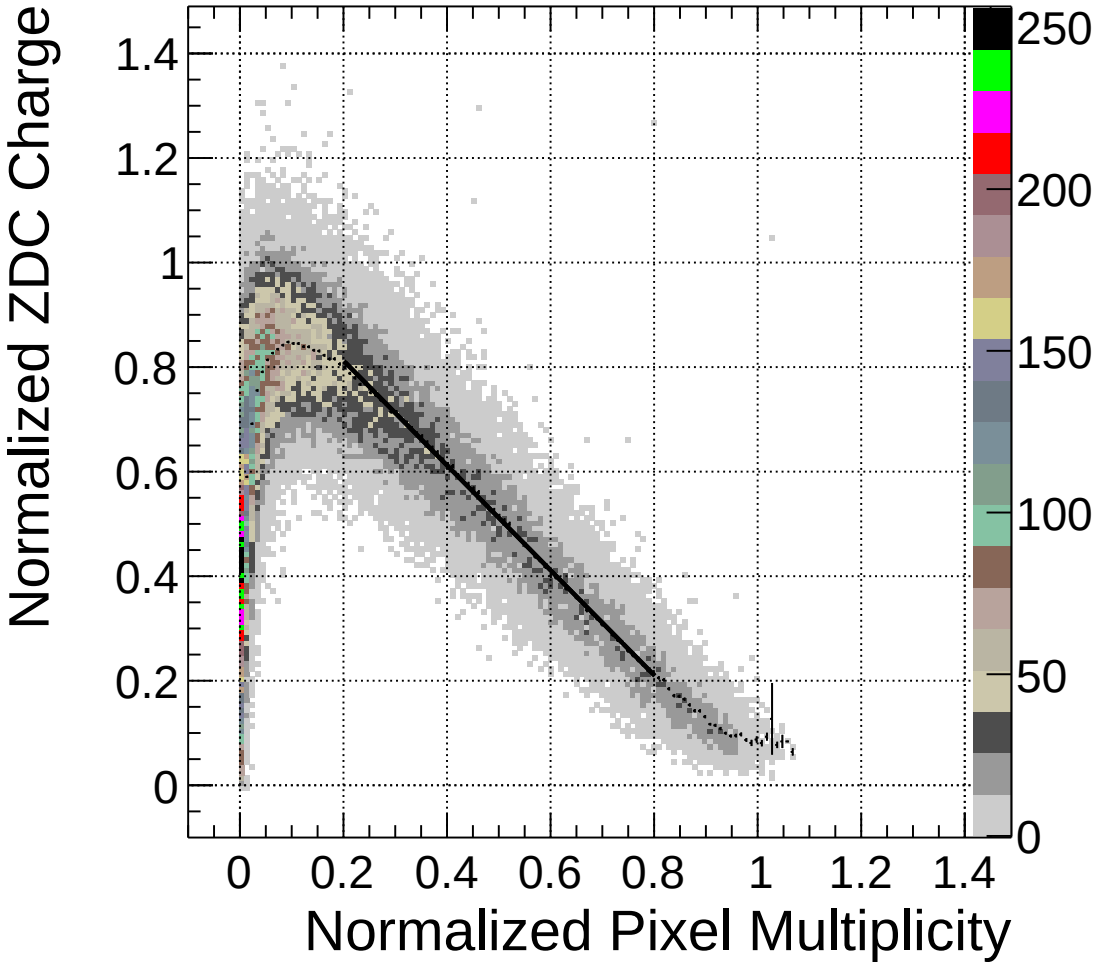

Figure 5.16: This is a banana plot without saturation in the ZDC. The plot area is square, so, by choosing appropriate units for ZDC charge and pixel multiplicity, the central collision region of the banana plot can be chosen to match a 45 degree line of total negative correlation. This is an effect of energy conservation.

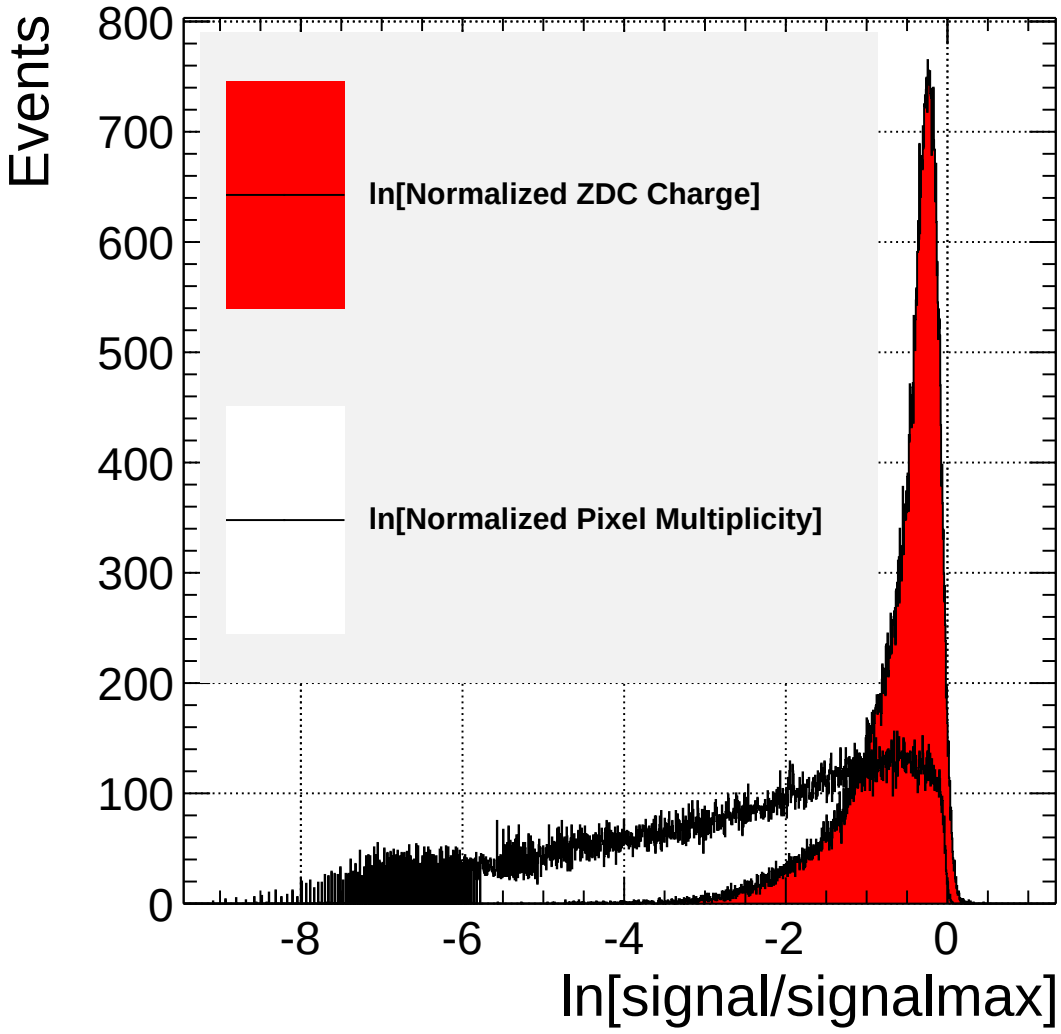

Figure 5.17: A plot of the logarithms of the signals in both the ZDC and pixels is shown here. When the ZDC signals are largest, they correspond to the cusp of the banana plot, where pixel values are low.

charge as a function of pixels. The fitting function is: $ZDC = 1.0 - PIX - (0.61 * exp(-PIX/0.032))$. A plot of this fit with the original profile histogram is shown in Figure 5.18, and the difference of the data from the fit is shown in Figure 5.19. This arclength parameterization ultimately serves to produce a plot of $\frac{dN}{ds}$ versus s where s is the arclength of the profile fit. This plot serves as the solution needed that makes sorting for the centrality linear. This is because the nuclear collision cross section scales with only one variable in this step, which is the arclength.

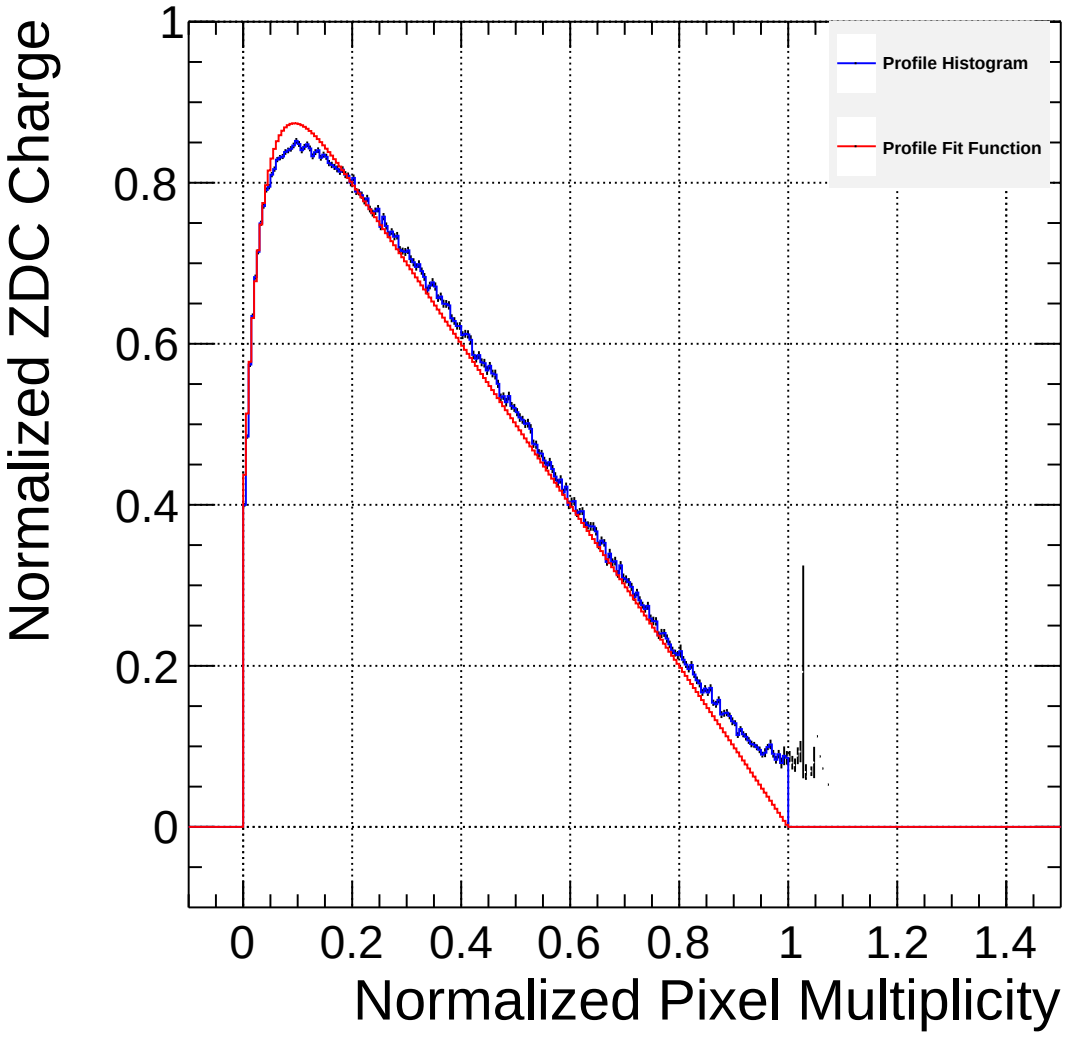

Figure 5.18: A plot of the profile fit function and the original profile histogram are both shown here. The fitting function hugs the data very well.

The goal of this analysis is to divide the banana plot into even nuclear collision cross sections. The main difficulty to this effort is at the cusp of the banana plot. Here, the profile histogram has the most curvature, so $\frac{ds}{dpixel}$ is largest. Additionally, in Figure 5.17, another difficulty is made apparent at the cusp. When the ZDC signals are largest, they correspond to the cusp of the banana plot, where pixel values are low. In order to maintain even nuclear collision cross sections to derive centrality, more precision is needed to handle low pixel multiplicity bins than in higher ones.

Another source of uncertainty is independent of detector signals. In Figure 5.20, obvious physics fluctuations from the mean signals increase as collisions become more peripheral, and as the ZDC signals become larger. In particular, in Figure 5.20, multi-fragmentation effects spread the ZDC signals quite dramatically between the plus and minus sides. This is due to the random behavior of multifragmentation. It is clear that from the cusp and towards more peripheral collisions, more precision is needed to handle these regions than in central, where the physics is much more deterministic. Even two ideal detectors situated with one at central rapidity and the other at forward rapidity should always find this unavoidable.

The precision problem at the cusp is solved by plotting the logarithm of pixel multiplicity. In order to continue avoiding bias in detector parameters, the ZDC charge is also plotted with the same logarithmic scale as pixel multiplicity. So, the double logarithmic mapping maintains a geometrically flat and square plot area to analyze. A log-log plot of the banana is given in Figure 5.21. It should be noted that the cusp of the banana plot is much more stretched and flattened in this logarithmic scaling of both signals, which relaxes the analysis to a great degree. With this plot, assigning events to a particular arclength of the profile histogram can begin.

A mapping of events to arclengths of the profile histogram is ready to begin after the log-log banana plot is produced. The first thing to note is that it is easier to parameterize such events as integer indices assigned to arclengths of the profile instead of the arclengths themselves. All parameters needed for the centrality derivation can

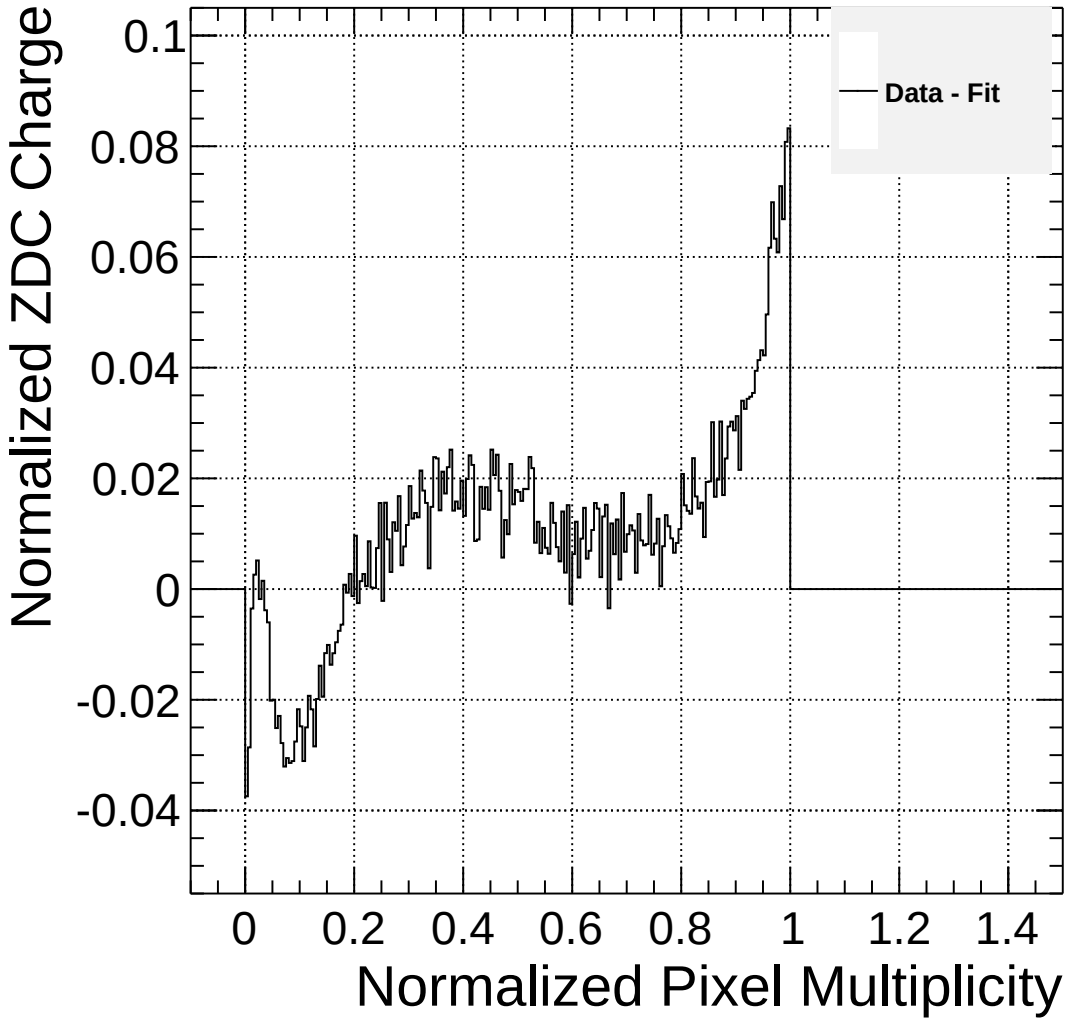

Figure 5.19: A plot of the original profile histogram minus the profile fit function is shown here. The precision is within less than 10% everywhere. The dip at about 0.1 pixel multiplicity corresponds to the top of the banana plot, which is the most difficult to analyze.

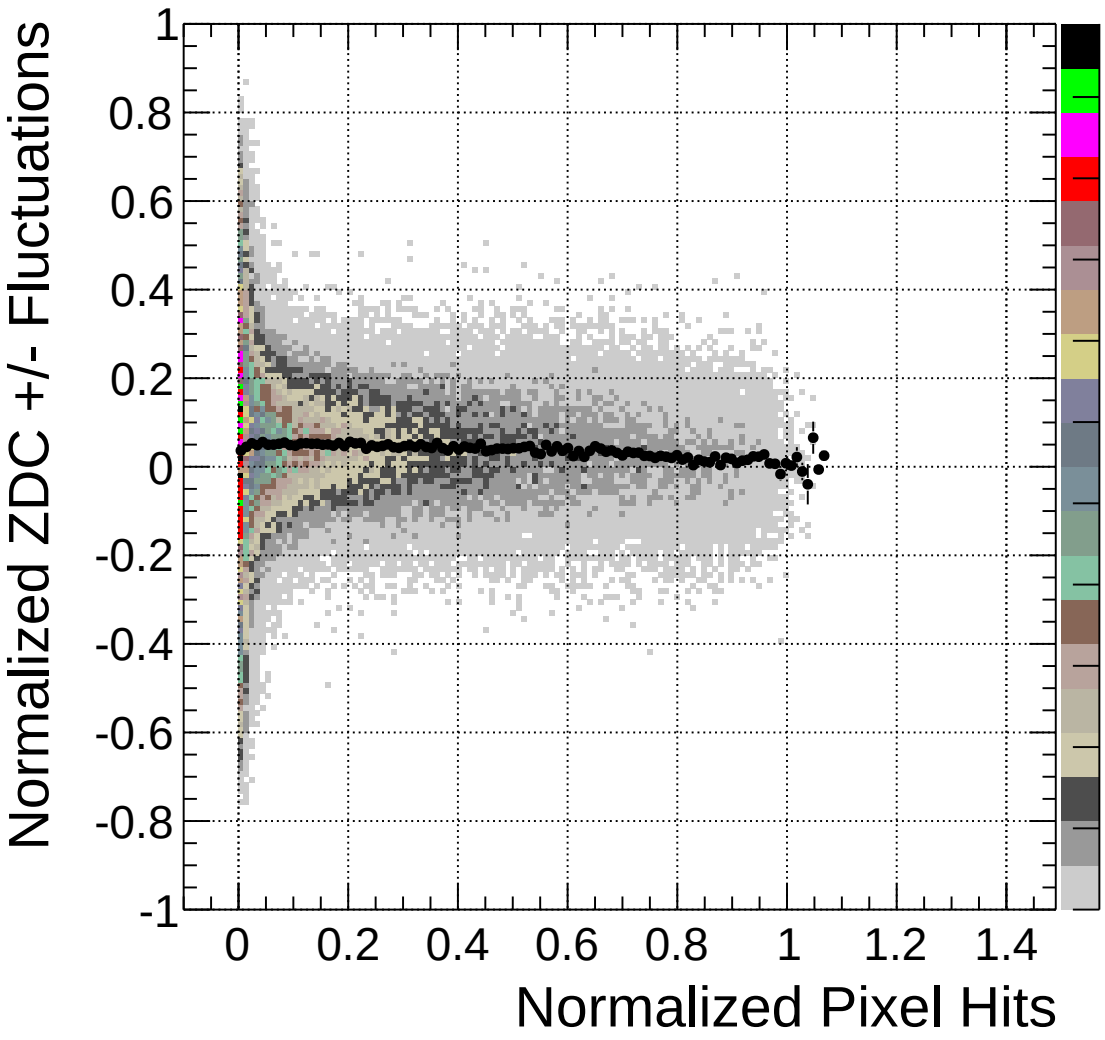

Figure 5.20: A plot of the difference of the plus and minus side signal in the ZDC divided by their sum versus pixel signal is shown here. Multifragmentation begins to dominate the statistics toward peripheral collisions, which correspond to low pixel hits.

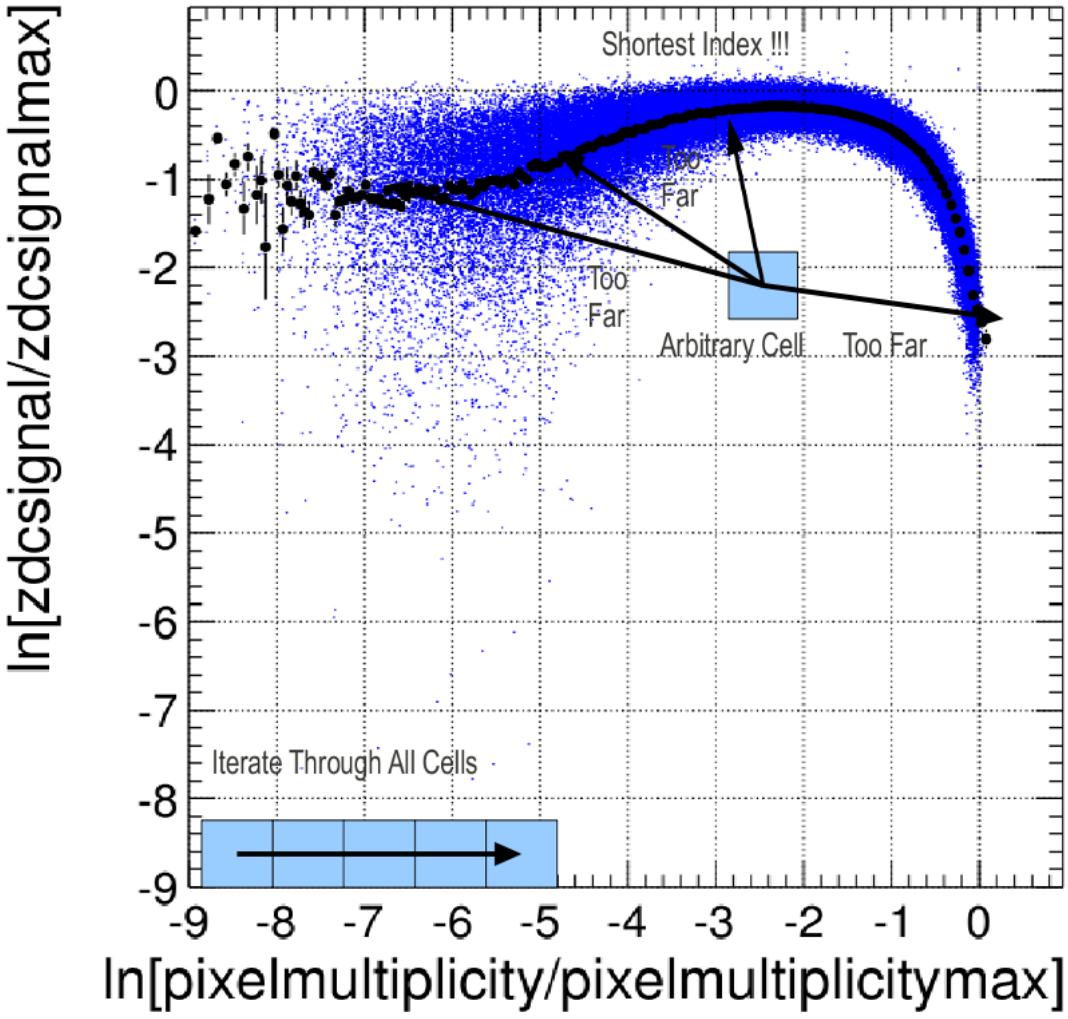

Figure 5.21: A banana plot shown in logarithmic scale in both axes is shown here. The binning has been adjusted to be even width throughout the scale in each, which is necessary to analyze centrality in peripheral collisions with enough precision. A simplified illustration of how cells are sorted by pixel indices is also shown.

use these indices as a common parameter between arclength and pixel multiplicity, since the fitting function of the profile is single-valued in pixels. So, the arclength is not actually needed, just a consistent binning of the profile instead. The method used to assign profile bins to events begins with dividing the square plot area of the log-log banana into a two-dimensional mesh. The units of the mesh, called cells, are then each tested to assign the profile bin corresponding to the profile fit's closest point to that cell. This creates a two-dimensional finite minimization analysis of the entire plot area. Figure 5.21 doubles its purpose when used in visualizing the steps taken to assign cells to a particular profile index. It should be noted, however, that the distance is calculated in linear space in both the ZDC and pixels, not logarithmic space.

The reason that cells are used instead of individual events in datasets is twofold. First, this analysis is designed to generalize centrality results for any dataset. Second, a consistent bin size for the logarithm of pixel multiplicity and the division of the profile fit is required for this analysis to have any consistent units of measure. This is because the profile fit is a function of pixel hits. A system of units has to be chosen here.

Both the logarithm of ZDC Charge and the logarithm of pixel multiplicity are binned to divide the plot area into a 2000 by 2000 cell mesh. This results in a mesh that is small compared to the sizes of the centrality bins. This is also meshed to account for all the dynamic range of both the ZDC and pixel signals. The easiest way to visualize the results of the analysis is given by a two-dimensional color-coded mesh. For this reason, the plot is called a color map when the analysis is finished. A resulting color map is shown in Figure 5.22 based on the profile.

After this reference color map is made, it can be used to count the number of collision events from a heavy ion dataset lying on each cell. All the events are then tallied for each profile index, and then they are stacked into a histogram called the profile index histogram. This results in a plot that counts the number of events corresponding to each point on the profile. The profile index histogram is very exciting because it is completely analogous to a plot of $\frac{dN}{ds}$ versus s, where s is the arclength of the profile fit.

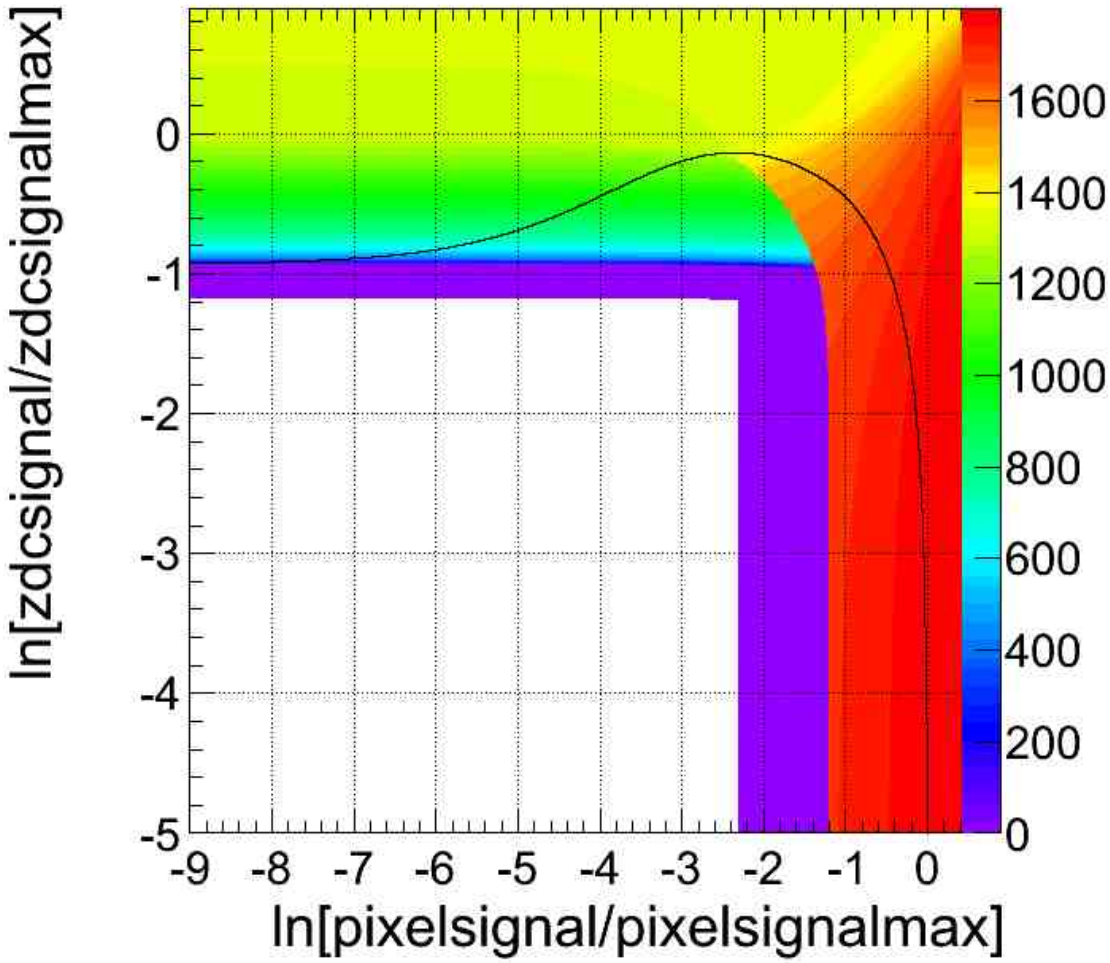

Figure 5.22: A plot of indices of the profile that arbitrary events plotted as responses of ZDC charge and pixel multiplicity are closest to is shown here. The large lower left-hand corner space corresponds to the very peripheral collision region where the profile is no longer used for the derivation of the centrality.

This means that this plot is the step that linearizes the problem. Now, all events are parameterized by one variable, the profile bin number, which is a function of arbitrary differential arclength. Again, the arclength is not explicitly needed. Just a consistent binning shared by the color map and the profile index histogram is needed instead, which is given by the profile indexing. An example of how a banana plot gets linearized into a profile index histogram is given by Figure 5.23. Region 2, from Figure 5.14, of course, is still left out of this stage of the analysis, as it must be consistent with the color map. The color map only is applicable to the profile range. The leftover events in region 2 are accounted for after this.

Since the banana plot is now linearized by profile indexing, it is a trivial matter to sort events into even nuclear collision cross sections. Figure 5.24 is sorted through from high pixel signals to low to derive centrality bin boundaries. Pixel signal, rather than profile index, is plotted because it is easier to compare Figure 5.24 to the banana plot this way. This sorting can then be used to derive a centrality bin as a function of profile index. This is another good reason to choose to parameterize by a profile index, rather than an arclength, because centrality can be stated discretely in terms of the profile index. It simply makes accounting easier, and more consistent. The minimum bias trigger efficiency here was 99%, so the last centrality bin handles the leftover events. The number of leftover events are given, in general, by the formula $(totalevents) * (1 - \frac{1}{(39)(0.99)}) = leftoverevents$. Since profile index histogram is able to sort up to centrality bin 36 out of 0 through 39, this does not apply here, but only to the last cut handled in region 2.

Once centrality as a function of profile index is sorted through, a new color map, the centrality map, can then be created. This can be done by sorting through the color map and using the centrality bin to profile index parameterization to convert the previous color map into a centrality map. An example of this conversion is given in Figure 5.25 in a logarithmic scale and in Figure 5.26 in a linear scale in both detector signals. Now, a reference plot exists to sort any heavy ion collision event by a centrality bin. To state

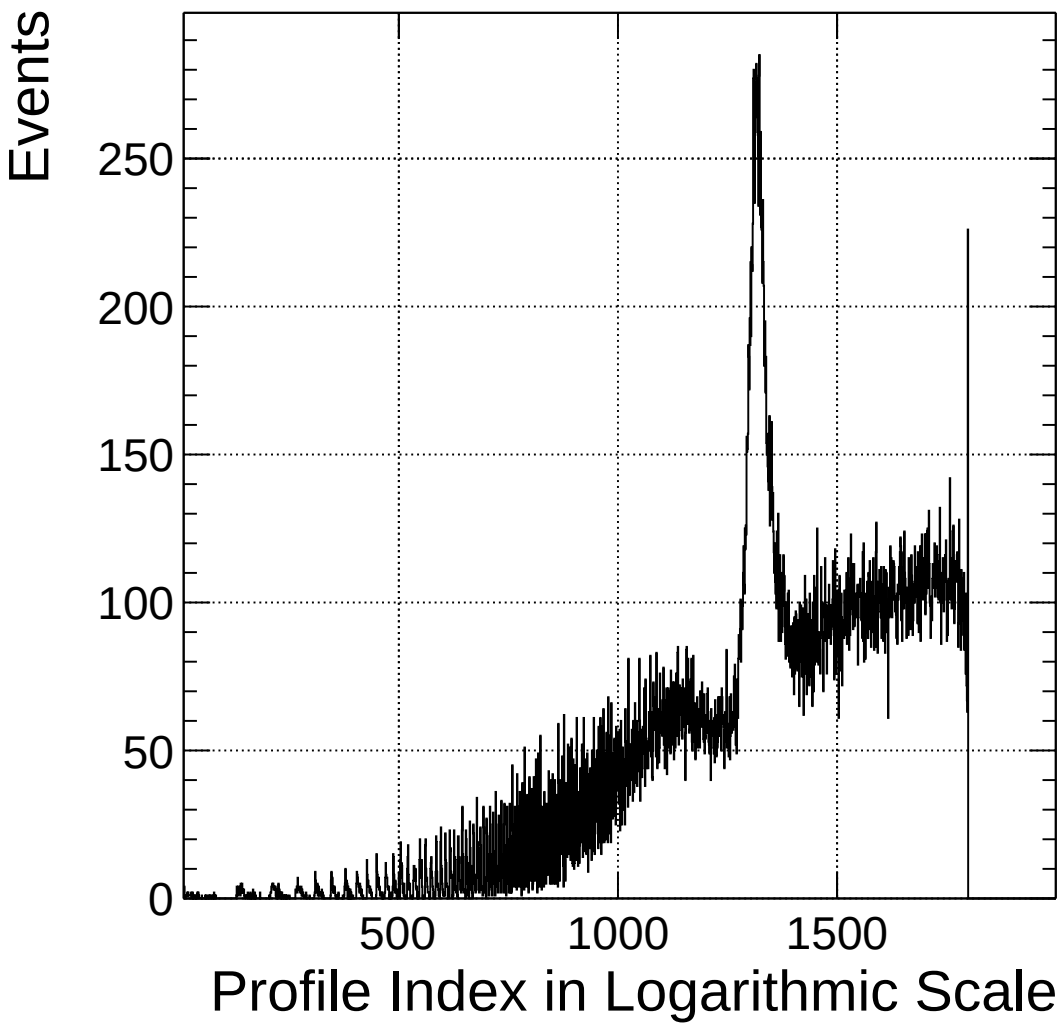

Figure 5.23: A plot of the number of events from the banana plot that are contained in each index of the color map is shown here. This linearizes the banana plot into a sortable dataset that can be used to locate profile indices that define centrality bin boundaries. The large peak corresponds to the peak of the profile, the most complicated part of the analysis.

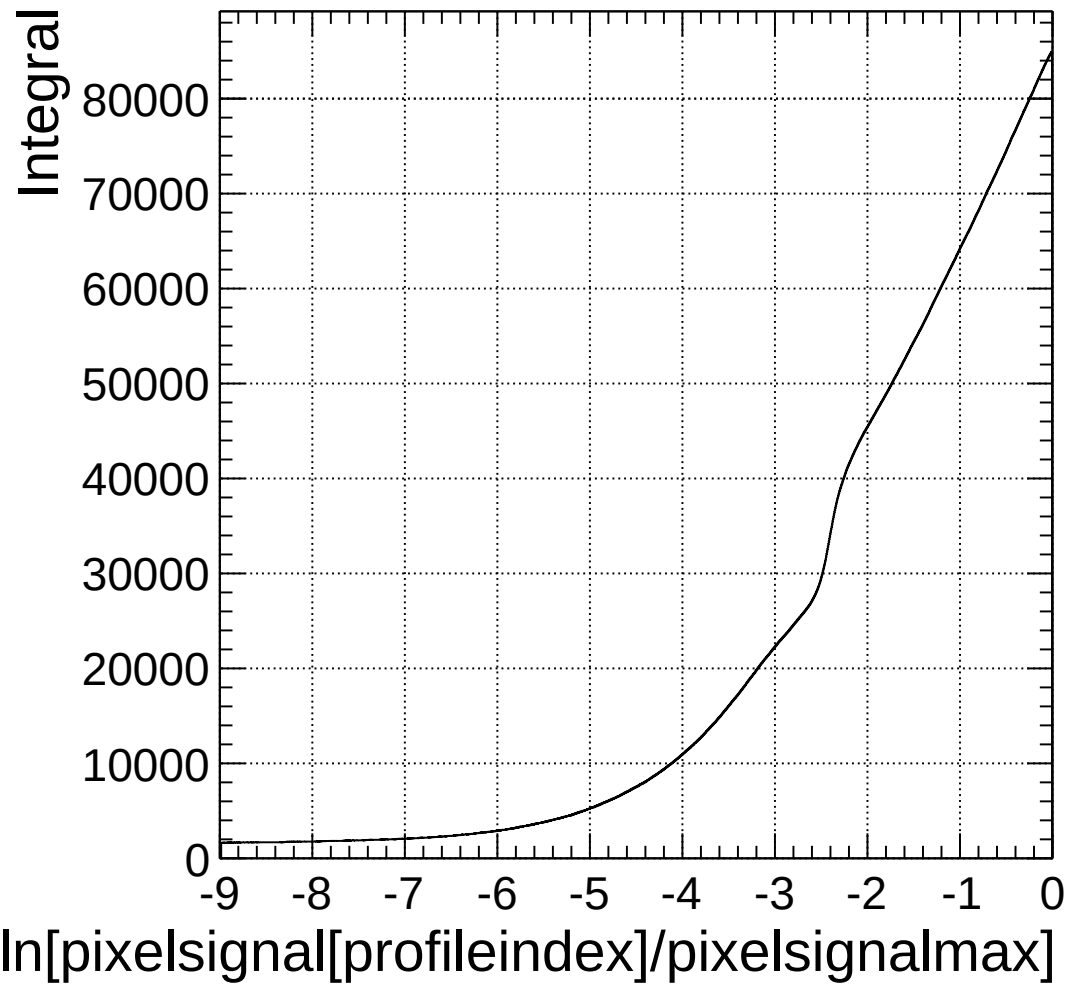

Figure 5.24: A plot of the integral of number of events from the banana plot that are contained in each index of the color map is shown here. It is plotted as the cumulative sum vs. the logarithm of pixel signal because pixel signal is one-to-one with the arclength of the profile. This is the histogram that sorts from large pixel values to low to derive centrality boundaries.

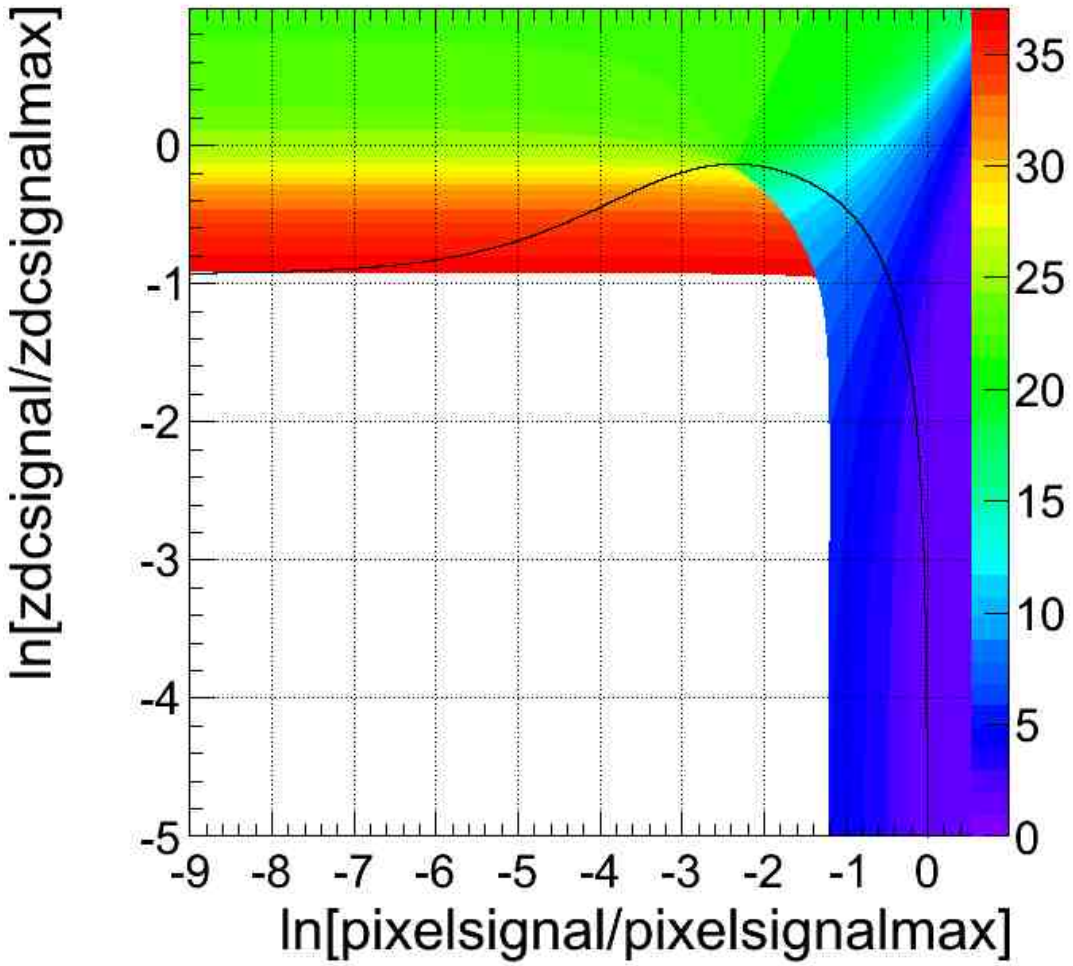

Figure 5.25: This is a color-coded map of regions of centrality that events plotted as responses of ZDC charge and pixel multiplicity correspond to. Both axes are plotted both logarithmically. The blank space in each plot is a region reserved for constant slope linear cuts because the profile does not cross these ZDC values.

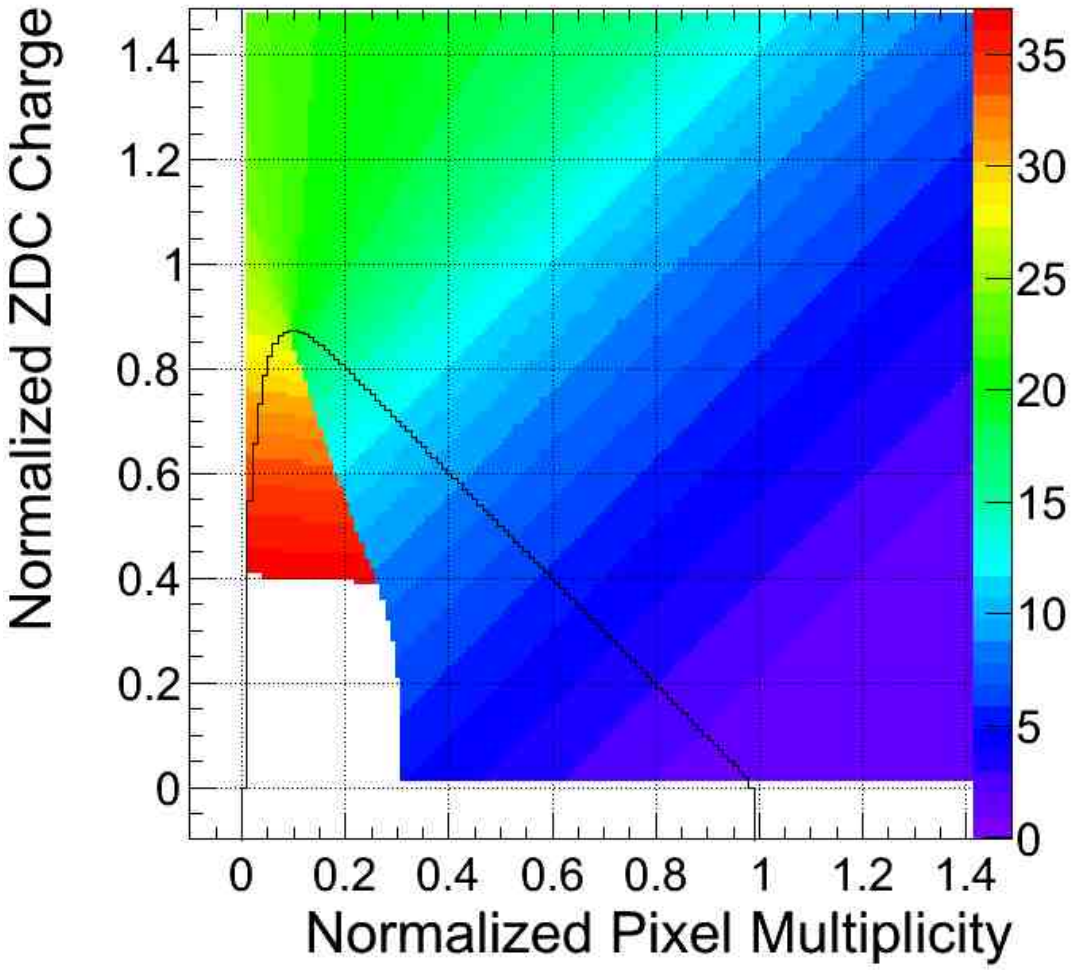

Figure 5.26: This is a color-coded map of regions of centrality that events plotted as responses of ZDC charge and pixel multiplicity correspond to. Both axes are plotted both linearly. The blank space in each plot is a region reserved for constant slope linear cuts because the profile does not cross these ZDC values.

it another way, all the profile indices are not needed to display a centrality map. All the cells that have profile indices that correspond to a particular centrality can be assigned the same centrality bin. The best way to visualize this is to assign a color to centrality bins 0 through 36 in a fashion consistent with the profile index color map. The profile index is no longer needed for any remaining part of the analysis because of this.

It is now possible to use the centrality map to run through collision data and organize it by centralities up to 90%. Region 2 of the banana plot remains after this analysis, but it is much more trivial to handle. The last four centrality bins are scanned and sorted for increasing ZDC charge by varying the ZDC-intercept of the cuts applied there while maintaining a constant slope. The constant slope is the slope of the fit profile histogram at zero pixel multiplicity. The form of the constant slope cuts is given by $(-0.045) * PIX + (ZDC - intercept) > ZDC$. The first constant slope cut invades the centrality map that covers bins 0 through 36 because the last centrality bin within did not have sufficient cross section to cutoff at the correct centrality, which, again, is 90%. In general, it is expected not to be lucky enough to cutoff at the exact previous centrality boundary when finding a continuous spline of two centrality derivations.

An example of a banana plot color-coded by centrality bins is given by Figure 5.27, which is the result of the complete analysis. As a sanity check, a banana plot of the same color code is plotted as ZDC charge versus HF energy in Figure 5.28. Figure 5.28 shows that for central collisions, the anticorrelation between the ZDC and HF signals remains as strong as those between the the ZDC and pixel signals. Also, Figure 5.28 shows that the event selection is smeared in ZDC charge versus HF energy banana plot compared to the sharply defined bins in the ZDC versus pixels banana plot in Figure 5.27. The centrality derived from HF is the result of sharply and evenly dividing the cross section of the total HF energy distribution. However, by comparison, Figure 5.29 shows how the centrality bins are reweighted and smeared from the centrality derived from the ZDC and pixel signals. A few examples of the ZDC versus pixels banana plot with the centrality derived from HF are color-coded and given in Figure 5.30.

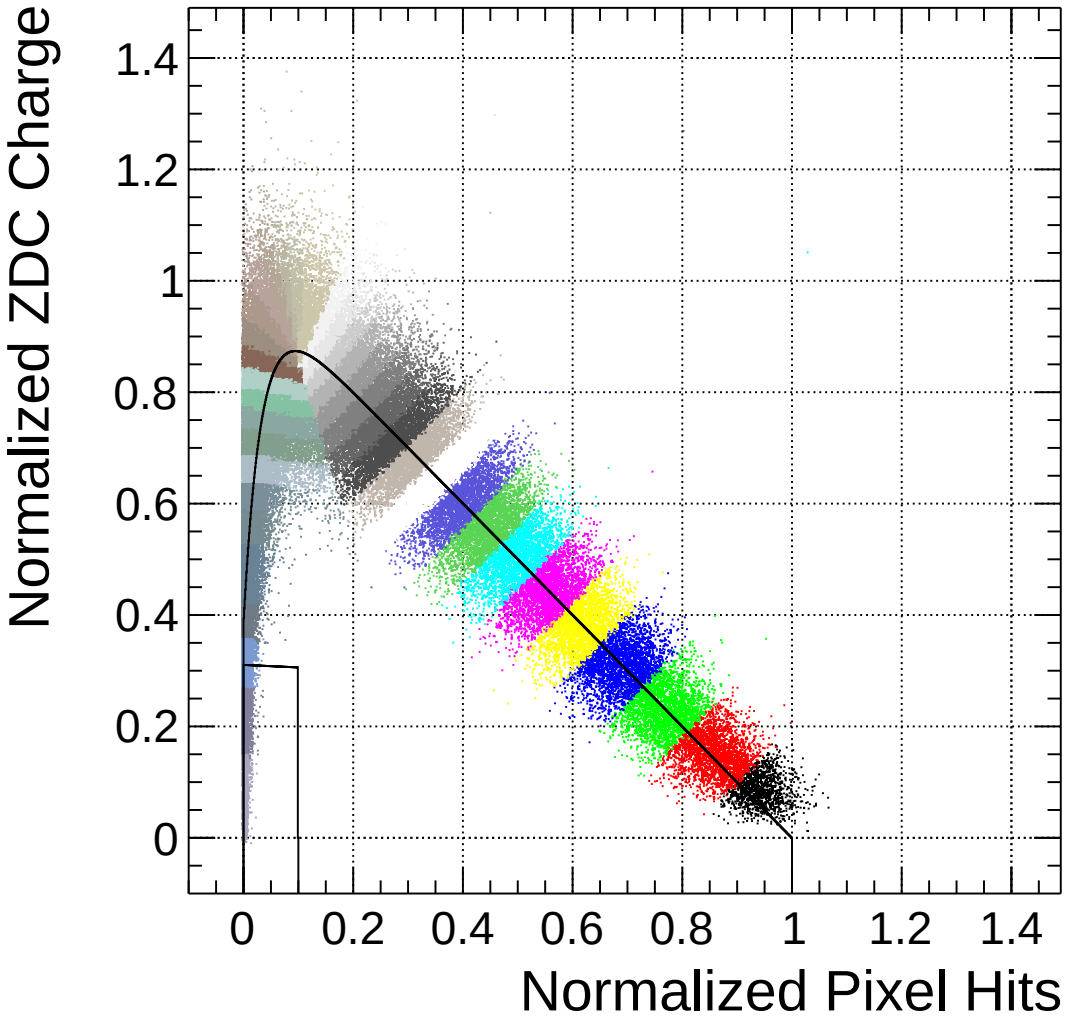

Figure 5.27: Applying the logarithmic centrality map criteria to the ZDC charge vs. pixel multiplicity data results in a banana plot divided by proper centrality bins. There are linear and constant slope cuts for the last four centrality bins corresponding to the centrality map limit.

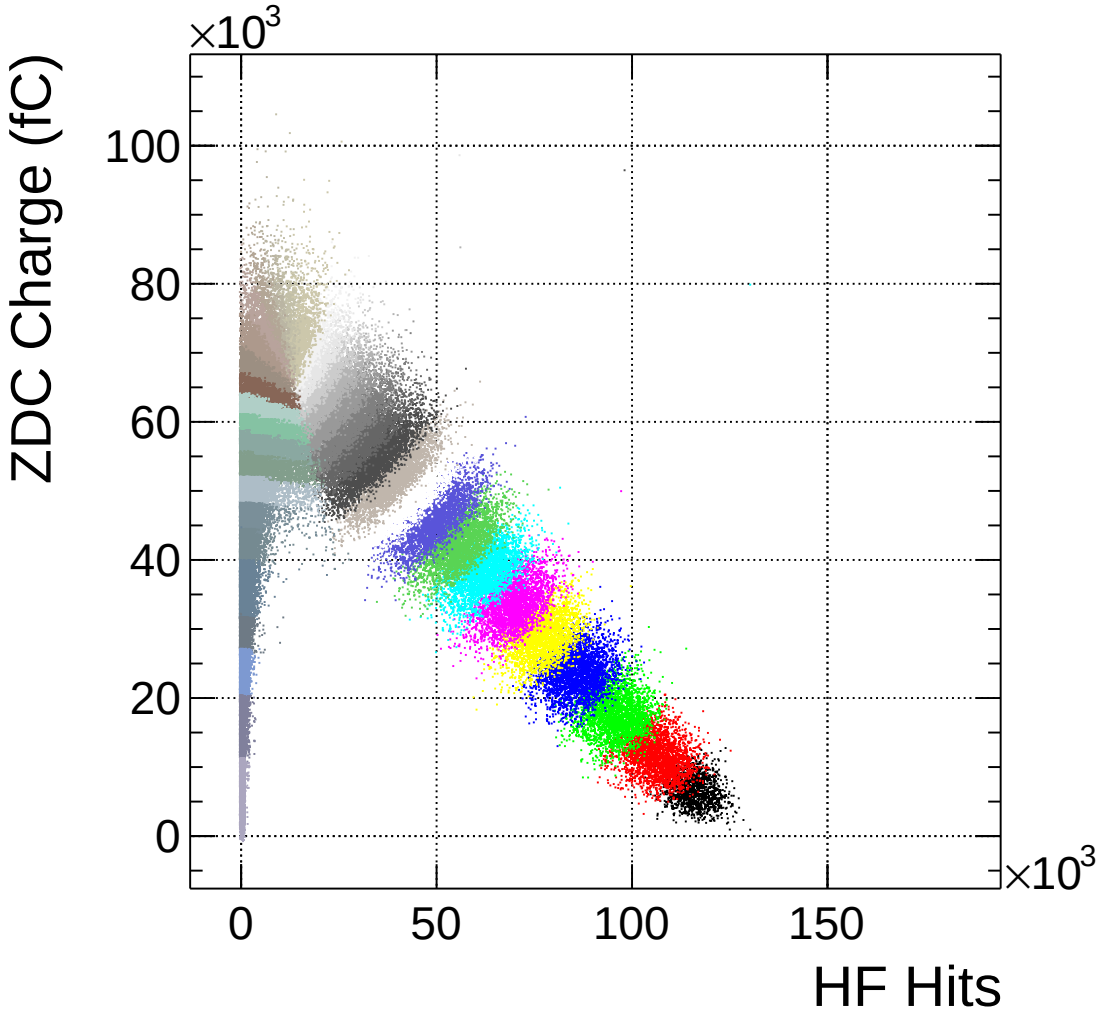

Figure 5.28: A plot of ZDC signal vs. HF hits is shown here with the same color-coded centrality bins as defined by Figure 5.27. This is completely analogous to Figure 2.2 when applied to CMS. There is some slight smearing between centralities defined by the ZDC vs. pixels derivation as compared to the sharp boundaries in Figure 5.27. The correlation between ZDC and HF in central collisions is still more well-defined as compared to previous generation experiments.

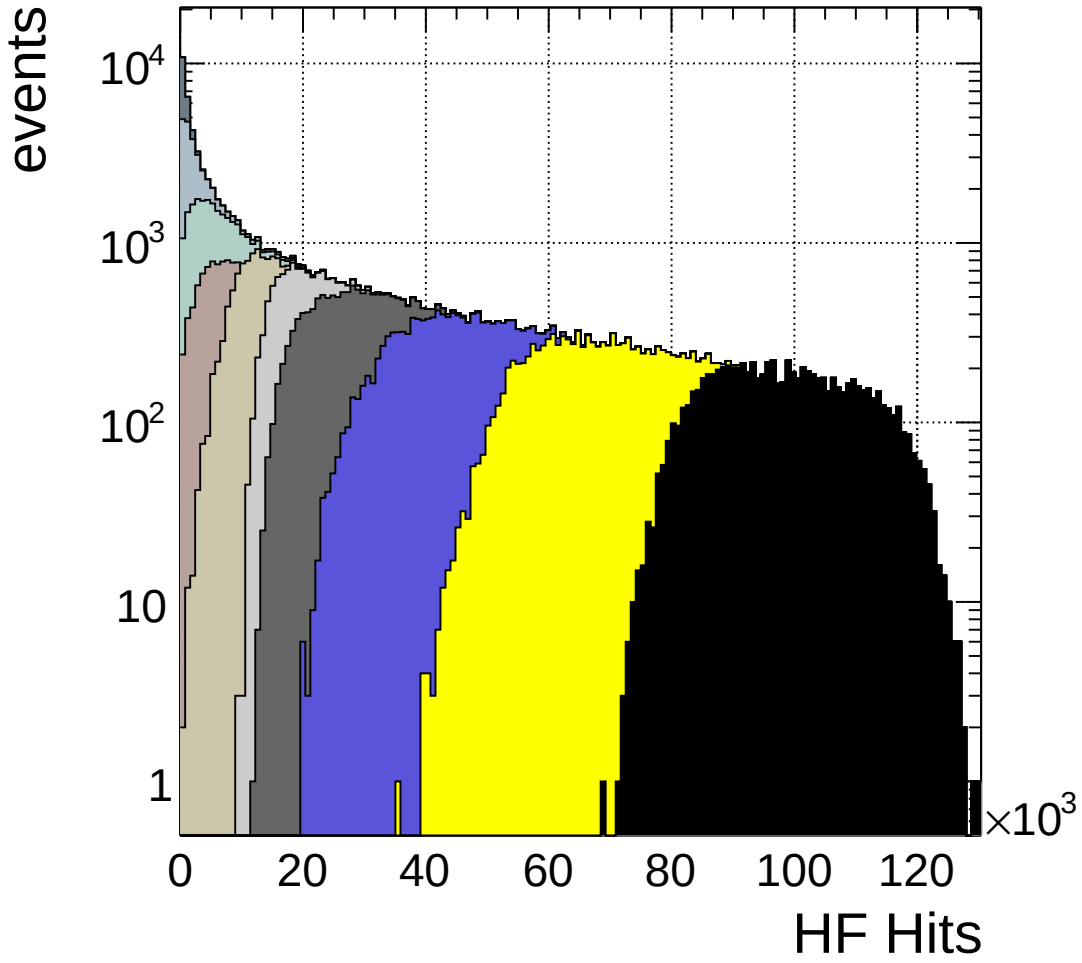

Figure 5.29: The HF signal color-coded by 10% wide regions of centrality derived from the ZDC vs. pixels banana is shown here. The events in each centrality bin are consistent with those in 10% grouping straight from Figure 5.27.

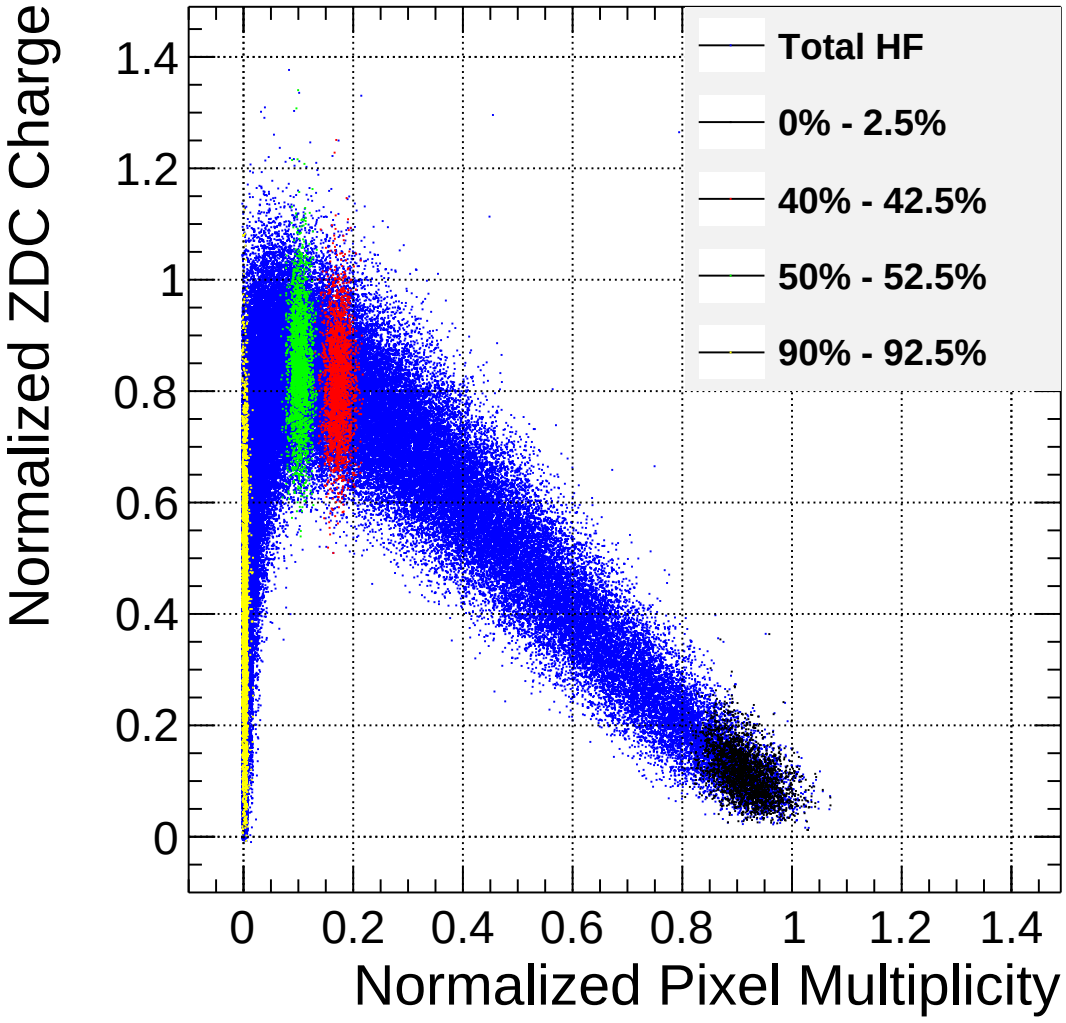

Figure 5.30: The banana plot with a few judicious choices of color-coded regions of centrality as defined by HF along with the HF distributions are shown here. This outlines that the derivation of centrality from ZDC versus pixels to the centrality as defined by HF becomes increasingly different for more peripheral collisions when comparing to Figure 5.27.

The reweighting of the HF distributions by centrality classes derived from ZDC versus pixels can naturally create an autocorrelation when HF signals are used in a given physics analysis. Therefore, it is also useful to derive the centrality with correlations in ZDC signals and HF transverse energy flow. Doing this allows a ZDC versus HF banana plot that can yield analogous centrality classes on a plot of pixel multiplicity. Clearly, events in each centrality class change in HF depending on the current and ZDC versus pixel derivation method. The events in each centrality class concordantly change in pixel multiplicity depending on whether the HF derived centrality or the ZDC versus HF transverse energy flow method is used. The exact same algorithm can be applied to the ZDC versus HF banana as that used in the ZDC versus pixels banana. As a matter of fact, because this algorithm normalizes the units in both ZDC charge and HF transverse energy flow, the profile fit function is exactly the same as it is in the ZDC versus pixel analysis. In other words, a ZDC versus HF transverse energy flow centrality derivation flips the assignments of HF transverse energy flow and pixel multiplicity everywhere from the ZDC versus pixel case.

A ZDC versus HF transverse energy flow analysis ultimately yields a resulting pixel multiplicity distribution that is analogous to the HF distributions given by the ZDC versus pixel analysis. The result is given by Figure 5.31.

It is not just the HF distributions of centrality classes that can derive N_{part}. A complimentary method for deriving N_{part} can be given by the analogous pixel multiplicity distributions of centrality classes. In this way, a ZDC vs HF analysis can avoid autocorrelations with HF where they appropriately occur, and N_{part} can still be derived by looking at the response of the pixel detector instead of HF. For comparison, however, Figure 5.32 shows the pixel distributions of the centrality classes derived by HF.

Figure 5.33 compares the ZDC versus HF results to the HF-alone results. The mean of each pixel distribution of a given centrality class from HF-alone results is subtracted from the mean of each ZDC versus HF result to show this difference. The difference is also applied to the RMS of the distributions in each centrality class. The pixel units are

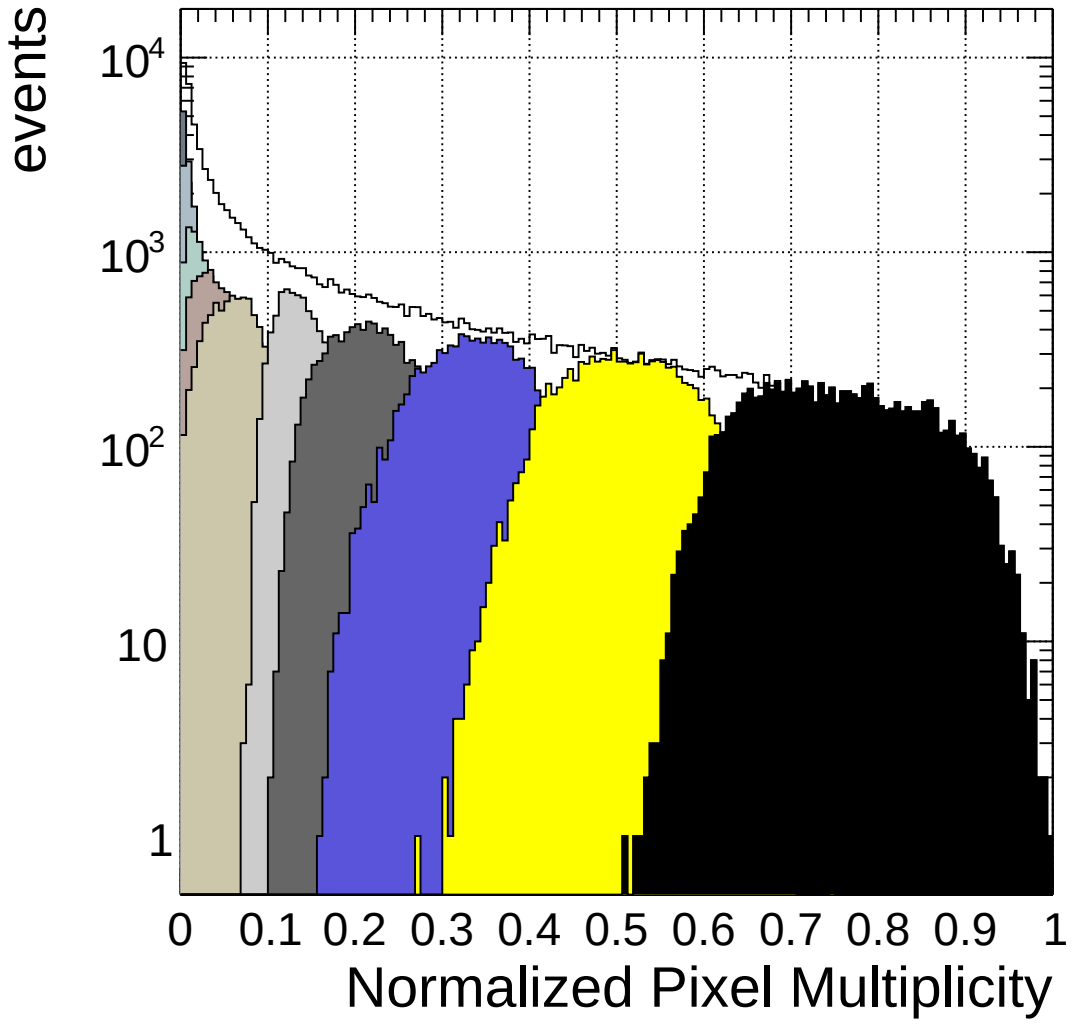

Figure 5.31: This shows the pixel distributions of 10% centrality classes from the ZDC versus HF analysis. These 10% distributions are different from the ones derived from HF centrality alone.

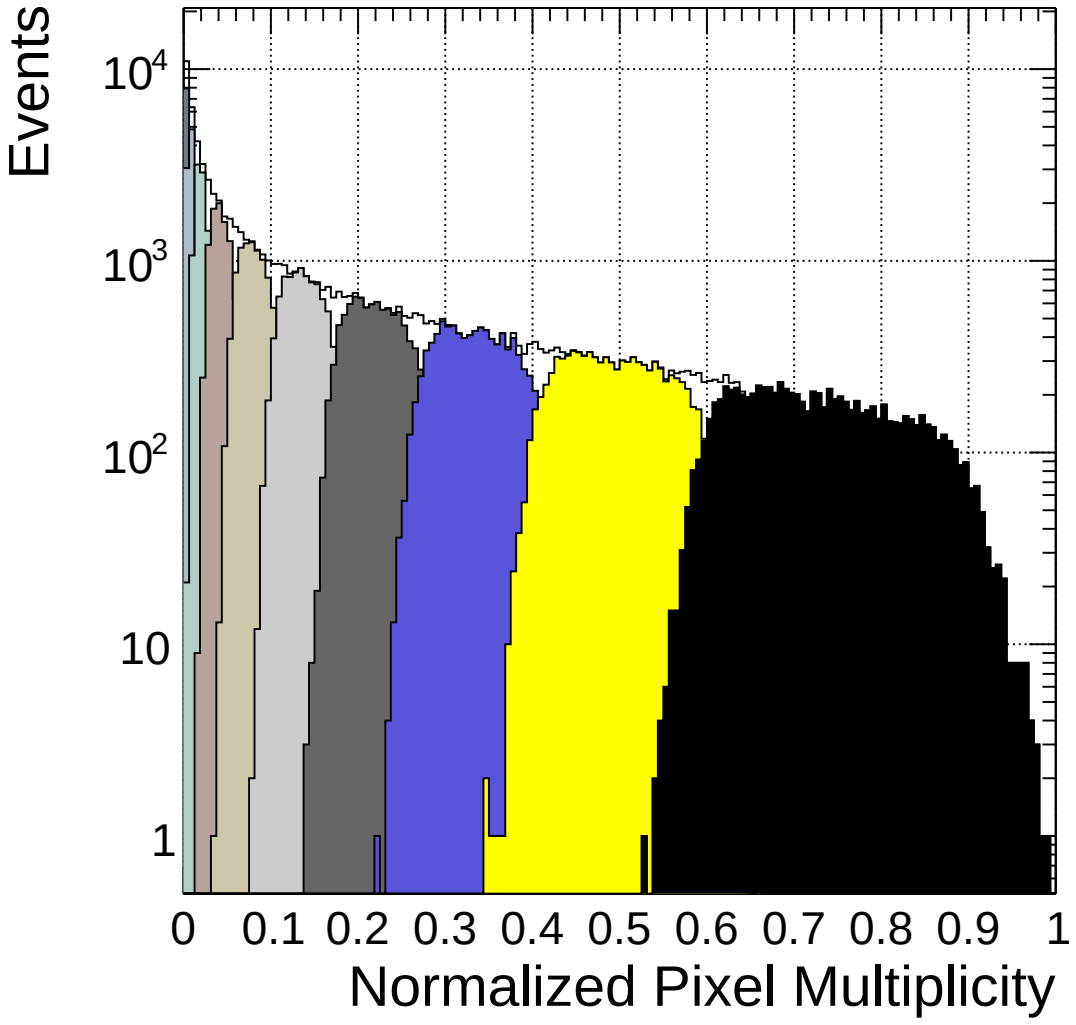

Figure 5.32: This shows the pixel distributions of 10% centrality classes from the HF derived centrality.

normalized in both cases, and the differences are clear. They do not, however scale by increasing difference for more peripheral collisions like in the analogous HF distributions. The differences are much more uncorrelated. The pixel detector, of course, has much more transverse angular coverage than HF, and this might account for the differences.

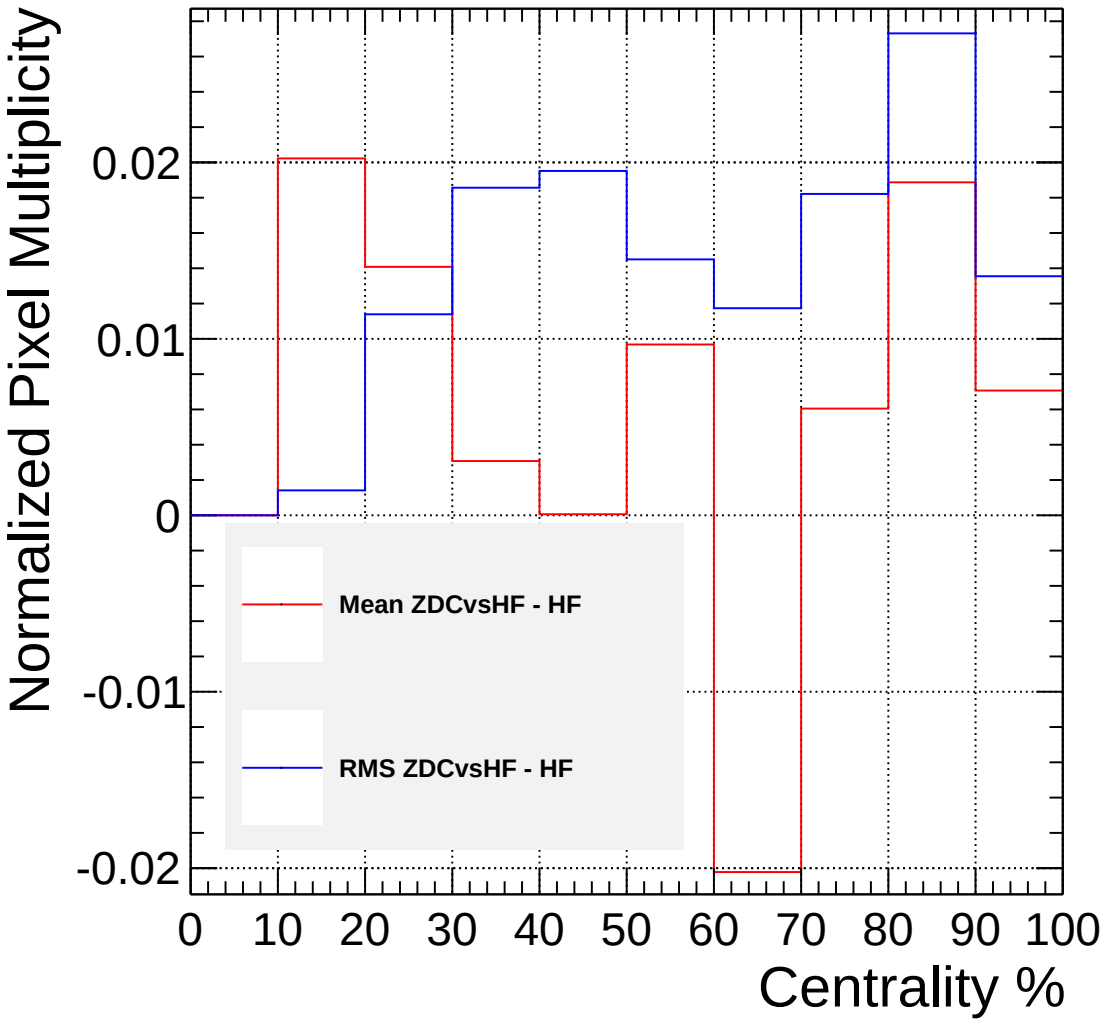

Figure 5.33: This shows the difference in the mean and RMS of pixel distributions of 10% centrality classes from ZDC versus HF to HF derived centrality. This is meant to illustrate that deriving centrality with ZDC versus HF will yield different $< N_{part} >$ than the HF derivation.

Chapter 6

ZDC Neutron Spectrum

"Discussing ZDC spectra is somewhat neutral territory..."

There was a mildly stronger fluctuation on the plus side ZDC signals than for the minus side. For brevity, it is worth showing the plot of these fluctuations again in this section in Figure 6.1. It is useful to process the signal in one more extra step using the ZDC spectator neutron spectrum to effectively gain-match the two sides of the ZDC detector.

To gain-match the two ZDCs, a method of singling out spectator neutrons is needed. It was found that the spectator neutrons are greatly constrained to peripheral collisions without the need of a series of convoluted Landau distributions. Instead, in peripheral collisions, spectator neutron peaks are observed one at a time. Again, peripheral collisions are localized to low pixel multiplicity. The fact that there is a dependence to deconvoluted spectator neutron signal to low pixel multiplicity is the reason why spectator signal is analyzed after the centrality analysis. A plot of a ZDC minus side spectator neutron spectrum is given in Figure 6.3 and for the plus side in Figure 6.2. To single out the spectator neutrons, a cut on the banana plot for small window of pixel signal is made. This cut includes all of the ZDC signal from $0 < PIX < 0.025$, where PIX is in normalized pixel units. This cut is used instead of a centrality range cut in

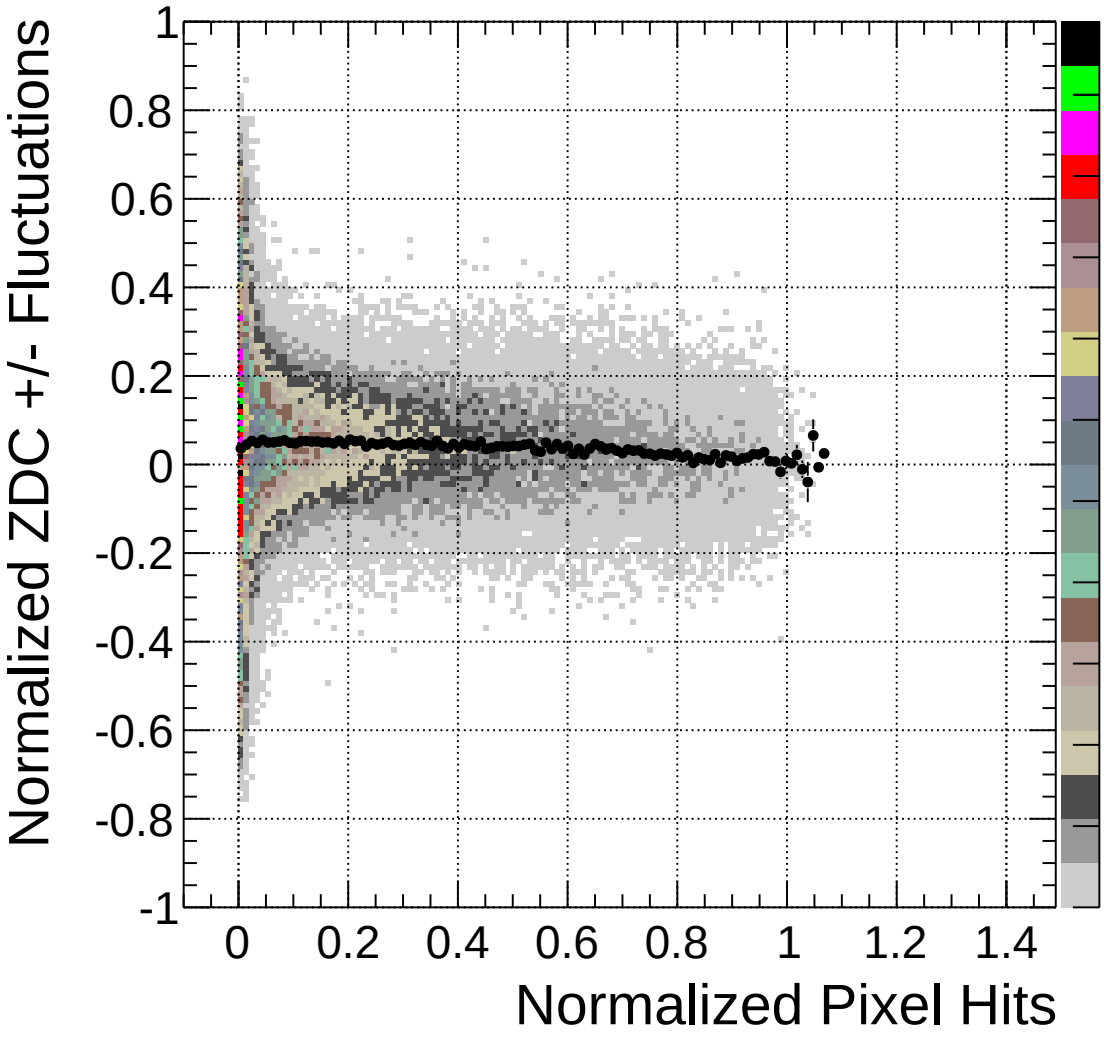

Figure 6.1: A plot of the difference of the plus and minus side signal in the ZDC divided by the square root of their sum versus pixel signal is shown here again. There is a slightly greater signal evident in the ZDC average, in black, from the ZDC plus side as fluctuations climb.

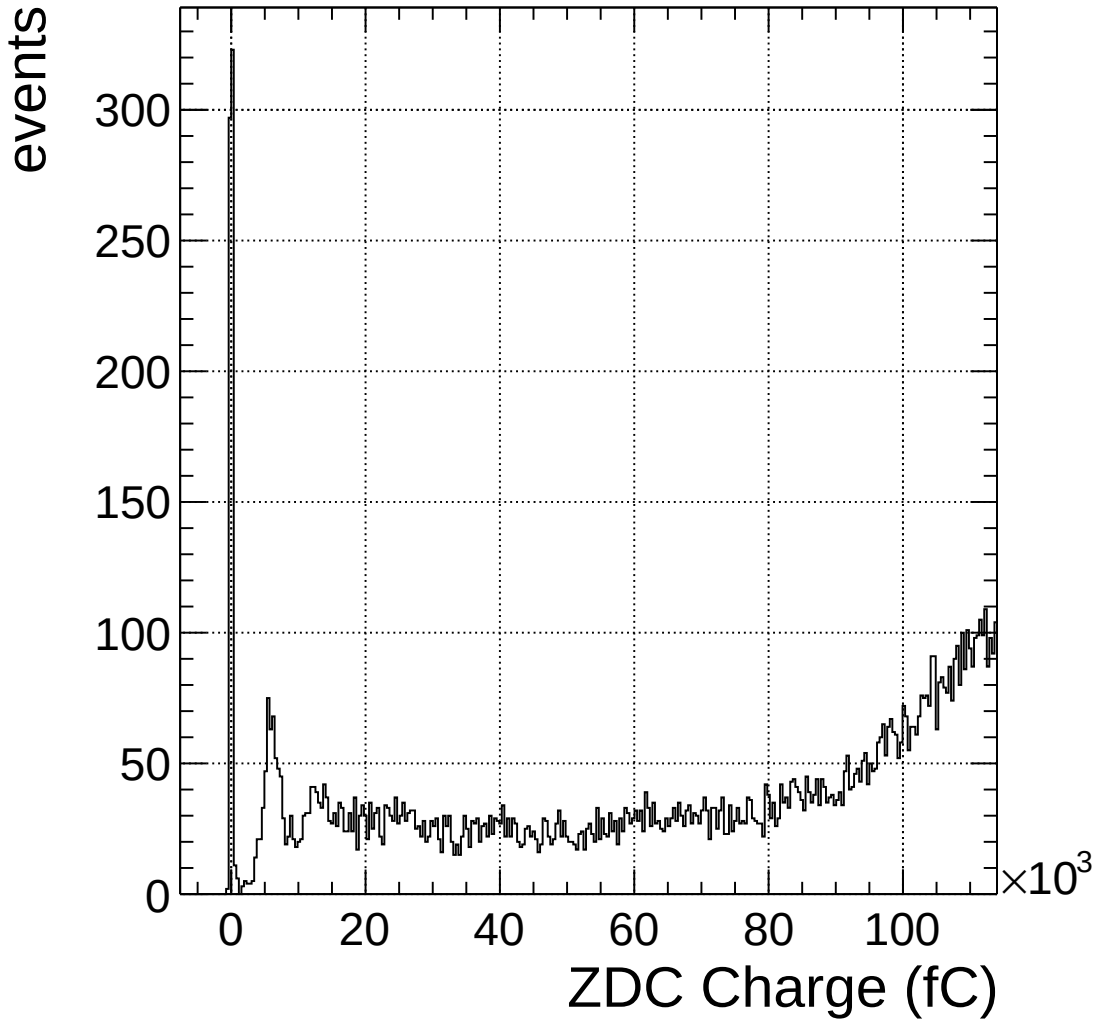

Figure 6.2: A plot of the spectator neutron spectrum for the ZDC plus side at low pixel multiplicity is shown here. The neutron peaks are deconvolved. Each peak corresponds to integrally increasing numbers of spectator neutrons.

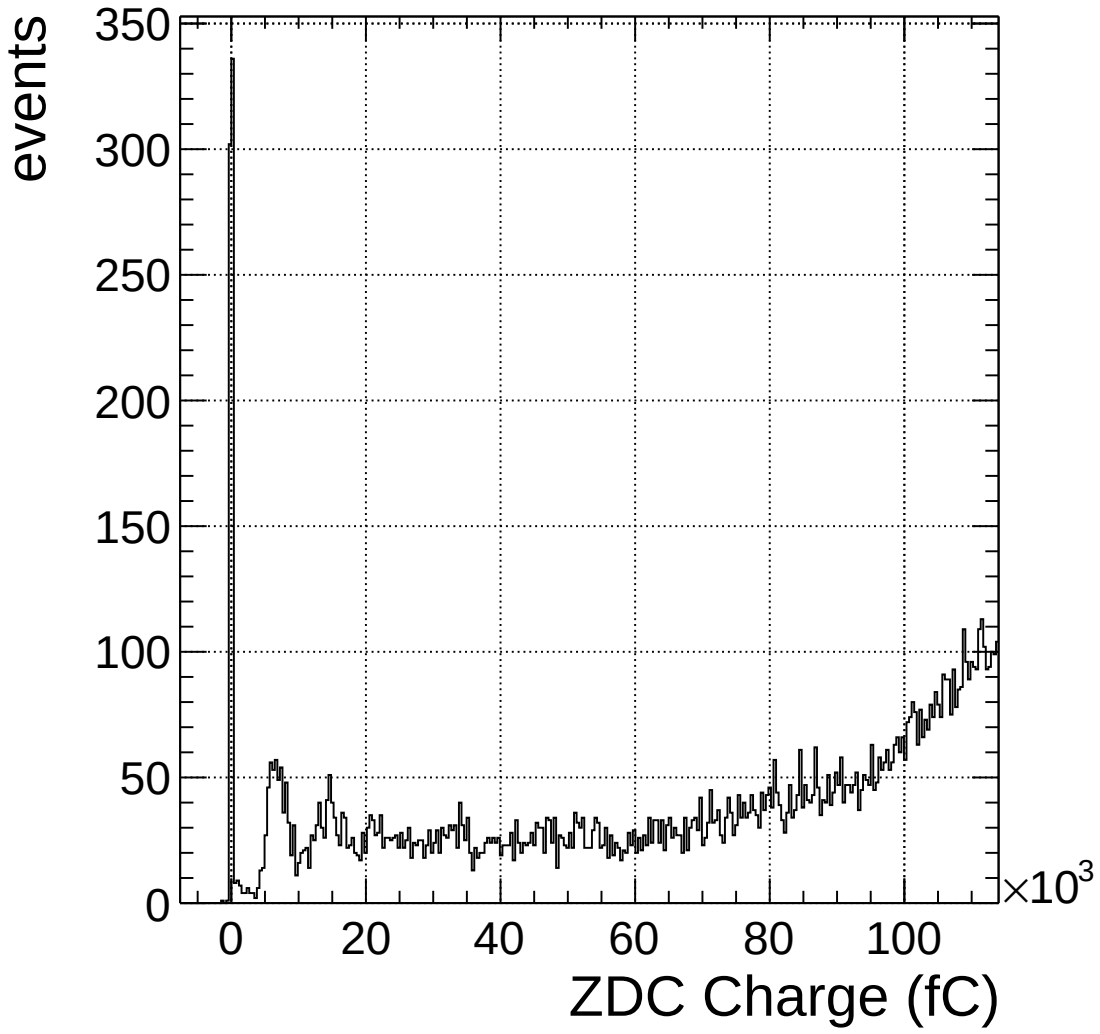

Figure 6.3: A plot of the spectator neutron spectrum for the ZDC minus side at low pixel multiplicity is shown here. The neutron peaks are deconvolved. Each peak corresponds to integrally increasing numbers of spectator neutrons.

peripheral collisions because of the random nature of multifragmentation. Because it is random, a more central centrality bin might contain the same amount of spectator neutrons as even the most peripheral bin. In order to capture as much signal from the ZDCs to reveal the first two neutron peaks, a global pixel range cut is used instead of the centrality information. The data is plotted from adding signal from timeslices five, six, and seven instead of from adding from six, seven, and eight. This is because the signal is not digitally saturated for low numbers of spectator neutrons per event, as the first two peaks are only one and two neutrons per event.

Table 6.1: Neutron Peak Fits for ZDC Plus

Neutron energy (GeV)	Mode of Charge (fC)	Sigma of Charge (fC)
1380	6490 ± 100	950 ± 80
2760	14700 ± 280	1900 ± 240

Table 6.2: Neutron Peak Fits for ZDC Minus

Neutron energy (GeV)	Mode of Charge (fC)	Sigma of Charge (fC)
1380	5930 ± 100	990 ± 80
2760	13600 ± 340	2300 ± 350

The gain matching of both sides of the ZDC begins with fitting each peak with its corresponding Landau distribution. The two parameters applicable here are the mode of the Landau distribution, and the sigma value, which is the statistical spread. The results of these fits is summarized in Tables 6.2 and 6.1. A graphical representation of these fits is given in Figure 6.6 for the first minus side peak, Figure 6.7 for the second minus side peak, Figure 6.4 for the first plus side peak, and Figure 6.5 for the second plus side peak.

Gain matching was performed by lining up the first neutron peak in each side of the ZDC. This is done by applying an appropriate factor of 12/13 to the plus side signal. When this is done not only does the first neutron peak line up for both sides of the ZDC, but the second one does also within less than 1% shift in peak charge. A result of these aligned peaks is given in Figure 6.8. A check of this gain matched ZDC signal is

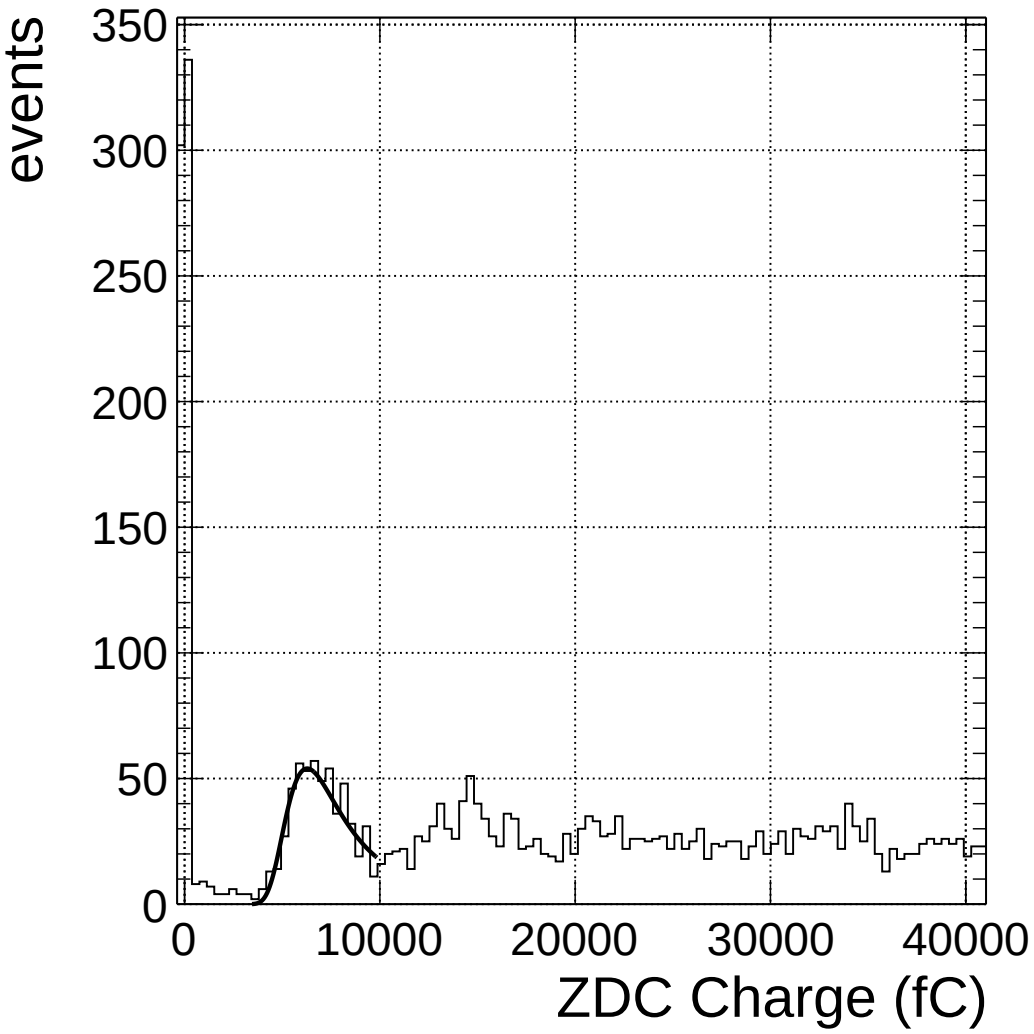

Figure 6.4: A plot of the Landau fit of the first spectator neutron peak for the ZDC plus side is shown here.

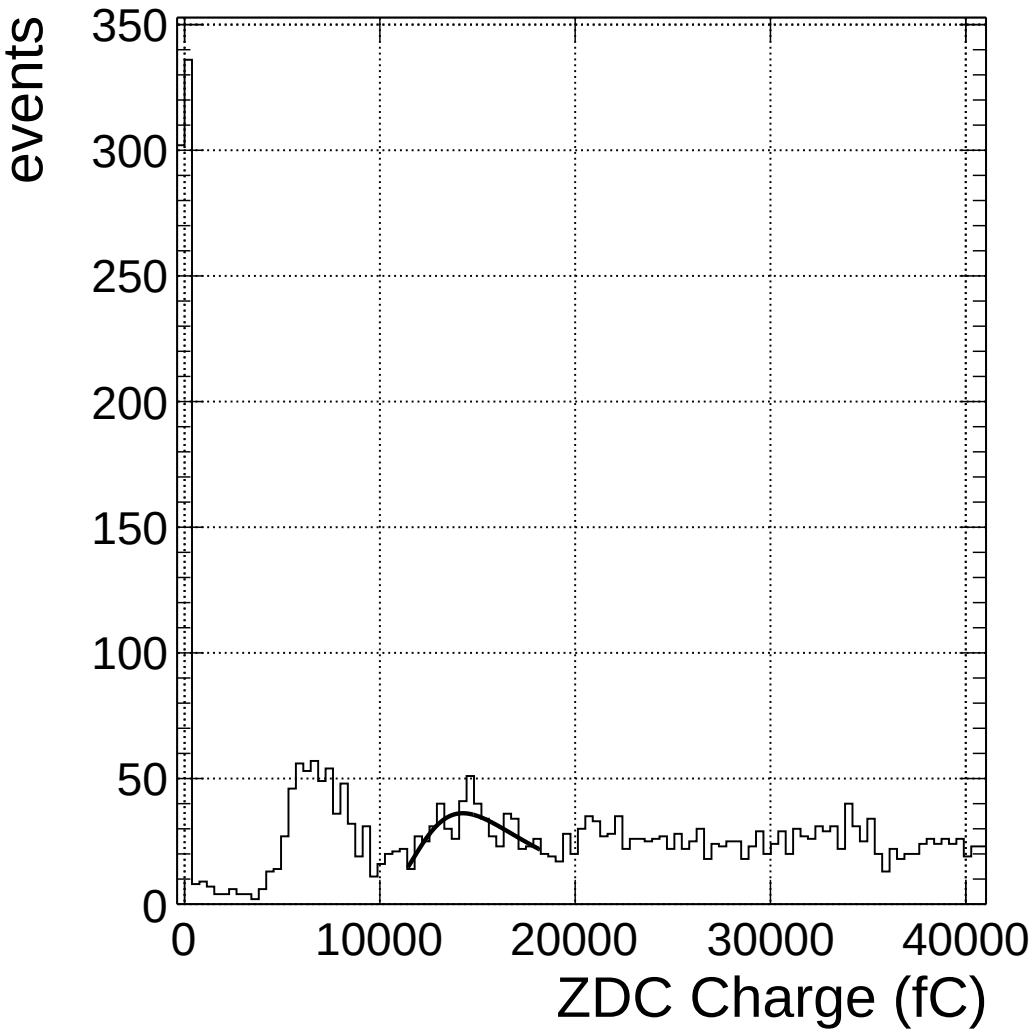

Figure 6.5: A plot of the Landau fit of the second spectator neutron peak for the ZDC plus side is shown here.

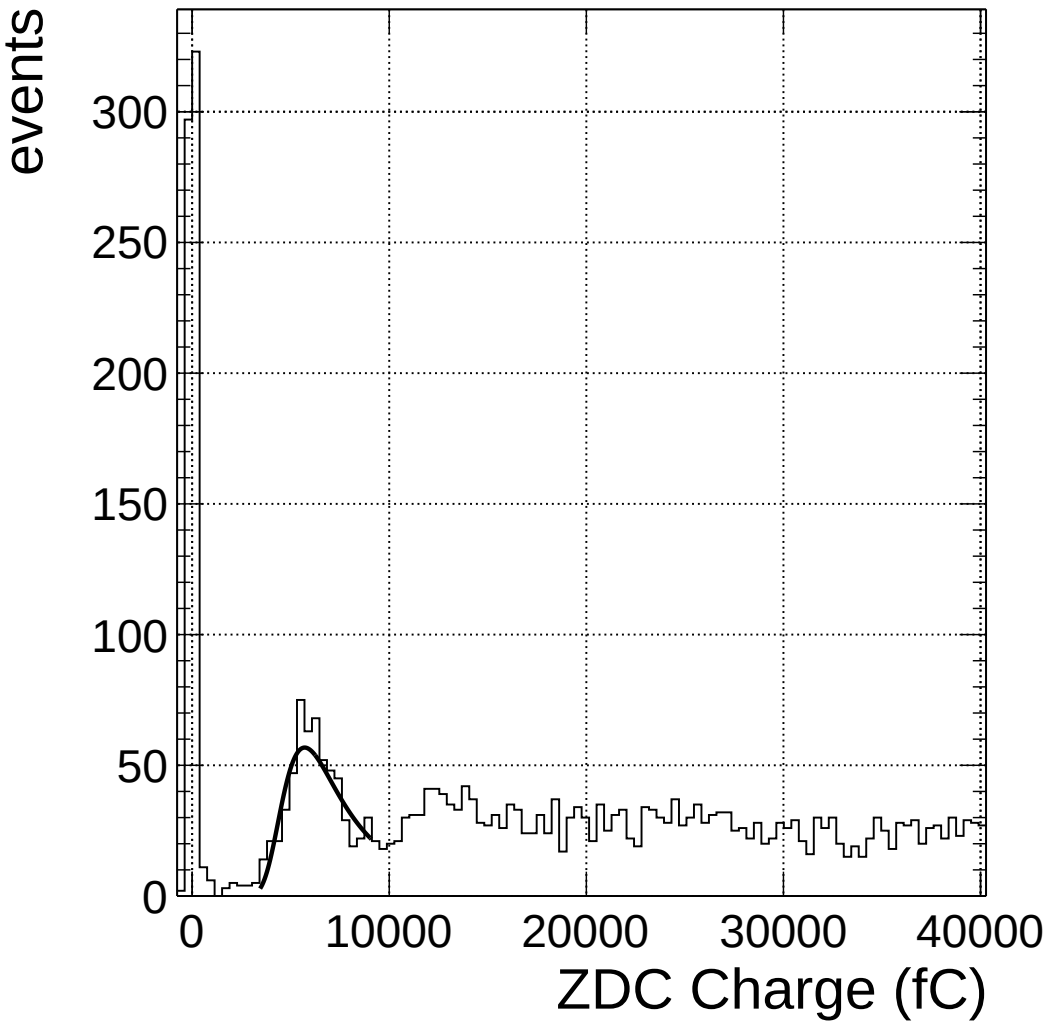

Figure 6.6: A plot of the Landau fit of the first spectator neutron peak for the ZDC minus side is shown here.

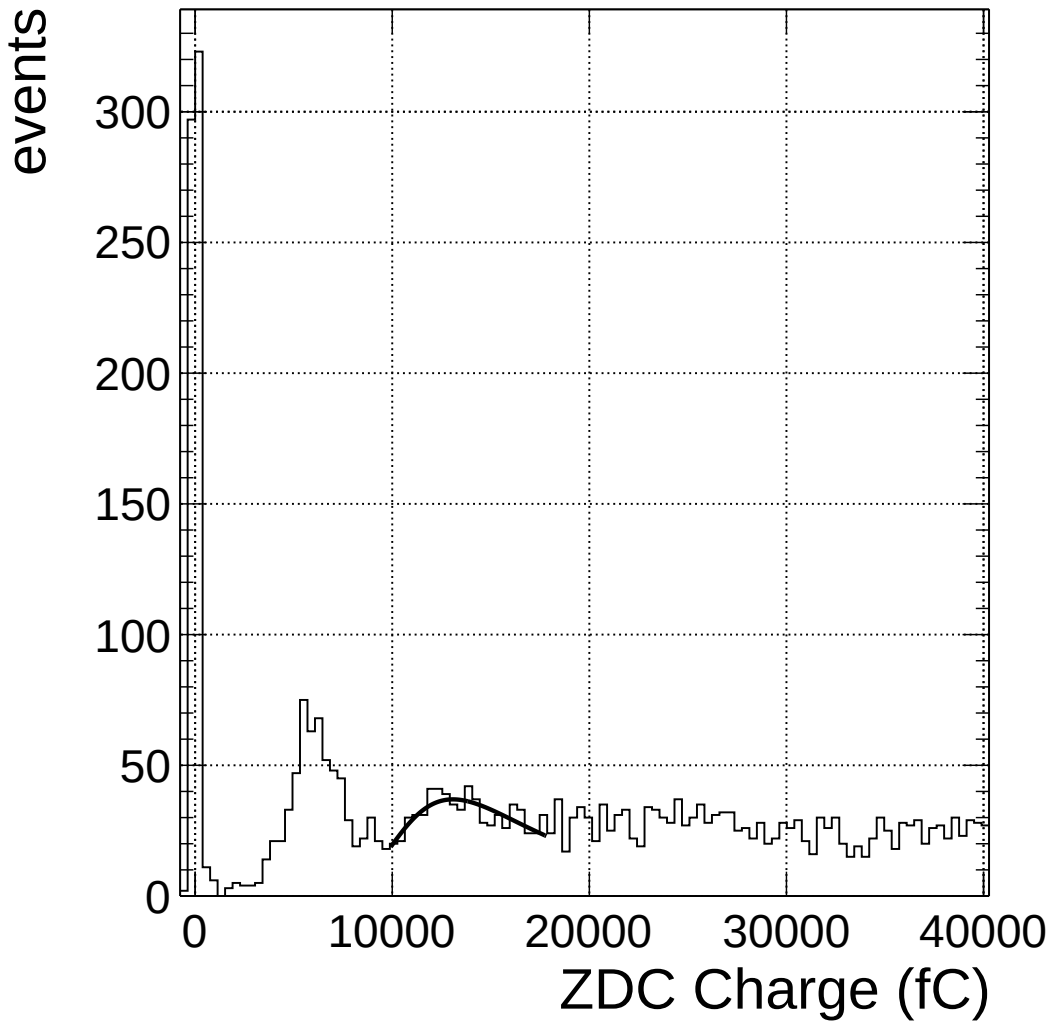

Figure 6.7: A plot of the Landau fit of the second spectator neutron peak for the ZDC minus side is shown here.

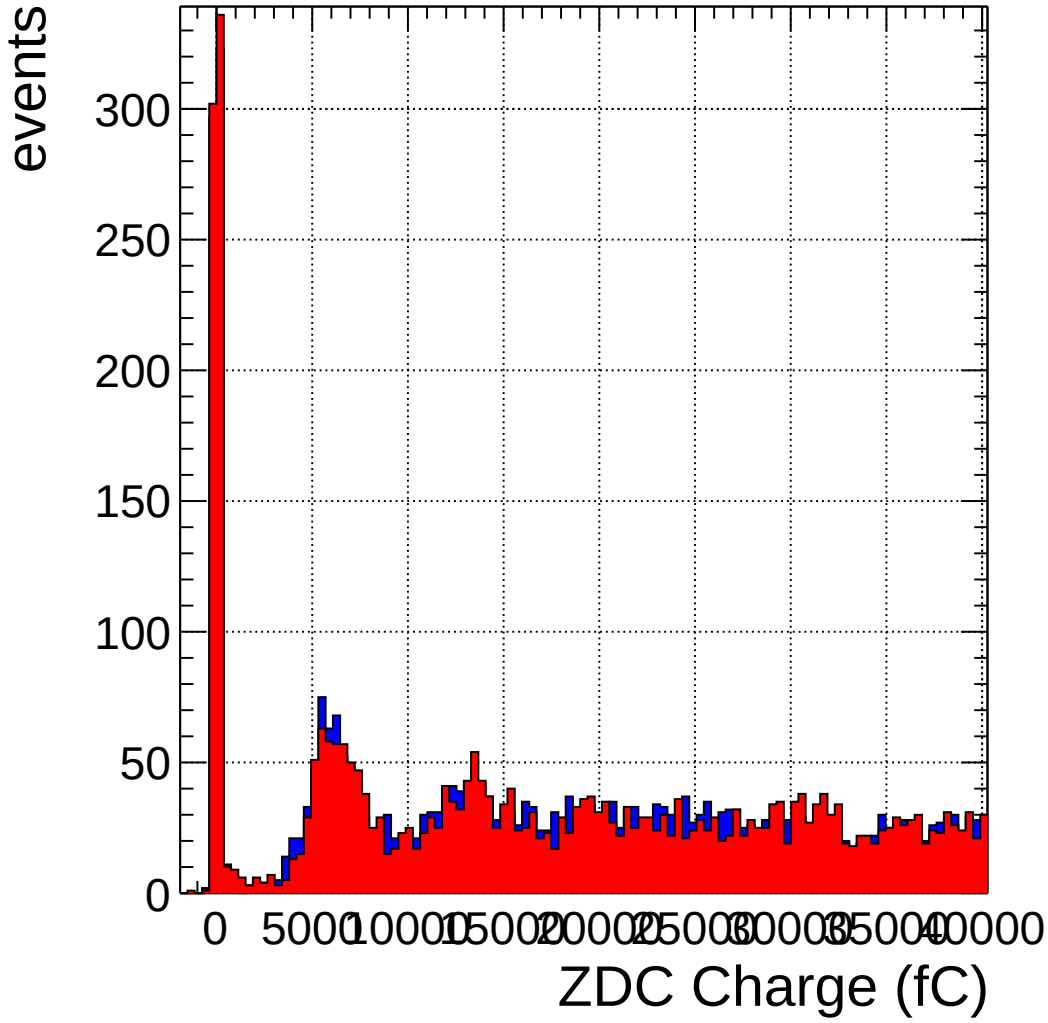

Figure 6.8: A plot of the gain matched neutron peaks is shown here. The plus side is given in red and the minus side in blue.

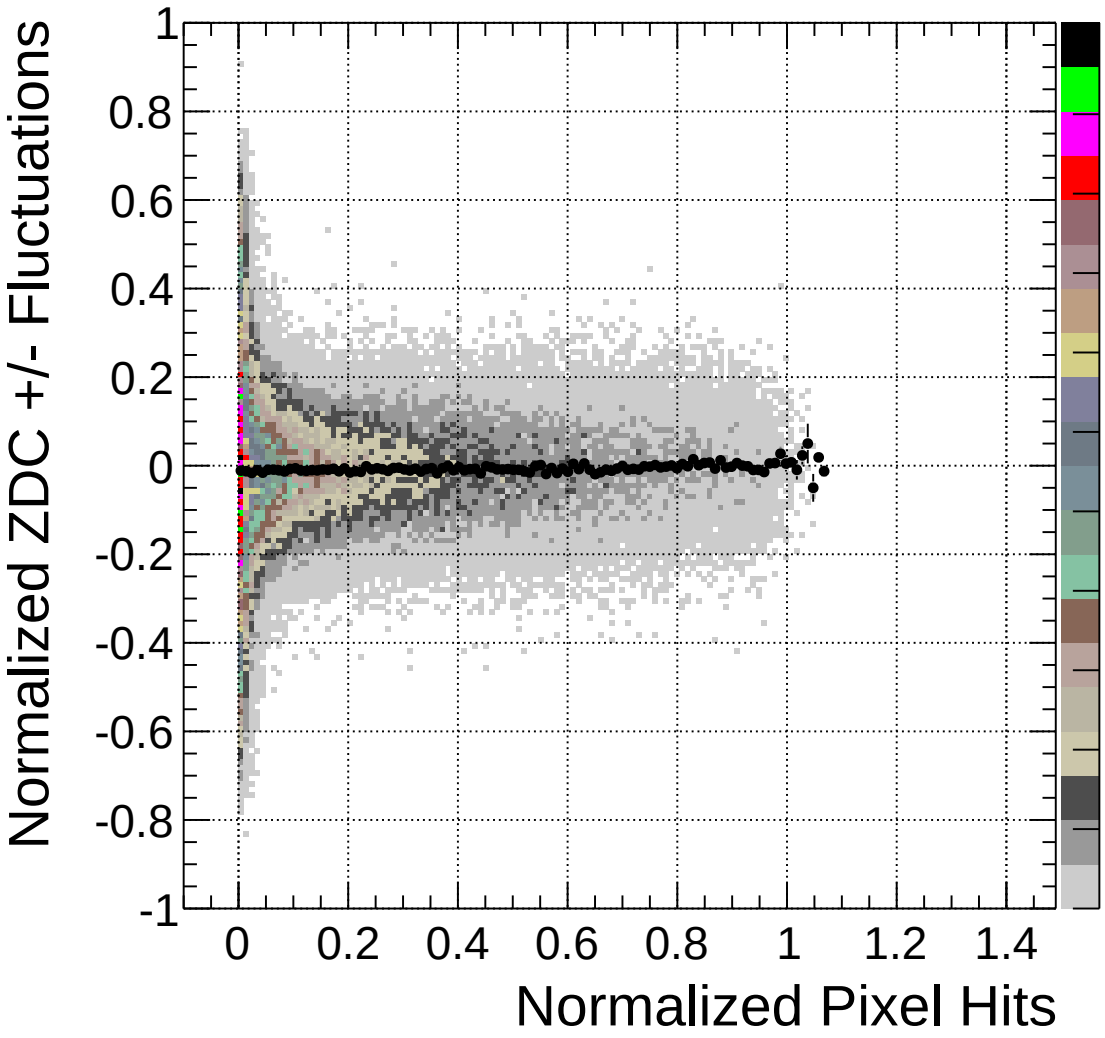

Figure 6.9: A plot of the difference of the plus and minus side signal in the ZDC divided by the square root of their sum versus pixel signal is shown here again. This time, the plus and minus side signals are gain matched, and the tendency of fluctations to be stronger on the ZDC plus side has been removed.

done by plotting the fluctuations again between ZDC plus and minus side signals with the weighting of 12/13 strength of the plus side. This is displayed in Figure 6.9.

Because of the system of units chosen on the banana plot, this gain matching correction actually does not change the parameterization of the profile. This is important, since the success of the centrality analysis hinges upon the profile parameterization. The maximum shift in the strength of the ZDC signal changes by a factor of 25/26, which is about 3.8%. This is inconsequential, however, because the ZDC units are normalized to a maximum value of 1 to keep the anticorrelation between ZDC and pixels in central collisions. The profile parameterization is still in terms of these normalized units, and they cannot depend on the gain of the detectors.

Chapter 7

Conclusion

"Forward spectator measurement is a step forward for centrality..."

A consistent, and generalized scheme is used to generate centralities up to 90% in 2.5% bins. Previous generation collider experiments do not come close to this by cutting off at about 60%, where the anticorrelation between forward spectators and low pseudorapidity particles breaks down. This analysis solves the difficulties that arise when this happens. Even after 90% centrality, the rest of the forward spectators are still counted to complete the centrality derivation.

Results show that there is a strong anticorrelation between forward spectators and high transverse momentum charged particles in central Pb Pb collisions. This is exploited to derive the centrality, and the centrality derived from the HF detector matches these results in central collisions. Multifragmentation and coalescence randomly remove some forward spectators from zero degrees, and this causes the anticorrelation to break down for peripheral collisions. Therefore, the anticorrelation alone is not enough to find and utilize a single parameter that scales with the centrality. However, averaging over the sample of the ZDC signal results in a parameter, the arclength of the profile of the ZDC versus pixels banana plot, that scales with the centrality for peripheral collisions up to 90% centrality. This is the same parameter used in the central collision analy-

sis. Studies show that event selection by centrality is different between the results of an analysis using HF and the ZDC versus pixel analysis in peripheral collisions, where multifragmentation and coalescence both become significant.

The centrality derived from the ZDC versus pixel analysis results in a ZDC versus HF energy banana plot where event selection is similar between the two. The ZDC versus HF energy banana plot smears the centrality boundaries of their sharp counterparts in the ZDC versus pixels banana plot. For central collisions, the anticorrelation present between the ZDC signals and HF energy is still as strong as it is between the ZDC signals and pixel multiplicity. This offers a good "sanity check" for extrapolation of the centrality derivation in this analysis to peripheral collisions. For peripheral collisions, the centrality boundaries are shifted. So there is a trend to shift centrality boundaries more when collisions are more peripheral in a ZDC versus pixel analysis.

The centrality can also be derived from a ZDC charge versus HF E_T banana plot, where the assignments of HF data and pixel data are swapped from what they are in the ZDC versus pixel analysis. The scheme is exactly the same as the ZDC versus pixel analysis, but the results of the centrality class boundaries changes behavior. There is still a shift in centrality class boundaries from the HF derived centrality, but the shift is uncorrelated everywhere. This supplimental banana plot analysis is useful if autocorrelations with HF data need to be avoided if a step further is taken to deriving an N_{part}. However, the price of using the ZDC versus HF analysis seems to be that no correlation can be found in the shift of centrality boundaries from the HF derived centrality when observing the pixel distribution, even if N_{part} changes.

Bibliography

[1] H. Fritzsch, Murray Gell-Mann, and H. Leutwyler. "Advantages of the Color Octet Gluon Picture". In: *Phys.Lett.* B47 (1973), pp. 365–368. DOI: 10.1016/0370-2693(73)90625-4.

[2] D.J. Gross and Frank Wilczek. "Asymptotically Free Gauge Theories. 1". In: *Phys.Rev.* D8 (1973), pp. 3633–3652. DOI: 10.1103/PhysRevD.8.3633.

[3] D.J. Gross and Frank Wilczek. "ASYMPTOTICALLY FREE GAUGE THEORIES. 2." In: *Phys.Rev.* D9 (1974), pp. 980–993. DOI: 10.1103/PhysRevD.9.980.

[4] D.J. Gross and Frank Wilczek. "Ultraviolet Behavior of Nonabelian Gauge Theories". In: *Phys.Rev.Lett.* 30 (1973), pp. 1343–1346. DOI: 10.1103/PhysRevLett.30.1343.

[5] H. David Politzer. "Reliable Perturbative Results for Strong Interactions?" In: *Phys.Rev.Lett.* 30 (1973), pp. 1346–1349. DOI: 10.1103/PhysRevLett.30.1346.

[6] Frank Wilczek. "QCD made simple". In: *Phys.Today* 53N8 (2000), pp. 22–28.

[7] V.E. Barnes et al. "Observation of a Hyperon with Strangeness -3". In: *Phys.Rev.Lett.* 12 (1964), pp. 204–206. DOI: 10.1103/PhysRevLett.12.204.

[8] Siegfried Bethke. "The 2009 World Average of alpha(s)". In: *Eur.Phys.J.* C64 (2009), pp. 689–703. DOI: 10.1140/epjc/s10052-009-1173-1. eprint: 0908.1135.

[9] Roger D. Woods and David S. Saxon. "Diffuse Surface Optical Model for Nucleon-Nuclei Scattering". In: *Phys.Rev.* 95 (1954), pp. 577–578. DOI: 10.1103/PhysRev.95.577.

[10] Robert Hofstadter. "Electron scattering and nuclear structure". In: *Rev.Mod.Phys.* 28 (1956), pp. 214–254. DOI: 10.1103/RevModPhys.28.214.

[11] Roy J. Glauber. "Quantum Optics and Heavy Ion Physics". In: *Nucl.Phys.* A774 (2006), pp. 3–13. DOI: 10.1016/j.nuclphysa.2006.06.009. eprint: nucl-th/0604021.

[12] A. Bialas, M. Bleszynski, and W. Czyz. "Relation Between the Glauber Model and Classical Probability Calculus". In: *Acta Phys.Polon.* B8 (1977), pp. 389–392.

[13] R.J. Glauber. "Deuteron Stripping Processes at High Energies". In: *Phys.Rev.* 99 (1955), pp. 1515–1516. DOI: 10.1103/PhysRev.99.1515.

[14] Constantin Loizides. "Collective behavior in heavy-ion collisions". In: *AIP Conf.Proc.* 1441 (2012), pp. 79–86. DOI: 10.1063/1.3700484.

[15] G. Aad et al. "Measurement of the centrality dependence of J/Ψ yields and observation of Z production in lead-lead collisions with the ATLAS detector at the LHC". In: *Phys.Lett.* B697 (2011), pp. 294–312. DOI: 10.1016/j.physletb.2011.02.006. eprint: 1012.5419.

[16] Serguei Chatrchyan et al. "Observation of sequential Upsilon suppression in PbPb collisions". In: (2012). eprint: 1208.2826.

[17] Dong Ho Moon. "Measurement of charmonium production in PbPb collisions at 2.76 TeV with CMS". In: (2012). eprint: 1209.1084.

[18] P. Pillot. "J/Ψ production at forward rapidity in Pb-Pb collisions at $\sqrt{s_{NN}} = 2.76$ TeV, measured with the ALICE detector". In: *J.Phys.* G38 (2011), p. 124111. DOI: 10.1088/0954-3899/38/12/124111. eprint: 1108.3795.

[19] Serguei Chatrchyan et al. "Measurement of the elliptic anisotropy of charged particles produced in PbPb collisions at nucleon-nucleon center-of-mass energy = 2.76 TeV". In: *Phys.Rev.* C87 (2013), p. 014902. DOI: 10.1103/PhysRevC.87.014902. eprint: 1204.1409.

[20] Jiangyong Jia. "Measurement of elliptic and higher order flow from ATLAS experiment at the LHC". In: *J.Phys.* G38 (2011), p. 124012. DOI: 10.1088/0954-3899/38/12/124012. eprint: 1107.1468.

[21] Ilya Selyuzhenkov. "Anisotropic flow and other collective phenomena measured in Pb-Pb collisions with ALICE at the LHC". In: *Prog.Theor.Phys.Suppl.* 193 (2012), pp. 153–158. DOI: 10.1143/PTPS.193.153. eprint: 1111.1875.

[22] Huichao Song et al. "200 A GeV Au+Au collisions serve a nearly perfect quark-gluon liquid". In: *Phys.Rev.Lett.* 106 (2011), p. 192301. DOI: 10.1103/PhysRevLett.106.192301. eprint: 1011.2783.

[23] James L. Nagle, Ian G. Bearden, and William A. Zajc. "Quark-Gluon Plasma at RHIC and the LHC: Perfect Fluid too Perfect?" In: *New J.Phys.* 13 (2011), p. 075004. DOI: 10.1088/1367-2630/13/7/075004. eprint: 1102.0680.

[24] Carlos A. Salgado. "Hard Probes of the Quark Gluon Plasma in Heavy Ion Collisions". In: *AIP Conf.Proc.* 1441 (2012), pp. 87–94. DOI: 10.1063/1.3700485. eprint: 1109.4082.

[25] B.G. Zakharov. "Variation of jet quenching from RHIC to LHC and thermal suppression of QCD coupling constant". In: *JETP Lett.* 93 (2011), pp. 683–687. DOI: 10.1134/S0021364011120162. eprint: 1105.2028.

[26] Saeid Paktinat Mehdiabadi. "Studies of jet quenching in PbPb collisions at s(NN)**(1/2) = 2.76-TeV". In: *AIP Conf.Proc.* 1422 (2012), pp. 203–208. DOI: 10.1063/1.3692218.

[27] Jan Fiete Grosse-Oetringhaus. "Measurement of jet quenching with I_{CP} and I_{AA},Pythia in Pb-Pb collisions at $\sqrt{s_{NN}} = 2.76$ TeV with ALICE". In: (2011). eprint: 1105.3901.

[28] Martin Rybar. "Measurements of jets and jet properties in $\sqrt{s_{NN}} = 2.76$ TeV lead-lead collisions with the ATLAS detector at the LHC". In: (2012). eprint: 1208.6504.

[29] Jan Fiete Grosse-Oetringhaus. "In-Medium Energy Loss and Correlations in Pb-Pb Collisions at $\sqrt{s_{NN}} = 2.76$ TeV". In: *AIP Conf.Proc.* 1422 (2012), pp. 209–215. DOI: 10.1063/1.3692219. eprint: 1109.6208.

[30] Serguei Chatrchyan et al. "Dependence on pseudorapidity and centrality of charged hadron production in PbPb collisions at a nucleon-nucleon centre-of-mass energy of 2.76 TeV". In: *JHEP* 1108 (2011), p. 141. DOI: 10.1007/JHEP08(2011)141. eprint: 1107.4800.

[31] S. Afanasev et al. "The NA49 large acceptance hadron detector". In: *Nucl.Instrum.Meth.* A430 (1999), pp. 210–244. DOI: 10.1016/S0168-9002(99)00239-9.

[32] Clemens Adler et al. "The RHIC zero degree calorimeter". In: *Nucl.Instrum.Meth.* A470 (2001), pp. 488–499. DOI: 10.1016/S0168-9002(01)00627-1. eprint: nucl-ex/0008005.

[33] Michael L. Miller et al. "Glauber modeling in high energy nuclear collisions". In: *Ann.Rev.Nucl.Part.Sci.* 57 (2007), pp. 205–243. DOI: 10.1146/annurev.nucl.57.090506.123020. eprint: nucl-ex/0701025.

[34] A. Denisov. "Common event characterization in the RHIC experiments". In: *Nucl.Phys.* A698 (2002), pp. 551–554. DOI: 10.1016/S0375-9474(01)01426-9.

[35] Lyndon Evans and Philip Bryant. "LHC Machine". Ed. by Lyndon Evans. In: *JINST* 3 (2008), S08001. DOI: 10.1088/1748-0221/3/08/S08001.

[36] G. Aad et al. “The ATLAS Experiment at the CERN Large Hadron Collider”. In: *JINST* 3 (2008), S08003. DOI: 10.1088/1748-0221/3/08/S08003.

[37] K. Aamodt et al. “The ALICE experiment at the CERN LHC”. In: *JINST* 3 (2008), S08002. DOI: 10.1088/1748-0221/3/08/S08002.

[38] Jr. Alves A. Augusto et al. “The LHCb Detector at the LHC”. In: *JINST* 3 (2008), S08005. DOI: 10.1088/1748-0221/3/08/S08005.

[39] G.L. Bayatian et al. “CMS physics: Technical Design Report”. In: (2006).

[40] N. Angert et al. “A HEAVY ION INJECTOR FOR THE CERN LINAC-I”. In: *Nucl.Instrum.Meth.* A258 (1987), p. 1. DOI: 10.1016/0168-9002(87)90074-X.

[41] *CERN Proton Synchrotron Specifications*. http://home.web.cern.ch/about/accelerators/proton-synchrotron. Accessed: 2010-09-30.

[42] *CERN SPS Specifications*. http://home.web.cern.ch/about/accelerators/super-proton-synchrotron. Accessed: 2010-09-30.

[43] *CMS HCAL TDR*. http://www.uscms.org/uscms_at_work/dmo/hcal/hcal_tdr.html. Accessed: 2010-09-30.

[44] *CMS Tracker TDR*. http://cmsdoc.cern.ch/cms/TDR/TRACKER/tracker.html. Accessed: 2010-09-30.

[45] O.A. Grachov et al. “Performance of the combined zero degree calorimeter for CMS”. In: *J.Phys.Conf.Ser.* 160 (2009), p. 012059. eprint: 0807.0785.

[46] Guenter Grindhammer, M. Rudowicz, and S. Peters. “THE FAST SIMULATION OF ELECTROMAGNETIC AND HADRONIC SHOWERS”. In: *Nucl.Instrum.Meth.* A290 (1990), p. 469. DOI: 10.1016/0168-9002(90)90566-0.

[47] R. Wigmans. “Sampling calorimetry”. In: *Nucl.Instrum.Meth.* A494 (2002), pp. 277–287. DOI: 10.1016/S0168-9002(02)01481-X.

[48] *Hamamatzu R7525 Photomultiplier Tube Specification*. http://doc.chipfind.ru/hamamatsu/r7525.htm. Accessed: 2010-09-30.

[49] *CMS Zero Degree Calorimeter TDR*. https://twiki.cern.ch/twiki/bin/viewauth/CMS/ZDCWikiHome. Accessed: 2010-09-30.

[50] *PolyMicro High-OH Silica/Silica Optical Fiber Specification*. http://www.molex.com/molex/products/family?key=polymicro_optical_fibers&channel=products&chanName=family&pageTitle=Introduction&parentKey=polymicro",

[51] O. Grachov et al. "Commissioning of the CMS zero degree calorimeter using LHC beam". In: *J.Phys.Conf.Ser.* 293 (2011), p. 012040. eprint: 1008.1157.

[52] Oleg A. Grachov et al. "Measuring photons and neutrons at zero degrees in CMS". In: *Int.J.Mod.Phys.* E16 (2007), pp. 2137–2142. DOI: 10.1142/S0218301307007581. eprint: nucl-ex/0703001.

[53] Oleg A. Grachov et al. "Status of zero degree calorimeter for CMS experiment". In: *AIP Conf.Proc.* 867 (2006), pp. 258–265. eprint: nucl-ex/0608052.

[54] Kenneth Aamodt et al. "Centrality dependence of the charged-particle multiplicity density at mid-rapidity in Pb-Pb collisions at $\sqrt{s_{NN}} = 2.76$ TeV". In: *Phys.Rev.Lett.* 106 (2011), p. 032301. DOI: 10.1103/PhysRevLett.106.032301. eprint: 1012.1657.

[55] C. A. Ogilvie et al. "Rise and fall of multifragment emission". In: *Phys. Rev. Lett.* 67 (10 1991), pp. 1214–1217.

[56] Zi-Wei Lin et al. "A Multi-phase transport model for relativistic heavy ion collisions". In: *Phys.Rev.* C72 (2005), p. 064901. DOI: 10.1103/PhysRevC.72.064901. eprint: nucl-th/0411110.